OBSERVATIONAL TESTS OF COSMIC ACCELERATION

by

Alireza Hojjati

M.Sc. Isfahan University of Technology, 2006

THESIS SUBMITTED IN PARTIAL FULFILLMENT
OF THE REQUIREMENTS FOR THE DEGREE OF
DOCTOR OF PHILOSOPHY
IN THE
DEPARTMENT OF PHYSICS

SIMON FRASER UNIVERSITY
Summer 2012

APPROVAL

Name:	**Alireza Hojjati**
Degree:	Doctor of Philosophy
Title of Thesis:	Observational tests of cosmic acceleration
Examining Committee:	**Dr. Eldon Emberly**, Associate Professor (Chair)
	Dr. Levon Pogosian Senior Supervisor, Associate Professor
	Dr. Andrei V. Frolov Supervisor, Associate Professor
	Dr. Howard Trottier Supervisor, Professor
	Dr. Dugan O'Neil Supervisor, Associate Professor
	Dr. Kris Sigurdson External Examiner, Assistant Professor Department of Physics and Astronomy University of British Columbia
Date Approved:	July 18, 2012

Partial Copyright Licence

The author, whose copyright is declared on the title page of this work, has granted to Simon Fraser University the right to lend this thesis, project or extended essay to users of the Simon Fraser University Library, and to make partial or single copies only for such users or in response to a request from the library of any other university, or other educational institution, on its own behalf or for one of its users.

The author has further granted permission to Simon Fraser University to keep or make a digital copy for use in its circulating collection (currently available to the public at the “Institutional Repository” link of the SFU Library website (www.lib.sfu.ca) at http://summit/sfu.ca and, without changing the content, to translate the thesis/project or extended essays, if technically possible, to any medium or format for the purpose of preservation of the digital work.

The author has further agreed that permission for multiple copying of this work for scholarly purposes may be granted by either the author or the Dean of Graduate Studies.

It is understood that copying or publication of this work for financial gain shall not be allowed without the author’s written permission.

Permission for public performance, or limited permission for private scholarly use, of any multimedia materials forming part of this work, may have been granted by the author. This information may be found on the separately catalogued multimedia material and in the signed Partial Copyright Licence.

While licensing SFU to permit the above uses, the author retains copyright in the thesis, project or extended essays, including the right to change the work for subsequent purposes, including editing and publishing the work in whole or in part, and licensing other parties, as the author may desire.

The original Partial Copyright Licence attesting to these terms, and signed by this author, may be found in the original bound copy of this work, retained in the Simon Fraser University Archive.

Simon Fraser University Library
Burnaby, British Columbia, Canada

revised Fall 2011

Abstract

The accelerating expansion of the universe is considered to be a well-established fact. However, a physical explanation of its origin is still missing. While the cosmological constant, Λ, is the favorite candidate, a multitude of other theories have been proposed. Rather than testing every theory against data, one can adapt phenomenological approaches aimed at testing Λ.

Adopting a model-independent approach to studying dark energy, we have investigated the utility of wavelets for constraining the redshift evolution of the dark energy equation of state, $w(z)$, from a combination of the type Ia supernovae (SNe Ia), cosmic microwave background (CMB) and baryon acoustic oscillation (BAO) data. We have shown that sharp deviations from $w_\Lambda = -1$ can be detected efficiently. Applying this method to the "Constitution" SNe Ia data, combined with the CMB data from Wilkinson microwave anisotropy probe (WMAP) and BAO data from Sloan digital sky survey, provided only weak hints of dark energy dynamics.

Future weak lensing surveys will have the ability to measure the growth of large scale structure with accuracy sufficient for discriminating between different theories of dark energy and modified gravity (MG). The growth of structure can be tested, in a model-independent way, by parametrizing the evolution equations of cosmological perturbations. At the linear level, this can be achieved by introducing two scale- and time-dependent functions (MG functions). We have consistently implemented the parametrized equations in the commonly used public codes, CAMB and CosmoMC, while preserving the covariant conservation of the energy-momentum. As a demonstration, we have obtained joint constraints on the neutrino mass and parameters of a scalar-tensor gravity model from the CMB, SNe Ia and the correlation of CMB with large scale structure.

We have performed a Principal Component Analysis (PCA) to find the eigenmodes and eigenvalues of the forecasted covariance matrix of the MG functions for surveys like Dark Energy Survey and Large Synoptic Survey Telescope. By examining the eigenmodes, we can learn about the scales and redshifts where the surveys are most sensitive to modification of the growth. We have considered the impact of some of the systematic effects expected in weak lensing surveys. Also, we have demonstrated the utility of the PCA as an efficient way of storing information about the linear growth of perturbations.

Finally, we have analyzed the degeneracy between the MG functions and other cosmological parameters, paying special attention to the effective equation of state $w(z)$. We have taken several models with different MG parametrizations and studied their merits. We have shown how the complementarity of different observables helps break the degeneracies.

Key words: dark energy, modified gravity, cosmological parameters, observational constraints, principal component analysis, massive neutrinos.

"There was a door to which I found no key
There was the veil through which I might not see ..."

- Omar Khayyam

To the random incidents in life ...

Acknowledgments

First of all, I would like to thank my advisor, Levon Pogosian. He has been a supportive supervisor and a good friend, a pusher when I was slowing down and a helper when I was confused. I enjoyed the useful conversations with Andrei V. Frolov on all the different topics that came up during these years. I am thankful to Howard Trottier for teaching me QED, with a taste of passion, and for being one of my examples as a very nice person. Gong-Bo Zhao taught me about the tools I needed for my research and I learned a lot from him. Aaron Berndsen introduced Linux to me for the first time and now, I can not work without it.

I am grateful to the staff and faculty of the Physics department at SFU who made it a fun and friendly environment to work in. The staff have been very helpful with all the administrative works and I could always count on them. I also enjoyed all the times I spend in the same office with Firuz Demir during the PhD years.

And last but foremost, in the background of any achievement lies the support and contribution of family and friends. And I am grateful for having many of them. I believe they all are aware of their importance to me and spare me of writing a long list of their names. I have shown and will show my gratitude to them in person.

Contents

List of Tables

List of Figures

Chapter 1

Introduction

With the development of General Relativity (GR) in the beginning of 20th century [1], our understanding of the universe fundamentally changed. Cosmology, as a new branch of science, could now be properly formulated in a theoretical framework. With the advancement of telescopes, further and further galaxies could be observed and the dynamics of their motion on larger scales began to be revealed. The agreement of Hubble's discovery of the expansion of the universe [2] with solutions of GR equations of motion provided one of the first experimental confirmations in cosmology.

Based on the GR equations, the expansion rate of a universe containing only matter should eventually slow down due to the attractive force of gravity. That led many observational scientist to try to measure the slow-down rate, a *deceleration* parameter. To their surprise, observations of type Ia supernovae in 1998 revealed that at present, the expansion is instead accelerating [3, 4, 5].

The origin of cosmic acceleration is still a big puzzle in cosmology. The simplest model that could explain the new observations, the ΛCDM model, requires about 70% of the energy budget of the universe to come from vacuum energy, the Cosmological Constant (CC). CC has had a history of appearing in and then disappearing from the cosmological models. It was introduced by Einstein in 1917 to design a static, matter dominated universe [6]. After a proof that such universe is unstable [7], CC was forgotten until 1968, when Zel'dovich realized that the stress energy of empty space is mathematically equivalent to CC and, hence, can not be simply dismissed. 30 years later, there was, again, a good observational motivation for considering the CC.

As we will describe in this chapter, there are problems associated with CC which have motivated physicists to think of alternatives to the ΛCDM model. Never short of ideas, theorists tried to introduce other theories of dark energy which could avoid some of the CC problems. In Chapter 2, we look at these theories, their observational consequences and their shortcomings.

As a different approach, the validity of GR on the cosmological scales has been questioned. Although GR had passed all the terrestrial and solar system tests, it has not been tested properly on very large scales. Alternative gravity theories have been proposed that behave differently from GR on cosmological scales. We will review these theories in Chapter 3.

All the proposed theories of dark energy or alternative gravity need to be studied thoroughly and tested against data. Despite the efforts for developing a compelling theory, capable of explaining the cosmic acceleration, no such theory is known yet. This has motivated taking a phenomenological approach instead. In this case, the goal would be to test the ΛCDM model against data in a model-independent way. If any departures from ΛCDM are observed, the efforts could then be focused efficiently on explaining the observed phenomena. In this thesis, new phenomenological schemes are developed for testing the ΛCDM model.

We start this chapter with a brief introduction to cosmology, and then move to description of the evidence for acceleration. Finally, we describe the ΛCDM model.

1.1 Basic cosmology

Our understanding of the universe is based on the *cosmological principle* stating that the universe is spatially homogeneous and isotropic on large scales. This leads to a simple form of the metric for the universe, the Friedmann-Robertson-Walker (FRW) metric. The line element for the FRW metric is

$$ds^2 = -dt^2 + a(t)^2 \left[dr^2 + S_\kappa^2(r,R) d\Omega \right] , \tag{1.1}$$

where a is the scale factor, t is the cosmic time, R is the curvature radius of the universe and

$$\begin{aligned} \kappa &= 0 & S_\kappa(r,R) &= r & &\text{Flat geometry}\,, \\ \kappa &= -1 & S_\kappa(r,R) &= R\, sinh(r/R) & &\text{Open geometry}\,, \\ \kappa &= +1 & S_\kappa(r,R) &= R\, sin(r/R) & &\text{Closed geometry}\,. \end{aligned} \tag{1.2}$$

For a flat universe we can rewrite the line element as

$$ds^2 = a(\tau)^2(-d\tau^2 + \delta_{ij}\, dx^i dx^j) \tag{1.3}$$

where here x^i is a Cartesian coordinate, $d\vec{x} \equiv d\vec{r}/a(\tau)$ and

$$d\tau = \frac{dt}{a(t)} \tag{1.4}$$

is the *conformal* time. The homogeneous and isotropic expansion of the universe can be characterized by the *Hubble* parameter defined as

$$H \equiv \frac{\dot{a}}{a} \tag{1.5}$$

where dot represents derivative with respect to t. The value of the Hubble parameter today, H_0, is measured to be about 70 $km/s/Mpc$ where $1pc \approx 3.1 \times 10^{16}$ meters.

The contents of universe are considered to be *perfect fluids*, with their energy-momentum tensor defined as

$$T^{\mu\nu} = (\rho + P)U^\mu U^\nu + P g^{\mu\nu}, \tag{1.6}$$

where ρ is the energy density, P is the isotropic pressure, and U^μ is the four velocity of the fluid. Energy-momentum conservation,

$$T^\mu{}_{\nu;\mu} = T^\mu{}_{\nu,\mu} + \Gamma^\mu{}_{\alpha\mu} T^\alpha{}_\nu - \Gamma^\alpha{}_{\nu\mu} T^\mu{}_\alpha = 0. \tag{1.7}$$

determines how the energy density of matter evolves as the universe expands. For $\nu = 0$ in

Eq. (1.8), we get the *fluid* or *continuity* equation

$$\dot{\rho} + 3H(\rho + P) = 0\,. \tag{1.8}$$

We can describe the relationship between a fluid's pressure and energy density using an *equation of state* (EoS) parameter, w,

$$w \equiv \frac{P}{\rho}\,. \tag{1.9}$$

and write Eq. (1.8) as

$$\dot{\rho} + 3H(1 + w)\rho = 0\,. \tag{1.10}$$

With a change of variables,

$$\frac{d\rho}{dt} \to \frac{d\rho}{da}\frac{da}{dt}\,, \tag{1.11}$$

the integration of Eq. (1.10) yields

$$\frac{\rho_i(a)}{\rho_i^0} = \exp\left[-3\int_a^1 (1 + w_i(a))\,d\ln a\right]\,, \tag{1.12}$$

where ρ_i^0 is the energy density today, when $a = 1$. For normal matter, the pressure of a species is related to the kinetic energy $\propto m < v >^2$, while the energy density $\sim mc^2$. Therefore, for non-relativistic matter, such as baryons and cold dark matter (CDM), one would expect the EoS to be negligible, while for relativistic species, such as photons, $< v^2 >\sim c^2/3$.

In cosmology, the dynamics of gravity is determined from the equations of General Relativity (GR). Unlike what we have in the classical physics, where the normalization of energy is arbitrary, in GR, however, the actual value of the energy density matters, i.e. the value of V_0 has a role in the dynamics. One then needs to include the expectation value of the vacuum, usually referred to as the *cosmological constant* (CC), Λ. CC is a component with a constant energy density with an energy-momentum tensor as

$$T^{\mu\nu} = -\rho_\Lambda g^{\mu\nu}\,. \tag{1.13}$$

Requiring that $\dot{\rho}_\Lambda = 0$, Eq. (1.8) gives

$$\rho_\Lambda \equiv \Lambda/(8\pi G) = -P_\Lambda\,. \tag{1.14}$$

We can therefore write

$$\begin{aligned} w_{\rm NR} &\approx 0\,, \\ w_{\rm R} &= \frac{1}{3}\,, \\ w_\Lambda &= -1\,. \end{aligned} \tag{1.15}$$

For a constant w, Eq. (1.12) yields

$$\frac{\rho_i(a)}{\rho_i^0} = a^{-3(1+w_i)}\,. \tag{1.16}$$

Since the universe is made up of a variety of different matter species, we need to consider the dynamics from the combination of these fluids. Hence, we can define an *effective* EoS fro the effective fluid as

$$w_{eff} = \frac{P_{tot}}{\rho_{tot}}\,, \tag{1.17}$$

where P_{tot} and ρ_{tot} are now the total pressure and energy density of the effective fluid.

1.1.1 Background dynamics

Dynamics of a homogeneous and isotropic universe, described by the FRW metric, is described by the evolution of the scale factor through the Einstein equations

$$G_{\mu\nu} \equiv R_{\mu\nu} - \frac{1}{2}g_{\mu\nu}R = 8\pi G T_{\mu\nu} - \Lambda g_{\mu\nu}\,. \tag{1.18}$$

Using Eqs. (1.1) and (1.8) in the above equation, we derive the evolution equations for the FRW universe. The 00 component of Eq. (1.18) gives the *Friedmann* equation

$$\left(\frac{\dot{a}}{a}\right)^2 \equiv H^2 = \frac{8\pi G}{3}\rho - \frac{K}{a^2} + \frac{\Lambda}{3}\,, \tag{1.19}$$

where ρ is the total energy density from all the constituents in the universe. Combination of the 00 and *ii* components of Eq. (1.18) gives us the *acceleration* equation

$$\frac{\ddot{a}}{a} = -\frac{4\pi G}{3}(\rho + 3P) + \frac{\Lambda}{3}. \tag{1.20}$$

Eq. (1.20) predicts that the universe should be *decelerating*, $\ddot{a} < 0$, when it is filled with the *ordinary* types of matter (photons, neutrinos, dark matter (DM) and baryons) with $w_{eff} \geq -1/3$, but *accelerating* when $w_{eff} \leq -1/3$.

We can define a *critical density,* $\rho_{crit}(a)$, as the total energy density in a flat universe, so that $K = 0$ in (1.19)

$$\rho_{crit}(a) \equiv \frac{3H^2(a)}{8\pi G}. \tag{1.21}$$

The *fractional energy density* for a species i, $\Omega_i(a)$, is defined as

$$\Omega_i(a) \equiv \frac{\rho_i(a)}{\rho_{crit}(a)}. \tag{1.22}$$

The fractional energy *today* for a species will be written Ω_i^0. The above definitions will be useful later.

1.1.2 Cosmological distances

Comoving Distance: Comoving coordinates is a system of coordinates fixed with respect to the overall Hubble flow of the universe. In the comoving frame, the location of a given galaxy does not change as the universe expands. This allows distances and locations in an expanding FRW universe to be related simply in terms of the scale factor. For example, a *physical* distance between two objects can be described as

$$d_{phys} \equiv a\,\chi, \tag{1.23}$$

where χ is the corresponding distance in the comoving coordinates.

Redshift: The redshift, z, is a measure of how much the wavelength of light is stretched due to the expansion of the universe, while traveling a distance. It is defined as

$$1+z \equiv \frac{\lambda(t_r)}{\lambda(t_e)} = \frac{a_r}{a_e}, \tag{1.24}$$

where t_e and t_r are the times of emission and reception of light. One can easily relate the ratio of the wavelengths to the ratio of the corresponding scale factors, as shown in Eq. (1.24). One should note that this cosmological redshift is caused by the expansion of space, not due to the motion of the galaxies that would exist in the absence of expansion. this extra component in the motion of galaxies is called *peculiar motion*. Hence, the total redshift of galaxies (or other objects) can be written as

$$1+z_{tot} = (1+z_{\mathrm{cosmology}})(1+z_{\mathrm{peculiar}}). \tag{1.25}$$

Typical peculiar velocities are of the order of a few 100 km/s, so that, given H_0, they are $\sim 10\%$ of cosmological expansion rate at distances $\sim O$ (10 Mpc) [8].

comoving horizon: The comoving horizon is the maximum comoving distance that information could have propagated (light could have traveled) from the beginning of the universe. For a light ray moving in the radial direction, $ds^2 = 0$, $d\theta = d\phi = 0$ and thus, $d\chi = dr = dt/a(t)$. Then, the total comoving distance traveled by the light ray is

$$\chi(t) = \int_0^t \frac{dt'}{a(t')}. \tag{1.26}$$

We can alternatively write this in terms of the scale factor and the Hubble parameter

$$\chi(a) \quad = \quad \int_0^a \frac{da'}{a'^2 H(a')}. \tag{1.27}$$

Angular diameter distance: The angular diameter distance, d_A, is the distance to an object inferred from comparing the angular size of the object to its length which is assumed to be known from other ways. For an object of length L that appears in the sky with an angle θ, the angular diameter distance is

$$d_A \equiv \frac{L}{\theta}. \tag{1.28}$$

In the comoving coordinates

$$\theta = \frac{L}{a_e \chi(a_e)}\,, \tag{1.29}$$

where $\chi(a_e)$ is the comoving distance to the object and L/a_e is the comoving size of the object. We have to take into account that space has expanded between the emission and observation times. Hence, the angular diameter distance is

$$d_A = a_e\,\chi(a_e) = \frac{\chi(z_e)}{1+z_e}\,. \tag{1.30}$$

In a curved space, the angular size of the object is modified. From the FRW metric

$$L \;=\; a(t)S_\kappa(r,R_0)\theta,\,. \tag{1.31}$$

Therefore, in a curved space we have

$$d_A \;=\; aS_\kappa(\chi,R_0)\,. \tag{1.32}$$

Luminosity distance: The luminosity distance, d_L, is inferred from comparing the brightness (flux) of an object to its luminosity. If an object with luminosity L is observed to have a flux F, then from the inverse square law,

$$d_L \equiv \sqrt{\frac{L}{4\pi F}}\,. \tag{1.33}$$

The cosmic expansion affects the luminosity distance in two ways: Firstly, the light is redshifted and its wavelength increases $\sim 1/a$. Therefore the energy of the photons, $E_\gamma \propto 1/\lambda$, decreases by factor a. Secondly, the number of photons arriving at the detector is also reduced so that $L_{obs} = a^{-2}L_{emit}$. Therefore, we have

$$F = \frac{a^2 L_{obs}}{4\pi\chi(a)^2}\,, \tag{1.34}$$

and

$$d_L = \frac{\chi(a)}{a} = (1+z)\chi(z)\,. \tag{1.35}$$

where $\chi(a)$ is the comoving distance to the object. In a curved universe, the effective observed area is $AS_{\kappa}^{2}(r,R_0)$ with A being the surface area of emission. Hence we have

$$d_L = \frac{S_{\kappa}(\chi,R_0)}{a} \tag{1.36}$$

We can combine Eqs. (1.30) and (1.35) to get

$$d_L(z) = (1+z)^2 d_A(z)\,. \tag{1.37}$$

It means that in an expanding universe, different methods of measuring distances yield different results. While the difference becomes negligible at low redshifts, it is important at cosmological scales.

The distance measurements described above mainly constrain the background cosmological parameters. However, large scale structure surveys offer the opportunity to constrain more cosmological parameters by measuring the growth of cosmic structure (the growth of over-densities and peculiar velocities that seed galaxies and clusters of galaxies). By contrasting expansion history and growth of structure measurements, one can investigate evidence for dark energy perturbations and modifications to gravity [9, 10, 11, 12, 13, 14, 15, 16].

In the next section, we review the linear perturbation theory in cosmology and the dynamics of the growth of large scale structure in the universe.

1.2 Linear perturbation theory

1.2.1 Gravitational instability and Jeans length

The large scale structure we see today is the result of primordial perturbations in the metric which then grew via the gravitational instability of matter. The growth of perturbation is opposed by the pressure of the relativistic matter so that the temporal behavior of the density contrast is governed by a balance between the two forces: the pressure force and the gravitational force.

In the Newtonian context, the evolution of density contrast, δ, follows this second-order differential equation [17]

$$\frac{\partial^2\delta}{\partial t^2} = c_s^2\nabla^2\delta - 4\pi G\rho\delta\,, \tag{1.38}$$

where ρ is the background density and

$$c_s^2 = \frac{\delta P}{\delta\rho}\,, \tag{1.39}$$

is the sound speed of wave propagation in the medium. In the Fourier space, this equation becomes

$$\frac{\partial^2\delta}{\partial t^2} = \left(k^2c_s^2 - 4\pi G\rho\right)\delta\,, \tag{1.40}$$

Two different regimes can be found for Eq. (1.40): a harmonic regime for $k > k_J \equiv \sqrt{4\pi G\rho/c_s^2}$ and a growing exponential regime for $k < k_J$. The critical wavenumber, k_J, defines a critical length called the *Jeans length*

$$\lambda_J = \sqrt{\frac{\pi c_s^2}{G\rho}}\,. \tag{1.41}$$

On the scales smaller than the Jeans length, the pressure forces rule over gravity, preventing the growth of the overdensities. While on the scales larger than the Jeans length, density perturbations grow exponentially under the gravitational collapse.

Since the universe is expanding, it affects the growth of perturbations by introducing a characteristic length scale, the Hubble scale. The Hubble scale is a good measure of small scales and large scales in the universe at a given epoch. It also defines a causal scale below which, the Newtonian theory suffices to describe the gravity, while at larger scales, the full equations of GR is needed. The above analysis, neglecting the expansion and the curvature of the universe, can be valid only locally in a small region of the universe. We will see later how using GR equations in an expansing FRW universe would change the evolution equations of matter density perturbations. The Jeans condition remains the same apart for a scale factor contribution, so that for the gravitational collapse the wavenumber has to satisfy $k < a\,k_J$. It is important to note the role of the sound speed (and the pressure): the smaller its value is, the smaller is λ_J and so a bigger part of the universe is undergoing a gravitational collapse.

1.2.2 Linear perturbations and gauge freedom

In general relativity (GR), the choice of metric variables is not unique, as there is a freedom in choosing a reference frame with respect to which perturbations are defined. This is referred to as *gauge freedom*. By choosing a gauge, one is able to eliminate redundant degrees of freedom (DoF) in the metric and define density fluctuations. Depending on the purpose, one can choose a gauge in which computation is easier or a gauge where the physical interpretation and/or form of the evolution is simplest.

The most general form for a linearly perturbed flat FRW metric can be written as [18]

$$\begin{aligned} g_{00} &= -a^2(\tau)\left\{1+2\psi(\vec{x},\tau)\right\}, \\ g_{0i} &= a^2(\tau)\, w_i(\vec{x},\tau), \\ g_{ij} &= a^2(\tau)\left\{[1-2\phi(\vec{x},\tau)]\delta_{ij}+\chi_{ij}(\vec{x},\tau)\right\}, \qquad \chi_{ii}=0 \end{aligned} \tag{1.42}$$

where the functions ψ, ϕ, w_i and χ_{ij} represent the metric perturbations about the background spacetime. The trace part of the perturbation to g_{ij} is absorbed in ϕ, and χ_{ij} is taken to be traceless.

As a symmetric 4×4 tensor, the metric has ten distinct components, but not all of them are true DoF. The number of the true DoF of the metric can be found from considering the decomposition of each tensor field in Eq. (1.42). w_i and χ_{ij} can be decomposed as

$$\begin{aligned} w_i(\vec{x},\tau) &= w_i^{\parallel}(\vec{x},\tau)+w_i^{\perp}(\vec{x},\tau), \\ \chi_{ij}(\vec{x},\tau) &= \chi_{ij}^{\parallel}(\vec{x},\tau)+\chi_{ij}^{\perp}(\vec{x},\tau)+\chi_{ij}^{S}(\vec{x},\tau), \end{aligned} \tag{1.43}$$

where $\perp$, $\parallel$ and S stand for transverse, longitudinal and solenoidal components, respectively. Since a transverse vector is divergenceless, it can be represented as the curl of another vector ξ_i, while he longitudinal vector can be written as the divergence of a scalar B. Therefore, we can write

$$\begin{aligned} w_i^{\perp} &= \varepsilon_{ijk}\partial^j\xi^k, \\ w_i^{\parallel} &= \partial_i B. \end{aligned} \tag{1.44}$$

The vector ξ_i appears to have three degrees of freedom, but one of these is redundant since we can make the transformation $\xi_i \rightarrow \xi_i + \partial_i \lambda$, where λ is a scalar. One can impose the condition $\partial^i \xi_i = 0$ to eliminate this freedom. Hence, there are two DoF from the transverse component and one from the longitudinal component. Similarly, the longitudinal and transverse components of χ_{ij} add three other true DoF. The solenoidal component in χ_{ij} can be derived from a transverse vector ζ_i which has two DoF.

Thus, we can write the ten distinct components of the metric in terms of four scalars with one DoF each, two transverse vectors with two DoF each, and one transverse (traceless) tensor ($\chi^{\perp}_{ij}$) with two DoF. These are referred to as the "scalar", "vector", and "tensor" modes of the metric [18].

For our purpose of studying the large scale structure at linear order, we consider only the scalar perturbations since these are the ones which couple to the matter perturbations. From the discussion above, the scalar perturbations in the metric can be written as [18]

$$\begin{aligned}
g_{00} &= -a^2(\tau)\left\{1 + 2\psi(\vec{x},\tau)\right\}, \\
g_{0i} &= a^2(\tau)\,\partial_i B(\vec{x},\tau), \\
g_{ij} &= a^2(\tau)\left\{[1 - 2\phi(\vec{x},\tau)]\delta_{ij} + \partial_{ij} E(\vec{x},\tau)\right\},
\end{aligned} \tag{1.45}$$

where ψ, ϕ, A and E are time- and space-dependent scalars. Furthermore, one can show that these four scalars are transformed under a general coordinate transformation by two other scalar functions [18]. Hence, there are only two true scalar DoF in the perturbed metric. However, the decomposition in Eq. (1.45) does not uniquely specify the two independent scalar variables. One can choose different coordinate systems in which the metric is decomposed into the same background metric but perturbations are different. By choosing a gauge we are specifying the perturbations we are working with. Here, we briefly introduce two frequently used gauges, *synchronous* and *conformal Newtonian* gauges, that will be used later.

The Synchronous gauge, in which $\psi = B = 0$, has the property that there exists a set of comoving observers which fall freely without changing their spatial coordinates. This is the natural coordinate system for freely falling observers. Each of such observers has conformal time, $d\tau$, and a fixed spatial coordinate label, x^i. These times and coordinate labels can be used to define the coordinate values at all spacetime points [1] [15].

---

[1] Syncronous gauge has a residual degree of freedom that can be further eliminated by, e.g., setting the

For the rest of this chapter, we work in the conformal Newtonian gauge in which $E = B = 0$ and the scalar linear perturbations to metric can be expressed as [18]

$$\begin{aligned} g_{00} &= -a^2(\tau)\left[1+2\psi(\vec{x},\tau)\right], \\ g_{0i} &= 0, \\ g_{ij} &= a^2(\tau)\left[1-2\phi(\vec{x},\tau)\right]\delta_{ij}. \end{aligned} \tag{1.46}$$

The conformal Newtonian gauge is a simple gauge to use for the scalar perturbations. It is called Newtonian gauge because perturbations of the metric in this gauge are simply related to the Newtonian gravitational potential of classical Newtonian gravity.

To study the growth of inhomogeneities in the full general relativistic way, we need to consider perturbations in metric and energy-momentum tensor. We choose to work in the conformal Newtonian gauge as a good choice when scalar perturbations are considered. At the linear level, the scalar perturbations are characterized by two *scalar potentials* ψ and ϕ, which appear in the perturbed line element as [18]

$$ds^2 = a^2(\tau)\left\{-(1+2\psi)d\tau^2 + (1-2\phi)dx^i dx_i\right\}. \tag{1.47}$$

The components of the linearly perturbed energy momentum tensor can be written as

$$\begin{aligned} T^0{}_0 &= -\rho(1+\delta), \\ T^0{}_i &= -(\rho+P)v_i, \\ T^i{}_j &= (P+\delta P)\delta^i_j + \pi^i_j, \end{aligned} \tag{1.48}$$

where $\delta \equiv \delta\rho/\rho$ is the density contrast, v the velocity field, δP the pressure perturbation and π^i_j denotes the traceless component of the energy-momentum tensor. Energy momentum conservation, $T^{\mu\nu}{}_{;\mu} = 0$, for the inhomogeneous matter gives us the perturbed fluid equations [18]

$$\dot{\delta} = -(1+w)(ikv+3\dot{\phi}) - 3\mathcal{H}(c_s^2 - w)\delta, \tag{1.49}$$

$$\dot{v} = -\mathcal{H}(1-3w)v - \frac{\dot{w}}{1+w}v - \frac{c_s^2}{1+w}ik\delta - ik\psi + ik\sigma, \tag{1.50}$$

---

velocity of CDM to zero.

where $\mathcal{H} = aH$. Substituting Eqs. (1.47) and (1.48) into Einstein equations, Eq. (1.18), one can derive the linear Einstein equations in the conformal Newtonian gauge [18]:

$$\begin{aligned}
k^2\phi + 3\frac{\dot{a}}{a}\left(\dot{\phi} + \frac{\dot{a}}{a}\psi\right) &= 4\pi G a^2 \delta T^0{}_0\,, && (1.51)\\
k^2\left(\dot{\phi} + \frac{\dot{a}}{a}\psi\right) &= 4\pi G a^2 (\bar{\rho} + \bar{P})\theta\,, && (1.52)\\
\ddot{\phi} + \frac{\dot{a}}{a}(\dot{\psi} + 2\dot{\phi}) + \left(2\frac{\ddot{a}}{a} - \frac{\dot{a}^2}{a^2}\right)\psi + \frac{k^2}{3}(\phi - \psi) &= \frac{4\pi}{3} G a^2 \delta T^i{}_i\,, && (1.53)\\
k^2(\phi - \psi) &= 12\pi G a^2 (\bar{\rho} + \bar{P})\sigma\,, && (1.54)
\end{aligned}$$

where θ and σ are defined as

$$(\bar{\rho} + \bar{P})\theta \equiv i k^j \delta T^0{}_j\,, \qquad (\bar{\rho} + \bar{P})\sigma \equiv -(\hat{k}^i \hat{k}_j - \frac{1}{3}\delta^j_i)\pi^i_j\,. \qquad (1.55)$$

1.2.3 Initial conditions

The evolution equations derived in the previous section can be solved once the initial conditions for the perturbations are specified. In the linear theory, the evolution of each k mode is independent. One can therefore evolve the equations for a given k-mode from when it is still outside the horizon, i.e., $k\tau \ll 1$. The initial conditions for perturbations is assumed to be set after inflation, when the corresponding mode is outside the horizon.

The leading-order behavior of super-horizon-sized perturbations in the conformal Newtonian gauge can be summarized as [18]

$$
\begin{aligned}
&\psi = \frac{20C}{15+4R_\nu}, \\
&\phi = (1+\frac{2}{5}R_\nu)\psi, \\
&\delta_\gamma = -2\psi, \\
&\delta_c = \delta_b = \frac{3}{4}\delta_\nu = \frac{3}{4}\delta_\gamma, \\
&\theta_\gamma = \theta_\nu = \theta_c = \theta_b = \frac{1}{2}(k^2\tau)\psi, \\
&\sigma_\nu = \frac{1}{15}(k\tau)^2\psi,
\end{aligned}
\tag{1.56}
$$

where C is a constant, $R_\nu \equiv \bar{\rho}_\nu/(\bar{\rho}_\gamma+\bar{\rho}_\nu)$ and subscripts γ, ν, c, b stand for photons, neutrinos, cold dark matter (CDM) and baryons, respectively. If we specify the initial value of ψ (or the constant C), all the other quantities can be derived from Eqs. (1.56). In the inflationary scenario, the initial value of ψ for each mode is related to the inflaton field Φ as [19]

$$\psi|_{post\ inflation} = \frac{2}{3}aH\frac{\delta\Phi}{\dot{\Phi}}|_{horizon\ crossing} \tag{1.57}$$

where $\delta\Phi$ is the perturbations of the inflaton field and "horizon crossing" stands for the moment the corresponding mode exits the horizon.

1.3 Cosmological observables

1.3.1 Distance measurements

Supernovae

Type 1a supernovae (SNe Ia) is an example of a *standard candle*. A standard candle is an object whose luminosity can be inferred from its physical properties, or some other observable. The *apparent magnitude, m,* of an object is related logarithmically to its flux.

For two objects, their apparent magnitudes and fluxes are related by

$$m_1 - m_2 = 2.5\log(\frac{F_2}{F_1})\,, \tag{1.58}$$

with the zero-point $m = 0$ set by a reference star. An object's *absolute magnitude* is defined as its apparent magnitude at a fixed distance

$$m - M = 5\log(\frac{d_L}{10\text{pc}})\,, \tag{1.59}$$

where the fixed distance is 10 pc in the above equation. From a comparison between a supernova's apparent and (assumed) absolute magnitudes, one can use Eq. (1.33) to estimate its luminosity distance. The quantity that is usually derived from measurements is the *distance modulus*, μ, defined as

$$\mu \equiv m - \mathcal{M} = 5\log\left(H_0\, d_L\right)\,, \tag{1.60}$$

where $\mathcal{M} \equiv M - 5\log(H_0 Mpc^{-1}) + 25$, is calibrated using low-redshift supernovae.

SNe Ia are extremely bright and are observable from very large distances. This property makes them an ideal target for measuring distances to object at high redshifts. As we will see, SNe Ia observations gave the first evidence for cosmic acceleration, and have provided the most effective constraints on the dark energy EoS parameter.

Cosmic Microwave Background (CMB)

The Cosmic Microwave Background (CMB) are relic photons released at the time of *recombination*, when the universe cooled enough for the ionized plasma of free electrons and protons to form neutral hydrogen. Before recombination, photons were interacting with the free electrons through the Thomson scattering. The scattering rate dropped significantly after recombination and, therefore, photons could *freely stream*.

CMB is considered a *standard ruler* and provides another measure of the expansion history. The angular diameter distance to the recombination is inferred by comparing the apparent angular size of correlations in the CMB temperature to their expected size, estimated from calculations of the propagation speed of photons in the ionized plasma, prior to recombination.

The sound speed of photons in the plasma prior to recombination, c_s, is roughly given by $c_s = c/\sqrt{3}$. The sound horizon at the recombination, r_s, describes the maximum distance photons could have traveled until recombination time. It provides a typical correlation length for any inhomogeneities (appear as temperature fluctuations in the CMB) that could be generated through causal processes. The comoving scale of the sound horizon is given by

$$r_s = \int_{t_i}^{t_{\mathrm{rec}}} c_s \, d\tau \sim \frac{(1+z_{rec})c_s}{H(z_{rec})}\,, \tag{1.61}$$

which is measured to be ≈ 145 Mpc today. The angular size of r_s today can be derived as

$$\theta = \frac{r_s}{d_A}\,, \tag{1.62}$$

where d_A is the angular diameter distance to recombination. CMB provides a complementary measurement of expansion history to the SNe Ia observations. However, it contains much more information than just a distance to recombination. There are many secondary effects that change CMB on its way to reaching us today. Some of these effects will be explained in the following sections.

Baryon Acoustic Oscillations (BAO)

As explained before, prior to recombination the photons and baryons were tightly coupled to each other through Thomson scattering, and the electrostatic attraction of the electrons and protons. Due to this tight coupling, the pressure waves in baryons would propagate with the same speed as photons, i.e. with $c_s \sim c/\sqrt{3}$. After decoupling from photons, baryons behaved as non-relativistic fluid and their sound speed dropped effectively to zero. As a result, baryon density distribution did not propagate anymore and a correlation with characteristic size r_s remains imprinted in the distribution of the baryons.

Baryons and DM then fell into each other's gravitational well and seeded the large scale structure we observe today. This preferred scale, r_s, can be observed in today's galaxy correlation function as a correlation bump (fig. 1.1). When Fourier transformed, this bump translates into a series of oscillations and hence is called *baryon acoustic oscillations* (BAO).

Having a characteristic size, BAO can be used as another standard ruler for constraining the cosmological parameters.

Complementarity of distance measures

The constraints on the cosmological parameters from different distance measurements can act as complementary to each other to shrink the parameter constraints. The agreement between these measurements assures us that there are not any systematics that are not taken into account. As an example, the complementarity of distance measurements for constraining some of the main cosmological parameters is shown in Fig. (1.2).

1.3.2 Measurement of growth of structure

After cosmological distances, the next frontier in constraining the cosmological parameters is measurements of the growth of inhomogeneities in the universe. By observing how the large scale structure of the universe looks today, we can make inference about the initial conditions for the perturbed universe and the intermediate cosmological events. These observations are complementary to the *background* measurement described in the previous section and can constrain some of the parameters to which the background observables are weakly sensitive.

The observable quantities discussed in this section have a statistical nature and are based on the two-point correlation functions. The two-point correlation function between 2D-fields X and Y, measured by an observer at the origin, is defined as

$$C^{XY}(\theta) = \langle X(\hat{\mathbf{n}}_1) Y(\hat{\mathbf{n}}_2) \rangle \,, \tag{1.63}$$

where $\hat{\mathbf{n}}$ is a direction in the sky, $\hat{\mathbf{n}}_1.\hat{\mathbf{n}}_2 = \cos(\theta)$ and the average is over all the points on the sky. $X(\hat{\mathbf{n}})$ (and also $Y(\hat{\mathbf{n}})$) can be expanded in spherical harmonics as

$$X(\hat{n}) = \sum_{l=0}^{\infty} \sum_{m=-l}^{l} a_{lm} Y_{lm}(\hat{n}) \,, \tag{1.64}$$

where a_{lm} is the expansion coefficient. $C^{XY}(\theta)$ can be expanded in Legendre series as

$$C^{XY}(\theta) = \sum_{\ell=0}^{\infty} \frac{2\ell+1}{4\pi} C_{\ell}^{XY} P_{\ell}(\cos\theta)\,. \tag{1.65}$$

The expansion coefficients $C_{\ell}^{XY} \equiv \langle a_{lm} a_{l'm'}^{*} \rangle$ are called the angular power spectrum and can be written as

$$C_{\ell}^{XY} = 4\pi \int \frac{dk}{k} \Delta_{\mathcal{R}}^{2} I_{\ell}^{X}(k) I_{\ell}^{Y}(k), \tag{1.66}$$

where I_{ℓ} are the transfer functions defined as

$$I_{\ell}^{X}(k) = \int_{0}^{z_*} dz\, W_X(z) j_{\ell}[kr(z)] \tilde{\mathcal{X}}(k,z)\,, \tag{1.67}$$

and similarly for I_{ℓ}^{Y}. In the above, z_* is a sufficiently high redshift at which the initial condition for the mode k is specified, j_{ℓ} are the spherical Bessel functions, $r(z)$ the comoving distance to a point at redshift z, and W_X are the window functions which, depending on the observable, specify the range of redshifts contributing to X. Finally, $\tilde{\mathcal{X}}(k,z)$ is the Fourier transform of the three-dimensional field $\mathcal{X}(\hat{n}r(z),z)$ responsible for producing the two-dimensional observable X (*i.e.* $X(\hat{n}) = \int_0^{\infty} dz W_X(z) \mathcal{X}(\hat{n}r(z),z)$).

The statistical uncertainty in the angular power spectrum C_{ℓ} is

$$\Delta C_{\ell} = \sqrt{\frac{1}{2(\ell+1) f_{sky}}} C_{\ell}\,, \tag{1.68}$$

where f_{sky} is the fracyion of the sky covered by a survey. This sampling uncertainty, known as *cosmic variance*, is because each C_{ℓ} has only $2\ell+1$ degrees of freedom as the universe is isotropic (there is no preferred axis) and all the m modes in $a_{\ell m}$ are summed over. For small ℓ, cosmic variance puts a systematic limitation on the precision of the measurements of an observable.

Galaxy number counts (GC)

Galaxy number Count (GC) probes the distribution and growth of matter inhomogeneities. From Press-Schechter theory [23], one can calculate the fraction of space volume which collapses to form gravitationally bounded objects from initial random density fluctuations.

The number density of these objects has the following differential relation with the mass (M) and redshift of the object [19]

$$\frac{dn(M,z)}{dM} = \sqrt{\frac{2}{\pi}}\,\frac{\rho_m\,\delta_c}{3M^2\,\sigma}\,\exp\left(\frac{-\delta_c^2}{2\sigma^2}\right)\left[-\frac{R}{\sigma}\frac{d\sigma}{dR}\right], \tag{1.69}$$

where R is the radius over which the density field is smoothed, $\sigma(R,z)$ is the rms of the smoothed density field and ρ_m is the density of a spherical region with radius R

$$\rho_m = \frac{M}{4\pi R^3/3}, \tag{1.70}$$

and δ_c is the critical density above which there is a gravitational collapse. Eq. (1.69) together with the knowledge about galaxy formation processes can be used to estimate the number of galaxies we should observe at each redshift.

One can describe the expected redshift distribution of galaxies by taking the total galaxy number density to be [24]

$$N_G(z) \propto z^2 \exp(-z/z_0), \tag{1.71}$$

where the value of z_0 for a given experiment depends on how faint an object it can observe and defines the redshift at which the most galaxies will be observed. This function compromises between two effects; more distant galaxies are harder to see and less of them have been formed at very high redshift, so they are less likely to be observed, but on the other hand, as one goes to higher redshifts, there is more volume of space available and thus one expects more galaxies. The window function is normalized so that the total number of galaxies matches that expected from a given survey.

With *tomographic* surveys, one can estimate the redshift of the observed galaxies precise enough so that they can be distributed into multiple redshift bins. Labeling the bins with index i, we have

$$N_G(z) = \sum_i N_{G_i}(z). \tag{1.72}$$

One can assume that the photometric redshift errors are Gaussian distributed, and that their rms fluctuations increase with redshift as [231, 25]

$$\sigma(z) = \sigma_{\max}(1+z)/(1+z_{\max}), \tag{1.73}$$

where z_{max} is the maximum redshift covered by a survey. The resulting photometric redshift distributions are given by

$$N_{G_i}(z) = \frac{1}{2} N_G(z) \left[\mathrm{erfc}\left(\frac{z_{i-1} - z}{\sqrt{2}\sigma(z)} \right) - \mathrm{erfc}\left(\frac{z_i - z}{\sqrt{2}\sigma(z)} \right) \right], \tag{1.74}$$

where "erfc" is the complementary error function. For a given photometric redshift bin, the normalized selection function that appears in Eq. (1.67) is given by

$$W_{G_i}(z) = \frac{N_{G_i}(z)}{N^i} \tag{1.75}$$

where N^i is the total number of galaxies in the i-th bin. Eq. (1.67) for GC is written as

$$I_\ell^G(k) = b_i \int_0^{z_*} dz W_G(z) j_\ell[kr(z)] \delta(k,z), \tag{1.76}$$

where $\delta(k,z)$ is the density contrast of baryonic matter (CDM + baryons) and b_i is the bias in the ith bin. The bias coefficient accounts for the fact that baryonic matter traces the CDM:

$$\delta_b = b(k,z)\delta_m . \tag{1.77}$$

If only very large scales are considered, where linear perturbation theory is valid, the bias can be treated as scale-independent and only as a function of the redshift.

Integrated Sachs Wolfe (ISW) effect

As photons stream in all directions after recombination, they pass through gravitational potential wells, gaining energy as they fall into the well, and losing it as they climb out. During the period of accelerated expansion the growth of overdensities is suppressed and it causes the gravitational potential wells to decay over time so that photons gain more energy on their descent into the well than they lose on their climb out later. This gain in energy is translated into a boost in large scale correlation amplitude in the CMB power spectrum. Hence, ISW effect depends on the rate of the change in the gravitational potentials: $\Delta(\phi + \psi)/\Delta z$.

The transfer function, Eq. (1.67), for ISW is

$$I_\ell^{ISW}(k) = \int_0^{z_*} dz e^{-\tau(z)} j_\ell[kr(z)] \frac{\partial}{\partial z}[\psi + \phi] \ , \tag{1.78}$$

where z_* is the recombination redshift and $\tau(z)$ is the reionization *optical depth*

$$\tau(z) = \int_0^z n_e \sigma_T \frac{c}{(1+z)H(z)} dz . \tag{1.79}$$

The $e^{-\tau(z)}$ term in Eq. (1.78) takes into account that some CMB photons are scattered by free electrons created when the universe was reionized by the first stars at $z \approx 10$. Here n_e is the electron number density and σ_T is the Thomson scattering cross-section. The more opaque (more ionized) the universe is to the photons, the larger the optical depth.

ISW is a large scale effect and hence, is dominated by cosmic variance. It has been measured already to the cosmic variance limits by the WMAP survey [28].

Weak lensing (WL)

When light travels through a gravitational potential well its path is distorted much as it would be through an optical lens. Two primary effects happen due to lensing. The image can be magnified and also, the image can be distorted. Since we observe a 2-D field in sky, the effect of lensing on object can be described by the change in the observation angles of the objects.

If θ_S and θ are the angles of the light ray emitted by a source and observed by an observer respectively, then one can define a 2×2 symmetric matrix [19]

$$A_{ij} = \frac{\partial \theta_S^i}{\partial \theta^j} , \tag{1.80}$$

describing the transformation between $\overrightarrow{\theta}_S$ and $\overrightarrow{\theta}$. The matrix A can be decomposed as

$$A \equiv \begin{pmatrix} 1-\kappa-\gamma_1 & -\gamma_2 \\ -\gamma_2 & 1-\kappa+\gamma_1 \end{pmatrix} , \tag{1.81}$$

where κ is the *convergence* which is related to the magnification, and $\gamma = \gamma_1 + i\gamma_2$ is the *shear*. The *weak* lensing condition applies when $|\kappa|, |\gamma_i| << 1$.

The transfer function, Eq. (1.67), for WL convergence can be written as

$$I_l^{\kappa}(k) = \int_0^{z_*} dz\, W_\kappa(z)\ j_l[kr(z)](\psi + \phi)\,, \tag{1.82}$$

where $W_\kappa(z)$ is the window function

$$W_\kappa(z) = \int_z^{\infty} dz' \frac{r(z') - r(z)}{r(z)} n(z')\,, \tag{1.83}$$

and $n(z)$ is the normalized redshift distribution of galaxies. In the limit of weak lensing, the convergence power spectrum is identical to the shear power spectrum and it simplifies the extraction of information about the weak lensing field [29].

Lensing is sensitive to both dark energy's effect on cosmic geometry, through the expansion history's effect on the window function, and the growth of structure, sensitive to both the expansion history and the relation between gravity and matter inhomogeneities, through the transfer function.

Lensing surveys such as Canada France Hawaii Legacy Telescope (CFHTLS) [30, 31, 32] and the HST COSMOS survey [33, 34] have provided the first generation of lensing data that have been used to test the nature of dark energy. Upcoming surveys such as the Dark Energy Survey (DES) [35] and the Large Synoptic Survey Telescope (LSST) [36] will provide higher precision lensing data with which different models of dark energy and modified gravity can be tested and distinguished.

Systematic errors in weak lensing measurements include intrinsic correlations (intrinsic alignments) in galaxy shapes, uncertainties/ errors in photometric redshift estimates of galaxies and errors in shape measurement arising from anisotropy of the point spread function (PSF) of the detector, atmospheric distortions and pointing errors amongst others. We will explain these systematics in detail in Chapter 5.

Cross-correlation of large scale structure observables

The ISW and lensing observations directly probe the properties of the gravitational potentials. On the other hand, galaxy number count measurements provide an estimate of the gravitational potential. To recover the distribution of all matter, both dark and baryonic (luminous), one needs information about the bias. However by using cross-correlation of galaxy counts, ISW and lensing variables one can reduce the sensitivity to bias [37]. With regards to understanding cosmic acceleration it has been shown that cross-correlations could provide a powerful tool with which to distinguish between modified gravtiy and dark energy [38, 39, 40, 41, 42, 43, 44, 45, 46, 47] .

1.4 Cosmic acceleration: the evidence

In this section we briefly review the observational evidence for the existence of a dark energy component in the universe., concentrating on the types of observation that have been introduced.

1.4.1 Constraints from Supernovae Ia

The direct evidence for the current acceleration of the universe is related to the observation of luminosity distances of high redshift supernovae [48, 49]. Until 1998, 42 SNe Ia had been discovered in the redshift range $z = 0.18$-0.83 by the Supernova Cosmology Project (SCP) [48], and 14 SNe Ia in the range $z = 0.16$-0.62 plus 34 nearby SNe Ia had been observed by the high-z Supernova Team (HSST) [49].

Assuming a flat universe, the SCP team found $\Omega_m = 0.28^{+0.09}_{-0.08}$ (1σ statistical) $^{+0.05}_{-0.04}$ (identified systematics), thus showing that about 70% of the energy density of the present universe consists of dark energy. In 2004 Riess *et al.* [50] reported the measurement of 16 high-redshift SNe Ia with redshift $z > 1.25$ with the Hubble Space Telescope (HST). By including 170 previously known SNe Ia data points, they showed that the universe exhibited a transition from deceleration to acceleration at > 99 % confidence level with a best-fit value of $\Omega_m = 0.29^{+0.05}_{-0.03}$ (68% confidence level).

Figure 1.4.1 shows the observational values of the luminosity distance d_L versus redshift z together with the theoretical curves derived from Eq. (1.33). This shows that a matter dominated universe without a cosmological constant ($\Omega_m^{(0)} = 1$) does not fit to the data. A best-fit value of $\Omega_m^{(0)} = 0.31^{+0.08}_{-0.08}$ was also obtained in a joint analysis of [51] which is consistent with the result of [50].

1.4.2 Constraints from the CMB

The observations related to the CMB support the ideas of a dark energy dominated universe [52]. Using the most recent WMAP data [52] with an assumption of a constant equation of state $w_{\mathrm{DE}} = -1$ for dark energy, then combining WMAP and the Supernova and BAO data implies $\Omega_K = -0.080^{+0.071}_{-0,093}$, consistent with a flat universe. In Fig. 1.4,the confidence regions coming from combined data is plotted. Clearly the flat universe with a cosmological constant is favored.

1.4.3 The age of the universe

Another evidence for the existence of dark energy emerges from the comparison of the age of the universe (t_0) to the age of the oldest stellar populations (t_s). One requires that $t_0 > t_s$, but it is difficult to satisfy this condition for a flat cosmological model with normal matter. On the other hand, the presence of dark energy (cosmological constant) can resolve this age problem.

The age of the oldest stellar objects have been constrained by different groups. The age of Globular clusters in the Milky Way are estimated as $t_1 = 13.5 \pm 2\,\mathrm{Gyr}$ from a distance-independent method [53]. Using the white dwarfs cooling sequence method, the age of the globular cluster M4 is constrained to be $t_1 = 12.7 \pm 0.7\,\mathrm{Gyr}$ [54, 55]. Then, the age of the universe needs to satisfy the lower bound: $t_0 >$ 11-12 Gyr.

The age of the universe is given by

$$\begin{aligned} t_0 &= \int_0^{t_0} dt = \int_0^{\infty} \frac{dz}{H(1+z)} \\ &= \int_0^{\infty} \frac{dz}{H_0 x [\Omega_r^{(0)} x^4 + \Omega_m^{(0)} x^3 + \Omega_\Lambda^{(0)} - \Omega_K^{(0)} x^2]^{1/2}}, \end{aligned} \tag{1.84}$$

where $x(z) \equiv 1+z$. We can neglect the contribution of the radiation term since the radiation dominated period is much shorter than the total age of the universe and the contribution of $z \gtrsim 1000$ is negligible. For a flat, matter-dominated universe we then obtain

$$t_0 \approx \frac{2}{3H_0}, \tag{1.85}$$

which does not satisfy the stellar age bound ($t_0 > 11$-12 Gyr). Hence a flat universe without a dark energy component suffers from an age problem. The observations of the CMB [52] constrain the curvature of the universe to be very close to flat, i.e., $|\Omega_K| = |\Omega_m - 1| \ll 1$, and therefore, the case of a non-flat universe can not be considered here.

On the other hand, a flat universe with a dark energy component (cosmological constant) ($\Omega_\Lambda \neq 0$) satisfies the constraint $t_0 > 11$-12 Gyr coming from the oldest stellar populations. In this case Eq. (1.84) gives

$$\begin{aligned} H_0 t_0 &= \int_0^\infty \frac{dz}{(1+z)\sqrt{\Omega_m^{(0)}(1+z)^3 + \Omega_\Lambda^{(0)}}} \\ &= \frac{2}{3\sqrt{\Omega_\Lambda^{(0)}}} \ln \left(\frac{1+\sqrt{\Omega_\Lambda^{(0)}}}{\sqrt{\Omega_m^{(0)}}} \right), \end{aligned} \tag{1.86}$$

where $\Omega_m + \Omega_\Lambda = 1$. When $\Omega_m = 0.3$ and $\Omega_\Lambda = 0.7$ one has $t_0 = 0.964 H_0^{-1}$, which corresponds to $t_0 = 13.1$ Gyr for $h = 0.72$ [8].

1.4.4 ISW signal from Cross-correlation of CMB and GC data

An independent evidence for the existence of dark energy ($\Omega_\Lambda \neq 0$) comes from the measurement of a non-zero ISW effect. During the matter domination era, the gravitational potential remains constant in a flat universe, which means that there will be no ISW produced in this era. On the other hand, in the presence of dark energy or if the geometry of the universe has curvature, the gravitational potential changes with time. Since the curvature of the universe is known to be very close to flat from the CMB data, an ISW signal can be attributed to a dark energy component.

Measurements of the ISW effect is difficult due to different reasons. First of all, ISW effect produces very small CMB anisotropy compared to the original anisotropy ($\sim 10\%$) [56]. Also, there is no small scale ISW effect since the produced anisotropies, positive and negative, will cancel out. The large scale ISW signal, on the other hand, is limited by the cosmic variance.

This problem can be solved by measuring the correlations between the ISW effect and the density of galaxies. The cross-correlation power spectrum, $C_\ell^{G\,ISW}$, can be derived using

Eqs. (1.76) and (1.78). From a combination of large scale structure and CMB data, $C_\ell^{G\ ISW}$ is measured to be non-zero on large scales confirming the existence of dark energy [56].

1.5 ΛCDM model

The Λ-Cold Dark Matter (ΛCDM) or the *concordance* model is the standard model of cosmology at present. It is the simplest known model that is in agreement with the observational data so far. The main assumptions in the ΛCDM model is that: The dark energy component in the universe is a Cosmological Constant (CC) with $\Omega_\Lambda \approx 74\%$; the dark matter component is mostly cold ($v_{CDM} << c$) with $\Omega_{CDM} \approx 22\%$; and $\Omega_{baryons} \approx 4\%$ for baryonic matter. The model assumes a nearly scale-invariant spectrum of primordial perturbations and a flat universe which is much larger than the observable particle horizon due to the cosmic inflation.

While the ΛCDM model is simple and agrees very well with the data, it suffers from a series of theoretical, philosophical and observational inconsistencies. These issues have been summarized as follows:

The cosmological constant problem:

In the ΛCDM model, the CC emerges from the vacuum energy. The total vacuum energy is the sum over contributions from all the quantum fields:

$$\rho_{vac} = \frac{1}{2} \sum_{particles} g_i \int_0^{k_{max}} \frac{d^3k}{(2\pi)^3} \sqrt{k^2+m^2}\,, \tag{1.87}$$

where $g_i = (-1)^{2j}(2j+1)$ is the *degeneracy factor* for a particle of spin j. ρ_{vac} is dependent on the cutoff value k_{max} and should be comparable to the vacuum energy today:

$$\rho_{vac} \sim \rho_{crit} \sim 10^{-47} GeV^4\,. \tag{1.88}$$

All the physically meaningful cutoff scales fail to provide a comparable value for vacuum energy, and the discrepancies are orders of magnitude. For example, a Planck scale cutoff would give $\rho_{vac} \sim 10^{74} GeV^4 \sim 10^{123} \rho_{crit}$. Applying a QCD or supersymmetry cutoff scale would remove many order of magnitudes of the discrepancy, but still a significant fine tunning would be needed. This is also referred to as the *old* cosmological constant problem [58].

The coincidence problem:

The energy density of the different constituents in the universe change very differently as the universe expands (Fig. 1.5). This raises the suspicion of why the accelerated expansion should occur at present, not at any other time in the long history of the universe. This is referred to as the *new* cosmological constant problem by Weinberg [58].

Massive neutrinos:

Neutrinos are assumed to be massless in ΛCDM. It wasn't until the Super-Kamiokande [59] and SNO [60] experiments that the detection of neutrino flavor oscillations proved non-zero mass for these species. Since then, constraining the masses of different neutrino generations have become an important goal of particle physics and cosmology experiments. Particle physics limits on the neutrinos mass are obtained from beta-decay [61] and neutrinos oscillations [62]. The neutrino oscillation experiments provide the following relations for the difference between the squared masses of 3 neutrino generations:

$$\begin{aligned} |\Delta m^2_{31}| = |m^2_3 - m^2_1| &= 2.2^{+1.1}_{-0.8} \cdot 10^{-3}\mathrm{eV}^2\,, \\ \Delta m^2_{21} = m^2_2 - m^2_1 &= 7.9^{+1.0}_{-0.8} \cdot 10^{-5}\mathrm{eV}^2\,. \end{aligned} \tag{1.89}$$

Cosmological experiments on the other hand are not sensitive to neutrino flavors but are mainly sensitive to the total neutrino mass and to some extent to their mass hierarchy. The combination of today's cosmological data provide an upper limit of $\sum m_\nu < 0.3\mathrm{eV}$ [63].

1.6 Alternatives to CC dark energy of the ΛCDM model

In the absence of a plausible theoretical explanation of the nature of dark energy, alternative ideas have been investigated to describe the accelerated expansion of the universe. These ideas can be classified in two main categories.

The first category includes theories that propose a dark energy component, other than CC, in the universe. In this case, the interaction of space-time with the constituents of the universe remains the same. It is the right hand side of the Einstein equations, Eq. (1.18), which are modified. A popular idea here is the use of a scalar field, as the dark energy component, rolling down a potential. When the energy density of the scalar field dominates (at recent time), the acceleration expansion of the universe emerges from the dynamics of the scalar field, very much like what happens with the inflaton during inflation. In Chapter 2, we describe these theories and their observational consequences in detail.

The second class involves ideas which modify the way in which space-time behaves in the interaction with the contents of the universe. In this case, the left hand side of Einstein equations, Eq. (1.18), are modified. This corresponds to a modification to the gravity theory used in the ΛCDM, namely, GR. These *modified gravity* theories can be seen as an alternative to theories of dark energy. In Chapter 3 we review these theories in detail.

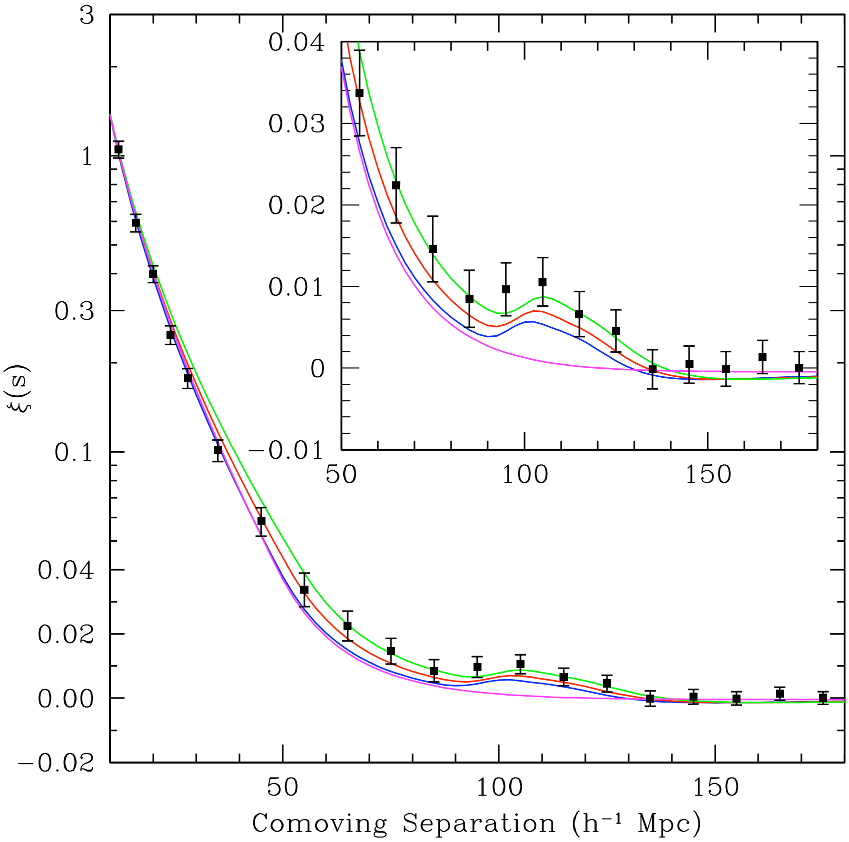

Figure 1.1: The galaxy correlation function, ξ, from the Sloan Digital Sky Survey, clearly showing the baryon acoustic correlation at $100h^{-1}Mpc$. The curves are models with $\Omega_m h^2$= 0.12 (top), 0.13 (second) and 0.14 (third), where $\Omega_b h^2$= 0.024 in all the cases. The bottom curve is for a model without baryons (pure CDM model) and hence no BAO bump. From [20]; used with permission.

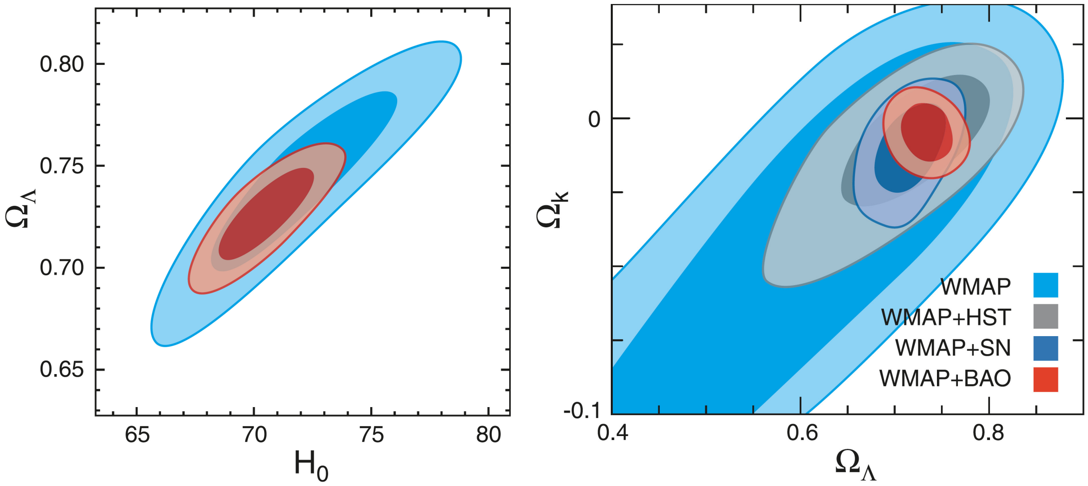

(a) $\Omega_\Lambda - H_0$ (b) $\Omega_k - \Omega_\Lambda$

Figure 1.2: Constraints on some of the cosmological parameter space for the WMAP 5-year CMB data, Sloan Sky Digital Survey (SDSS) BAO [21] and Supernova Cosmology Project (SCP) Union supernovae constraints [22]. Used with permission from WMAP team.

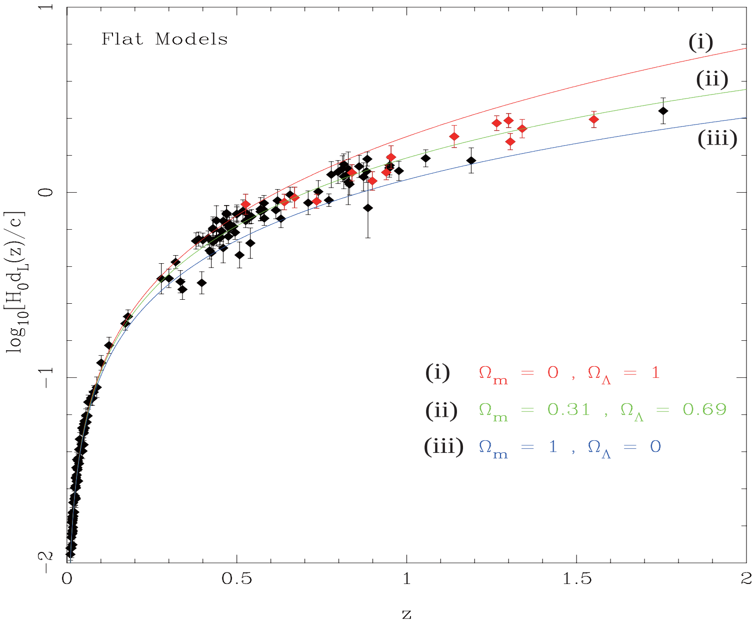

Figure 1.3: The luminosity distance $H_0 d_L$ versus the redshift z for a flat cosmological model. The black points come from the "Gold" data sets [50], whereas the red points show the recent data from HST. Three curves show the theoretical values of $H_0 d_L$ for (i) $\Omega_m = 0$, $\Omega_\Lambda = 1$, (ii) $\Omega_m = 0.31$, $\Omega_\Lambda = 0.69$ and (iii) $\Omega_m = 1$, $\Omega_\Lambda = 0$. From [51]; used with permission.

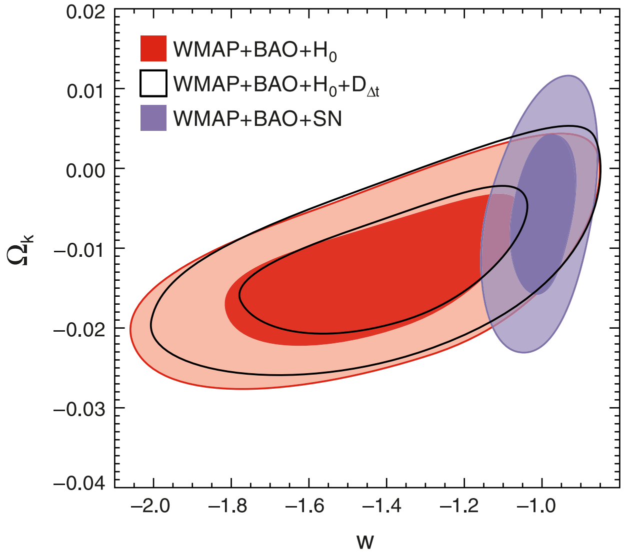

Figure 1.4: Joint two-dimensional marginalized constraint on the dark energy equation of state, w, and the curvature parameter, Ω_k. From [52]; used with permission.

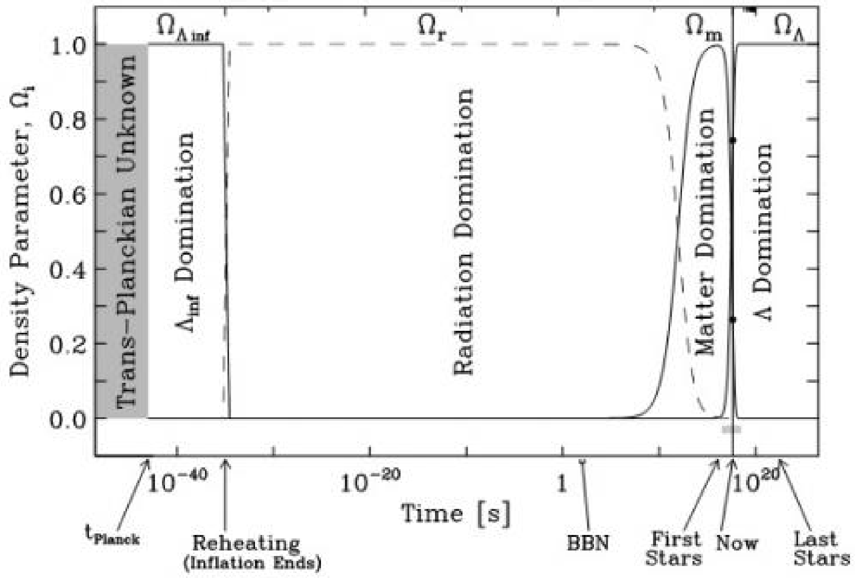

Figure 1.5: Time dependence of the densities of the different components of the universe. The comparable density of dark energy and matter today is the origin of the coincidence problem. From [57]; used with permission.

Chapter 2

Dark energy and observational constraints

Discovery of an accelerated expansion of the universe has been one of the most important achievements of cosmology in the 20th century. It is a well established fact these days and those who discovered it received a Nobel prize. As described before, ΛCDM is a simple model providing the conditions we need for acceleration via the energy of the vacuum with a constant EoS, $w = -1$. Current experimental constraints on w, however, are not precise enough to rule out the possibility of a dynamics in it. Therefore, it is of fundamental importance to know whether DE is a static component or dynamical. Future observations will be sensitive enough to address this question [64].

The similarity between the situation here and that of inflation has inspired physicist to consider new degrees of freedom (DoF), usually a scalar DoF, that can produce acceleration and eliminates the need for a CC by attributing the missing energy to this new DoF, a scalar field for example.

In the next section, we review the alternative theories to CC that have been introduced in the literature to describe a (dynamical) DE component in the universe. Then, we describe how DE properties are determined from observations and briefly review the model-independent parametrizations applied to constrain the effective EoS of DE. Finally, we explain in detail, a model-independent approach to constrain w using wavelets.

2.1 Scalar field DE

A popular alternative to CC is a scalar field component that produces the observed acceleration with a dynamics similar to that of inflation. The most general way a scalar field can appear in the action is

$$S = \int d^4x\sqrt{-g}\left[\frac{f(\phi)}{16\pi G}R + \mathcal{L}_\phi(\phi, \partial\phi) + \mathcal{L}_m(\phi, \Psi_i)\right], \tag{2.1}$$

where $f(\phi)$ term corresponds to a non-minimal coupling between ϕ and gravity, $\mathcal{L}_\phi$ is a non-canonical Lagrangian for the scalar field [1], and the final term is the matter Lagrangian including a non-minimal coupling between normal matter species Ψ_i and ϕ.

A non-minimal coupling between ϕ and gravity ($f(\phi) \neq 1$) will result in an effective Newton constant, G_{eff}, which could be a function of space-time in general. We study such cases in Chapter 3. Several of the other possibilities leading to a DE component capable of causing an acceleration phase are briefly reviewed below.

2.1.1 Quintessence DE

The simplest form of Eq. (2.1) includes a scalar field, known as *quintessence*, with a general action written as

$$S = \int \mathrm{d}^4x\sqrt{-g}\left[-\frac{1}{2}(\nabla\phi)^2 - V(\phi)\right], \tag{2.2}$$

where $(\nabla\phi)^2 = g^{\mu\nu}\partial_\mu\phi\partial_\nu\phi$ and $V(\phi)$ is the potential of the field. The field obeys the Klein-Gordon equation

$$\Box\phi - V_{,\phi} = 0, \tag{2.3}$$

where $V_{,\phi} \equiv \partial V/\partial\phi$. In an expanding FRW universe, this equation reduces to

$$\ddot{\phi} + 3H\dot{\phi} + V_{,\phi} = 0. \tag{2.4}$$

---

[1] The canonical form of the Lagrangian for a scalar field (ϕ) is defined in Eq. (2.2).

The 00 and *ii* components of the energy-momentum tensor of the scalar filed, $T_{\mu\nu}^{(\phi)}$, give its energy density and pressure

$$\begin{aligned} \rho_\phi &= \frac{1}{2}\dot{\phi}^2 + V\,, \\ P_\phi &= \frac{1}{2}\dot{\phi}^2 - V\,. \end{aligned} \tag{2.5}$$

When quintessence field is the dominant component in the universe, the Friedmann and acceleration equations are

$$H^2 = \frac{8\pi G}{3}\left[\frac{1}{2}\dot{\phi}^2 + V(\phi)\right]\,, \tag{2.6}$$

$$\frac{\ddot{a}}{a} = -\frac{8\pi G}{3}\left[\dot{\phi}^2 - V(\phi)\right]\,. \tag{2.7}$$

If, in Eq. (2.4), $m \equiv \sqrt{V_{,\phi\phi}} >> H$ so that the *Hubble friction* term ($3H\dot{\phi}$) is negligible, the scalar field simply moves toward the minimum of the potential and oscillates at the minimum. On the other hand, if $m << H$ so that the Hubble friction overdamps the oscillator and the conditions

$$\begin{aligned} \ddot{\phi} &\ll H\dot{\phi}\,,\, V_{,\phi}\,, \\ 3H\dot{\phi} &\simeq -m^2\phi\,, \end{aligned} \tag{2.8}$$

apply, then the field slowly rolls down the potential so that $\dot{\phi}^2 < V(\phi)$ and a positive acceleration condition is achieved from Eq. (2.7). In the slow-roll state, the effective EoS is

$$w_\phi = \frac{P_\phi}{\rho_\phi} \approx -1\,. \tag{2.9}$$

So far, we have just provided an alternative mechanism to the Λ dark energy for producing acceleration. It is the quintessence potential that determines the expansion history and the onset of DE domination and thus, the accelerated expansion of the universe. To apply the quintessence as a realistic DE model, different issues must be addressed. For example, the scalar field needs to be very light ($m_\phi \lesssim H \sim 10^{-42}$GeV) for the slow-roll state to happen, and should remain non-interacting with the standard model particles. Even then, there would still be some fine tuning involved to achieve the late-time dynamics we expect. Two classes of quintessence models that have been extensively studied in the literature and have been shown to produce acceleration are based on the power-law and exponential potentials.

Power-law potentials

Inspired by supersymmetry theories [65, 66], power-law potentials of the form

$$V(\phi) = V_0\, \phi^{-n}\,, \tag{2.10}$$

are shown to produce accelerated expansion at late times. For a wide range of initial conditions, the scalar field approaches a universal track and is therefore called a *tracker field* [8, 67, 68, 69]. The EoS is negative, so that the scalar field inevitably dominates at late times, and will go asymptotically to $w_\phi = -1$. When subdominant, the EoS follows the effective background EoS, w_B, as [8]

$$w_\phi \approx (n w_B - 2)/(n+2)\,. \tag{2.11}$$

With these models, the coincidence problem is often claimed to be naturally solved by having the scalar field's energy density tracking the effective background EoS and dominating at late times. There is still a fine-tuning involved to achieve acceleration now, rather than any other time.

Exponential potentials

Exponential potentials of the form

$$V = V_0\, e^{-\lambda\phi}\,, \tag{2.12}$$

can be found in many extensions of the standard model of particle physics and provide the desired acceleration. When $\lambda^2 > 3(1+w_B)$, the energy density of the field tracks the background fluid ($w_\phi = w_B$), while for $\lambda^2 < 2$, there are accelerating solutions [70]. However, these solutions track the scaling behavior of matter ($w_\phi = w_{matter}$) and do not convert into dark energy at late times. In this case, a viable acceleration is achieved in other ways such as combining more than one exponential potentials, or by non-minimal coupling to matter [8].

2.1.2 General scalar field models

In addition to working with a scalar field that is minimally coupled to gravity, extensions to Eq. (2.2) have been considered that can lead to the desired dynamics. We briefly review some of these generalized forms here.

Scalar fields with non-canonical Lagrangian

An action of the form

$$S = \int d^4x\sqrt{-g}\mathcal{L}(X,\phi)\,, \tag{2.13}$$

where $X \equiv -\frac{1}{2}g^{\mu\nu}\partial_\mu\phi\partial_\nu\phi$ can provide an alternative scenario for acceleration. The Lagrangian can contain terms including non-trivial functions of X or combinations of X and ϕ. An example is the *k-essence* model with

$$\mathcal{L} \equiv K(X) - V(\phi)\,, \tag{2.14}$$

where $K(X)$ is the non-canonical kinetic term. This theory can be viewed as a low-energy analogue of *k-inflation* motivated by the low-energy effective action in string theory [71, 72, 73, 74]. The resulting stress-energy tensor is

$$T_{\mu\nu} = \mathcal{L}_{,X}(\nabla_\mu\phi)(\nabla_\nu\phi) + \mathcal{L}g_{\mu\nu}\,, \tag{2.15}$$

which gives an EoS as

$$w = \frac{K-V}{2XK_X - K + V} = -1 + \frac{2XK_X}{2XK_X - K + V}\,, \tag{2.16}$$

where $K_X \equiv dK/dX$.

Scalar fields with non-minimal coupling to matter

For a scalar filled non-minimally coupled to matter, the action is

$$S = \int d^4x\sqrt{-g}\left[\frac{1}{2}M_{\rm p}^2 R - \frac{1}{2}(\nabla\phi)^2 - V(\phi)\right] + \sum_j S_{\rm j}[e^{2\alpha_{\rm j}(\phi)}g_{\mu\nu}, \Psi_{\rm j}], \tag{2.17}$$

where $\alpha_{\rm j}(\phi)$ are coupling functions between the j-th matter sector and the scalar field. The Friedmann and fluid equations for matter are

$$3M_p^2 H^2 = \frac{1}{2}\dot{\phi}^2 + V(\phi) + \sum_{\rm j} e^{\alpha_j(\phi)}\rho_{\rm j}, \tag{2.18}$$

$$\dot{\rho}_{\rm j} + 3(1+w_{\rm j})H\rho_{\rm j} = -3w_{\rm j}e^{\alpha_j(\phi)}\rho_{\rm j}\alpha_{\rm j}'(\phi)\dot{\phi}, \tag{2.19}$$

and the scalar field obeys a forced oscillatory equation

$$\ddot{\phi} + 3H\dot{\phi} + V'(\phi) = -\sum_{\rm j}\alpha_{\rm j}'(\phi)(1-3w_{\rm j})e^{\alpha_j(\phi)}\rho_{\rm j}. \tag{2.20}$$

From certain conditions, an acceleration phase can be achieved in these theories through a negative EoS

$$w = -1 + \frac{1}{24\pi G}(\frac{V'}{V})^2. \tag{2.21}$$

2.2 Other theories of DE

2.2.1 Mass-varying neutrinos (MaVaNs)

The idea in this theory is that the comparable mass of neutrinos and the CC mass-scale, $m_\Lambda \equiv \Lambda^{1/4} \sim 10^{-3}$ eV, might mean that cosmic acceleration and neutrinos are related [83, 84]. Here, similar to quintessence, a scalar field called *scalaron* is rolling down a potential with its value coupled to the neutrino mass. The advantage of these models is that the dark energy density can be almost constant without the need of slow rolling a flat potential. A generic instability in these theories, however, leads to large spatial perturbations in the energy density of the neutrinos, inconsistent with observations [85, 86].

2.2.2 Phantom DE

As mentioned before, observational data allow for small deviation from $w = -1$ and are consistent with a $w < -1$. In the simplest form, this behavior can be achieved from a scalar field with a negative kinetic energy [87]. The action in this case is written as

$$S = \int \mathrm{d}^4x\sqrt{-g}\left[\frac{1}{2}(\nabla\phi)^2 - V(\phi)\right], \tag{2.22}$$

with the EoS

$$w = \frac{p}{\rho} = \frac{\dot{\phi}^2 + 2V(\phi)}{\dot{\phi}^2 - 2V(\phi)}, \tag{2.23}$$

where $w_\phi < -1$ for slow rolling condition. The property of these models is that they violate the null energy condition:

$$T_{\mu\nu}\, n^\mu\, n^\nu \geq 0, \tag{2.24}$$

where n^μ is a null vector. For a perfect fluid, the null energy condition is

$$P + \rho \geq 0. \tag{2.25}$$

As a result of violating this condition, the energy density of the scalar field grows with time, rather than decaying. The cosmological consequence of this behavior would be a divergent expansion of the universe in finite time, an early *big rip* [88, 89]. These models also contain ghosts [116] and, generally, are not considered to be a viable DE model [116].

2.2.3 Chaplygin gas

In this class of DE models a fluid, *Chaplygin gas*, is responsible for the acceleration of the universe through an EoS of the form

$$P = -\frac{A}{\rho}, \tag{2.26}$$

where A is a positive constant. This form of EoS is motivated from the extra-dimension theories [90, 91, 92], and provides the possibility of unification of DE and DM. However, these models provide a strong ISW effect and have difficulty fitting the CMB data. The generalized Chaplygin gas model solves this problem to some extent [93] by modifying Eq. (2.26) as

$$P = -A/\rho^{\alpha}, \tag{2.27}$$

where $0 < \alpha < 1$, at the cost of tight constraints on α from observational data [94].

2.3 Observation of DE and constraining its EoS

For DE, the main quantities to measure are its energy density and its EoS, w, which could be changing with time. $\Omega_{\rm DE}(z)$ can be calculated from measurements of the Hubble parameter. For a universe dominated with DE and matter, one can rewrite Eqs. (1.19) and (1.20) as

$$H^2 = \frac{8\pi G}{3}(\rho_{DE} + \rho_m), \tag{2.28}$$

$$\dot{H} = -4\pi G(\rho_{DE} + p_{DE} + \rho_m + p_m). \tag{2.29}$$

The Hubble parameter itself can be calculated from the luminosity distance data, Eq. (1.35):

$$d_L = (1+z)\int_0^z \frac{dz'}{H(z')}. \tag{2.30}$$

$\Omega_{\rm DE}(z)$ is also related to $w(z)$ via

$$\Omega_{\rm DE}(z) = \Omega_{\rm DE}^{(0)} \exp\left\{-3\int d\ln z'[1+w(z')]\right\}, \tag{2.31}$$

where $\Omega_{\rm DE}^{(0)}(z)$ is the fractional energy density of DE today.When working with a specific model of DE, w can be calculated based on the parameters of that model and a functional form of $w(z)$ or the Hubble parameter $H(z)$ is fit to data. For example, the scalar field models described above [8] give analytical expressions for w and have predictions for its behavior with redshift. Many of these expressions have been considered [95, 96, 97, 98] and the results are forecasted in terms of constrains on the model parameters. The general issue with this approach is that the results are strongly dependent on the assumed model.

Alternatively, one can take a phenomenological approach and parametrize the EoS in a general way. In that case, the goal would be to come up with the least model-dependent parametrization that can constrain w with a minimum number of parameters.

2.3.1 Model-independent representation of w

w is a continuous function with infinite DoF and data can never completely constrain it. Hence, any function or parametrization that is used to acquire information about $w(z)$, inevitably introduces some model-dependence. Much effort has been put in extracting $w(z)$ from data, in the most model-independent and efficient way. Approaches taken so far to estimate w from data can be classified into the followings.

Parametric forms

w can be expressed in terms of parametric functions, which are inspired by a general functional form w has in a class of theories, or are purely phenomenological. Some of the widely used parametric function in the literature are [99]:

- Constant w: which covers *wCDM* models as well as ΛCDM model.
- Power-law: $w(z) = \sum_n w_n \, z^n$.
- Logarithmic function: $w(z) = \sum_n w_n \, [\log(1+z)]^n$.
- *Kink* approach where $w(a) = w_0 + (w_m - w_0)\Gamma(a, a_t, \Delta)$ with Γ being a transition function, and other similar parametrizations.

In principle, one can consider as many terms as desired but data limits the number of well-constrained parameters. Hence, usually, a few terms are considered [100, 101, 102, 103].

Binning

A common approach to parametrizing w is an expansion into a basis

$$w(z) = \sum_n w_n \, x_n(z) \,, \tag{2.32}$$

where, here, w_n are the expansion coefficients. The binning method is an example of such expansions where the basis are w bins in redshift (or scale factor) [106, 107, 108], so that in Eq. (2.32)

$$x_n(z) = \begin{cases} 1 & \text{if} \quad z_n < z < z_{n+1} \\ 0 & \text{Otherwise} \end{cases} \tag{2.33}$$

where z_n and z_{n+1} specify the beginning and the end of a redshift bin. This approach has been modified in different ways. For example, instead of a sharp transition to the next bin value, one can have a smooth transition using hyperbolic tangent functions [109], or efficient methods can be applied to control bias in EoS [110].

The basis functions can be chosen to be orthogonal, and it has the benefit that in principle, the errors we get on the expansion coefficients are not correlated.

Direct reconstruction

In this method, $w(z)$ or Hubble parameter is reconstructed by a direct differentiation of luminosity distance data. From Eq. (2.30), the Hubble parameter $H(z)$ can be expressed as

$$H(z) = \left\{ \frac{d}{dz} \left(\frac{d_L(z)}{1+z} \right) \right\}^{-1}, \tag{2.34}$$

and $w(z)$ can be obtained from differentiating Eq. (2.31). For example, in [111], Type Ia SNe luminosity distance data is smoothed, and $w(z)$ is calculated from the second derivative of this smoothed function. Although model-independent in nature, this approach needs application of some smoothing and differentiating methods which are model-dependent. Also, lack of enough data points to perform a precise smoothing and differentiating procedure causes relatively large uncertainties in $w(z)$.

2.3.2 How many parameters to fit

Observational constraints on $w(z)$ are sensitive to how we parametrize it. Hence, an important question is: how many parameters do we need to describe $w(z)$ and its possible dynamics? To judge whether a model is preferred by data, the following selection criteria are commonly used:

- The improvement in χ^2 per extra degree of freedom, $\Delta\chi^2/\Delta(\text{DoF})$, with

$$\chi^2 = (\mathbf{x}-\mathbf{d})^T \mathbf{C}^{-1} (\mathbf{x}-\mathbf{d}) \tag{2.35}$$

where **x** is theoretical value for an observable, **d** is data vector and **C** is the data covariance matrix.

- Akaike Information Criterion (AIC) [112]

$$\mathrm{AIC} = -2\log L + 2N_p + \frac{2N_p(N_p+1)}{N_d - N_p - 1}\,, \tag{2.36}$$

where L is the likelihood function of the model [2], N_p is the number of parameters and N_d is the number of data points.

- Bayesian Information Criterion (BIC) [113, 114]

$$\mathrm{BIC} = -2\log L + \frac{N_p N_d \log(N_d)}{N_d - N_p - 1}\,, \tag{2.37}$$

The second terms on the right hand sides of Eqs. (2.36) and (2.37) show the penalty for adding new parameters, which is stronger for BIC. Both expressions include second-order corrections, which is important for the case with a small data sample size, i.e. small N_d. The AIC and BIC are widely used in the model selection – the lower the value of AIC (BIC), the more the model is preferred. A model with $\Delta\mathrm{BIC} < -10$ is decisively preferred, while models with $-10 \leq \Delta\mathrm{BIC} < -6$, $-6 \leq \Delta\mathrm{BIC} < -2$ and $\Delta\mathrm{BIC} \geq 2$ have very strong, strong and weak evidence of model preference, respectively. In the case of the AIC, models with $\Delta\mathrm{AIC} \leq 2$ have substantial support, models with $4 \leq \Delta\mathrm{AIC} \leq 7$ have considerably less support and those with $\Delta\mathrm{AIC} > 10$ have essentially no support.

2.3.3 Principal Component Analysis

As mentioned above, ideally, many parameters are needed to precisely constrain $w(z)$. On the other hand, information provided by data is limited. Hence, as one increases the number of parameters in a model, their constraints weaken. The other challenge is that the parameters are usually correlated, so that making inference about each parameter is dependent on the other parameters.

---

[2] For Gaussian probability distributions $-2\log L \equiv \chi^2$.

Principal component analysis (PCA) is a procedure that transforms a set of correlated parameters into a set of uncorrelated parameters called *principal components* (PCs) or *modes*. PCs are sorted so that the first principal component corresponds to a direction in the *old* parameter space that accounts for the minimum possible variance in the data, and the succeeding components are sorted according to the variance they represent. Decorrelation is done by simply diagonalizing the covariance matrix of the original parameters. We have

$$C \equiv W^T \, \Lambda \, W \,, \tag{2.38}$$

where C is the original covariance matrix, Λ is a diagonal matrix and W is the *decorrelation* matrix W. The rows of W of the are the eigenvectors e_i, which define the basis in which our parameters are uncorrelated. Since C is real and symmetric, W can be chosen to be orthogonal and of unit determinant, so that e_i form an orthonormal basis [106]. In the new basis, the errors are autocorrelated (the new covariance matrix is diagonal) .

In the case of binned $w(z)$ described by Eq. (2.33), the bin values are intrinsically correlated. To see why, one should note from Eq. (2.31) that it is the integral of $w(z)$ which enters the Hubble parameter, Eq. (2.29). Distance measurements such as luminosity distance, Eq. (2.30), involve the Hubble parameter in calculation of the comoving distances. Hence, data probes the integral of $w(z)$ from today ($z = 0$) to a certain redshift, so that the error on the value of a bin is dependent on the errors on the values of the bins at lower redshifts.

Treating the bin values as parameters of the model, their covariance matrix can be computed by fitting them to data (or from a forecast as we will see later). The covariance matrix can then be decorrelated using PCA. From Eq. (2.38), we have

$$W_{im} = e_i(z_m) \,, \tag{2.39}$$

where $e_i(z_m)$ are the eigenvectors at the m-th bin. $w(z)$ can then be expanded in the new basis as

$$w(z) = \sum_{i=1}^{\#\text{ of bins}} \alpha_i \, e_i(z) \,, \tag{2.40}$$

where the expansion coefficients α_i are

$$\alpha_i = \sum_{m=1}^{\text{\# of bins}} w(z_m)\, e_i(z_m)\,. \tag{2.41}$$

The eigenvalues of C, which are the diagonal elements of Λ, determine how well-constrained the corresponding PCs are.

It is argued that in the absence of a compelling theoretical argument for any particular parameterization of w except $w(z) = -1$, the PC basis is the natural basis in which the function $w(z)$ should be considered [106]. The error of measurement of w at a given redshift, z_m is

$$\sigma(w(z_m)) = \left(\sum_{i=1}^{\text{\# of bins}} \sigma^2(\alpha_i)\, e_i^2(z_m) \right)^{1/2} . \tag{2.42}$$

The best-determined modes are better determined than the best-determined *original* components, bin values w_i, while the worst-determined modes are determined more poorly than the worst-determined w_i [106].

2.4 Wavelet method

Here, we examine the possibility of using wavelets as a tool to detect possible features in $w(z)$ [115]. Sharp features in $w(z)$ would exist if, for example, dark energy was a quintessence scalar field with a potential that had a step-like bump. Such features are also predicted in certain types of phantom models of DE [116]. Wavelets, known as "mathematical microscopes", are specially designed functions that have the property of being localized in both frequency and configuration space. As a result, wavelets have the ability to "see" signals on multiple scales, making them a powerful tool for detecting features in noisy data.

Wavelets have been used in cosmology for reconstructing the primordial power spectrum [117, 118], probing the non-Gaussianity of the primordial fluctuations [119], and searching for signals of parity breaking [120].

2.4.1 The wavelet parametrization

Wavelets are generated from a "mother" function as

$$\psi_{nm}(x) = \left(\frac{2^n}{L}\right) \psi\left(\frac{2^n\, x}{L} - m\right) \tag{2.43}$$

where $\psi(x)$ is the mother function, L is the range on which the function is defined, $0 < m < 2^n - 1$ and $0 < n < N - 1$, where N specifies the resolution so that number of data points equals 2^N. Each wavelet function has a localized shape. The index n determines the size of the feature, while m determines its location on x. Functions ψ_{nm} are orthogonal by design, hence we can expand any function onto the wavelet basis in the same way as we do for any other orthogonal basis:

$$f(x) = \sum_{n=0}^{N-1} \sum_{m=0}^{2^n-1} a_{nm} \psi_{nm}(x) \ . \tag{2.44}$$

By this definition, each wavelet acts as a band-pass filter and an infinite number of wavelets are needed to cover the whole spectrum. This problem is solved by introducing a scaling function which covers the spectrum up to a scale, after which is covered by the wavelet functions. Wavelets coefficients together with the coefficient of the scaling function, 2^N in total, can be used to describe $f(x)$ at 2^N points.

We consider $w(z)$ to be an unknown function which can, in principle, have local features in z. Like any other function, we can expand it into the wavelet basis as

$$1 + w(z_j) = \sum P_i \psi_i(z_j) \ , \tag{2.45}$$

where z_j are the redshift points at which we calculate w, P_i are the wavelet expansion coefficients, and ψ_i are the wavelet functions. We chose to simplify our indices so that P_1 is the scaling function coefficient, $P_2 = a_{00}$, $P_3 = a_{10}$, etc. We then treat the wavelet expansion coefficients as the parameters of the model to be measured from data. Note that we expand $1 + w(z)$, as opposed to $w(z)$, so that all coefficients are zero if $w = -1$, as in the currently favored ΛCDM model.

We use Daubechies 4 (D4) [121] and Haar [122] wavelets (prototypes shown in Fig. 2.1). The D4 wavelets are highly localized and suitable for reconstructing sharp features. The Haar wavelets are made of step functions. We should keep in mind that our results using

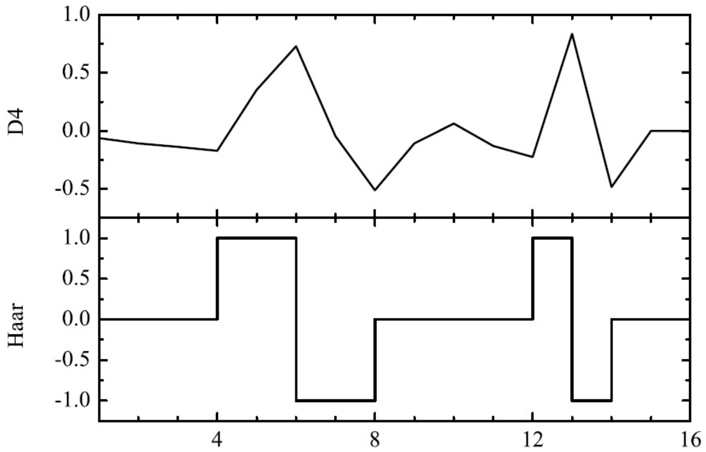

Figure 2.1: The 5th and 15th D4 (upper) and Haar (lower) wavelets. The resolution (16 points) in this illustration is the same as the one used in the numerical calculations of this section. From [115].

different types of wavelets should converge and be consistent with each other in the limit of large number of data points.

The redshift range is chosen based on the expected coverage range of the SNe survey we consider. Here, we take the redshift range to be $0 < z < 1.7$ according to future survey specifications. We choose to work with up to 16 wavelet parameters, which allows us to calculate $w(z)$ at 16 equally spaced points in z and probe features of order $1.7/8 \approx 0.2$ size in redshift. The values of the wavelet coefficients are determined by fitting (2.45) to data using Markov-chain Monte Carlo (MCMC).

The main advantage of wavelets is that we do not need a prior knowledge of the position and the scale of the possible features in the function $w(z)$. Wavelets search for large and small scale features at the same time and, since they are localized in configuration space, it is possible to reconstruct local features with only a few nonzero coefficients.

In practice, we start with performing an initial MCMC run with all 16 wavelet coefficients as free parameters. We then keep those parameters whose signal-to-noise ratio (SNR) is above a certain threshold, and set parameters with low SNR to zero, since they are not sensitive to features in $w(z)$. From the surviving set of wavelet coefficients, we find the combination that has the lowest reduced χ^2. This gives us the optimal number of wavelets we need to detect a feature in $w(z)$. We then use the model selection criteria, described in

$z \rightarrow$	0.1	0.2	0.3	0.4	0.5	0.6	0.7	0.8	0.9	1.0	1.1	1.2	1.3	1.4	1.5	1.6	1.7
$N(z)$	300	35	64	95	124	150	171	183	179	170	155	142	130	119	107	94	80
$\sigma_m(z)$ $(\times 10^{-3})$	9	25	19	16	14	14	14	14	15	16	17	18	20	21	22	23	26

Table 2.1: The redshift distribution of type Ia supernovae $N(z)$ for a futuristic SNe Ia survey [123], together with 300 SNe from the NSNF [124]. The redshifts given are the upper limits of each bin. Magnitude errors $\sigma_m(z)$ are evaluated at bin midpoints.

2.3.2, to determine if the wavelet fit is in fact preferred over a constant w.

2.4.2 Data

We work with a combination of SNe, CMB and BAO data, considering both the current [3] available data and the simulated future data. The combined likelihood of the model is calculated as

$$-2\log\mathcal{L} = \chi^2_{total} = \chi^2_{\rm SNe} + \chi^2_{\rm CMB} + \chi^2_{\rm BAO}\,. \tag{2.46}$$

SNe Ia data

The observable quantity in SNe Ia data is the redshift-dependent magnitude, Eq. (1.59). We use the characteristics of a futuristic survey [123] to simulate the SNe Ia data with errors given by

$$\sigma_m(z) = \sqrt{\frac{\sigma^2_{\rm obs}}{N_{\rm bin}} + {\rm d}m^2}\,, \tag{2.47}$$

where $\sigma_{\rm obs} = 0.15$. The systematic error, dm, is assumed to increase linearly with redshift:

$${\rm d}m = \delta m \frac{z}{z_{\rm max}}, \tag{2.48}$$

δm being the expected uncertainty and $z_{\rm max}$ the maximum redshift. Table 2.1 shows the redshift distribution of type Ia supernovae expected to be detected by the survey together with estimated error in magnitude for different redshift bins.

For current SNe Ia data, we use the "Constitution" sample with 397 data points [136].

---

[3] As of 2009.

CMB and BAO data

Rather than working with the full CMB data, we use the procedure suggested in [125] and work with two distance ratios: the *shift parameter* R, and the *acoustic scale* ℓ_A, defined as

$$
\begin{aligned}
R(z_*) &= \frac{\sqrt{\Omega_m H_0^2}}{c}(1+z_*)D_A(z_*) && (2.49)\\
\ell_A &\equiv (1+z_*)\frac{\pi D_A(z_*)}{r_s(z_*)} && (2.50)
\end{aligned}
$$

where z_* is the redshift of decoupling, $D_A(z)$ is the proper angular diameter distance to redshift z, and $r_s(z)$ is the comoving sound horizon at z. It was shown that these two quantities contain almost all of the information required to constrain dark energy with CMB [126, 127, 128].

For future CMB data, we use the Planck characteristics for parameters and their errors [129]. For today's CMB data we used the WMAP-5 values and errors for the parameters [125].

We use the BAO data point at $z = 0.35$ from [130] corresponding to $r_s/D_V(z)$, where $D_V(z)$ is given by

$$
D_V = \left[(1+z)^2 D_A^2(z)\frac{cz}{H(z)}\right]^{1/3}, \qquad (2.51)
$$

where c is the speed of light.

2.4.3 Features in $w(z)$

Broad features in $w(z)$, such as a single transition from one constant value to another, can be efficiently detected by other methods such as binning. Our aim is to detect, if any, local features in w(z) in a least model-dependent way. In this case, wavelets can do a good job phenomenologically. Wavelet method is more effective for searching for localized features in $w(z)$ that would likely require a larger number of parameters to describe with other methods. From the theoretical point of view, a local feature in $w(z)$ is not particularly motivated, but can be produced in scalar field models of dark energy with a step-like bump in the potential, or in certain types of phantom models [116].

In the next section we will try to recover a feature in $w(z)$, a bump, that we "hide"

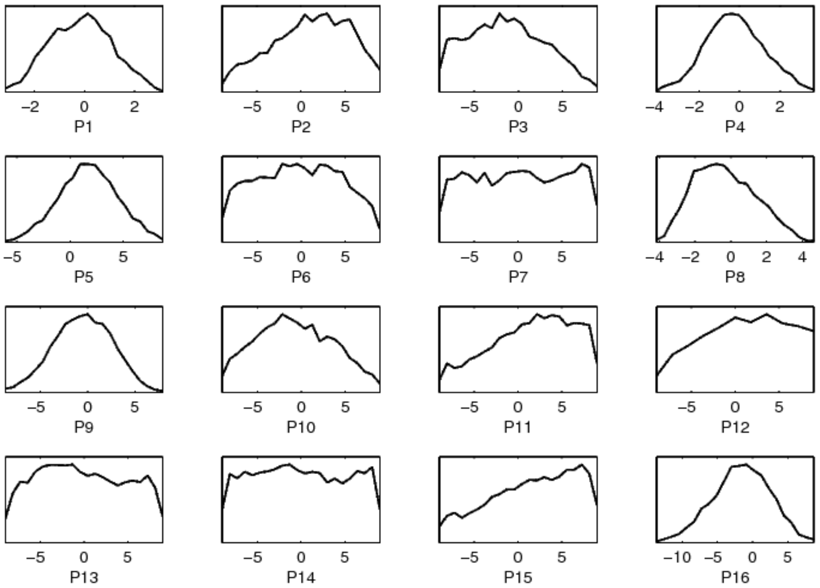

Figure 2.2: The 1-D posterior distributions of all the 16 wavelet coefficients obtained from our first MCMC run.From [115].

in a simulated future data. Such a bump is not ruled out by current data [132], since the averaged $w(z)$ – the quantity that the current data essentially constrains – does not significantly deviate from -1 for this feature. The main rationale for considering this particular choice is that such a bump feature cannot be easily discovered by binning if one does not know the size, the position and the scale of the bump in advance.

2.4.4 Detecting localized features in $w(z)$

In this section, we use the wavelet method to detect a feature hidden in the simulated mock future data. Our procedure can be summarized as follows:

1. Generate a mock dataset with a feature of $w(z)$ hidden in;
2. Perform the first MCMC fit for 16 wavelet coefficients;
3. Sort the wavelet coefficients according to their signal-to-noise ratio (SNR) and set all except the few with the highest SNR to zero;

Para.	Constraints	SNR	Para.	Constraints	SNR
P1	-0.1 ± 1.2	0.1	P9	-0.5 ± 3.0	0.2
P2	1.1 ± 4.4	0.3	P10	-0.7 ± 4.3	0.2
P3	-1.3 ± 4.3	0.3	P11	1.5 ± 4.6	0.3
P4	-0.2 ± 1.4	0.1	P12	7.4 ± 9.2	0.8
P5	1.7 ± 2.7	0.6	P13	-0.1 ± 5.0	0.0
P6	-0.3 ± 4.7	0.1	P14	0.1 ± 5.2	0.0
P7	0.2 ± 5.2	0.0	P15	1.6 ± 4.8	0.3
P8	-0.3 ± 1.7	0.2	P16	-1.6 ± 4.1	0.4

Table 2.2: Marginalized mean values with 68% CL. errors and SNR for all the 16 wavelet parameters. The high SNR parameters are underlined.

4. Perform the second MCMC with all possible combinations of “surviving” wavelet coefficients to find the model with the least χ^2 per degree of freedom (DoF)

5. Quantify the detection using $\Delta\chi^2/\Delta(\mathrm{DoF})$, ΔAIC and ΔBIC.

To start, we simulate future SNe Ia data for a DE model with a feature in $w(z)$ given by

$$w(z) = -1 + A\,\exp[-(z-z_0)^2/\sigma^2]\,, \tag{2.52}$$

where we choose $A = -0.9$, $z_0 = 0.6$, $\sigma = 0.1$. This $w(z)$ is shown with a black solid line in Fig. 2.5. We assume a flat universe, and choose the other cosmological parameters as $\Omega_b = 0.046$, $\Omega_m = 0.279$ and $H_0 = 70$ km/s/Mpc. We also apply the distance priors derived from the CMB and BAO data as described in Sec. 2.4.2. We assume the luminosity data binned into 17 redshift bins in the range of $z \in [0, 1.7]$. Fig. 2.3 shows the comparison of the residuals (defined with respect to the ΛCDM model) of the distance modulus for the model with a bump-like feature in $w(z)$ and a constant-w model which has the same average value w (i.e. one that gives the same distance to the CMB last scattering surface). Error-bars are plotted according to the characteristics of the SNe Ia survey considered here. The plot shows that future SNe Ia data is able to differentiate between these models around $z = 0.5$.

Having produced our mock datasets, we perform a MCMC fit for all the 16 wavelet parameters plus $\Omega_b h^2$, $\Omega_m h^2$ and h, assuming a flat universe and flat priors for all the wavelet parameters. Fig. 2.2 shows the marginalized 1-D likelihood distributions for the

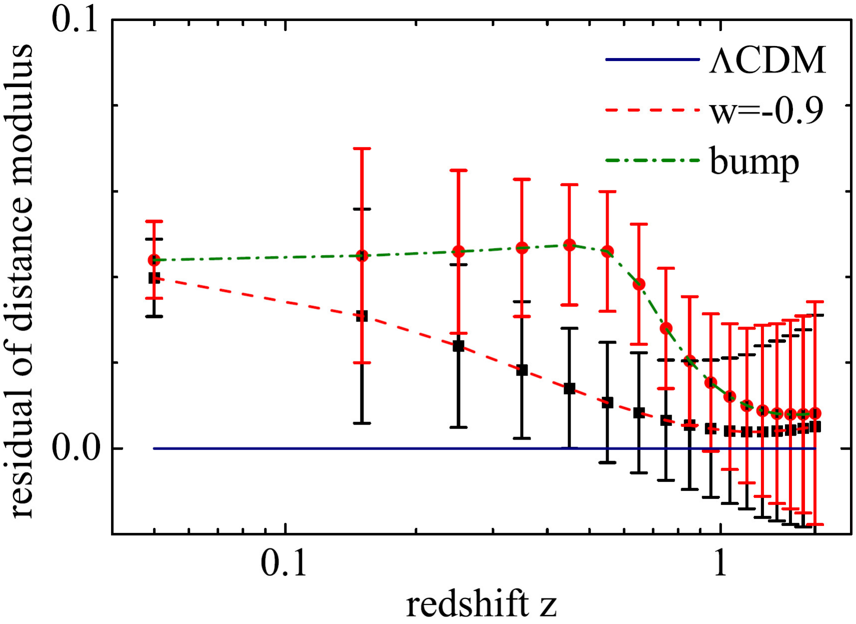

Figure 2.3: Comparison of the residuals of the distance modulus for ΛCDM, WCDM and bump models with characteristic error-bars for the futuristic SNe Ia survey considered here. From [115].

16 wavelet parameters, with Table 2.2 listing the corresponding mean values and the 68% CL error bars. As one can see, for many wavelet parameters the standard deviation is much larger than the mean value, indicating that they are not sensitive to the presence of a feature in w. Such poorly constrained parameters are thus redundant, so we keep only the ones with the highest SNR. In order for the D4 wavelets to be able to describe a constant w, one should keep P_1. In addition, we keep the 2-3 coefficients with the highest SNR. In our example, we keep parameters $P1$, $P5$ and $P12$.

Next, we redo the MCMC using every combination of the selected parameters (with $P1$ always included) and find the one that gives the minimum value of the reduced χ^2. In this case, the optimal combination is that of $P1$ and $P5$, while setting $P12 = 0$. Marginalized likelihood distributions for this model are shown in Fig. 2.4 and the plot of $w(z)$ reconstructed using this model is shown in the left panel of Fig. 2.5.

In the above example two wavelet parameters were measured to be non-zero. The correlation between the two wavelet parameters is negligible, which need not happen in

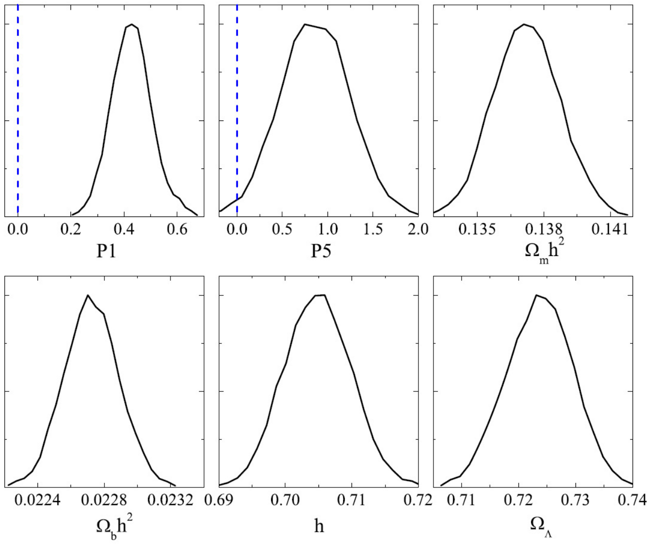

Figure 2.4: 1-D posterior distributions of the 1st and the 5th wavelet coefficients, and the other four cosmological parameters. From [115].

Model	$\Delta\chi^2/\Delta(\mathrm{DoF})$	ΔAIC	ΔBIC
WCDM($w=-0.9$)	0	0	0
CDM-D4-P1,5	-8.8	-6.3	-3.7
CDM-Haar-P2,4	-8.3	-6.8	-3.2

Table 2.3: The differences in the model selection criteria for the simulated data with a bump feature in $w(z)$.

general, but is somewhat expected. Namely, this combination is the one most favored by the reduced χ^2, which means that both parameters are likely needed to describe the data – one of them cannot compensate for the other. This implies a small correlation between these two parameters.

Detecting a departure from $w=-1$, which is all we have discussed so far, does not in itself amount to detecting the bump feature. The value of $w(z)$ in Fig. 2.5 averaged over redshift is larger than -1, so we would detect a departure from -1 by simply fitting a constant w. Hence, the more relevant question is not to what extent wavelets are able to detect a departure from -1, but to what extent the wavelet fit is preferred to a fit by a simpler model with one constant w parameter.

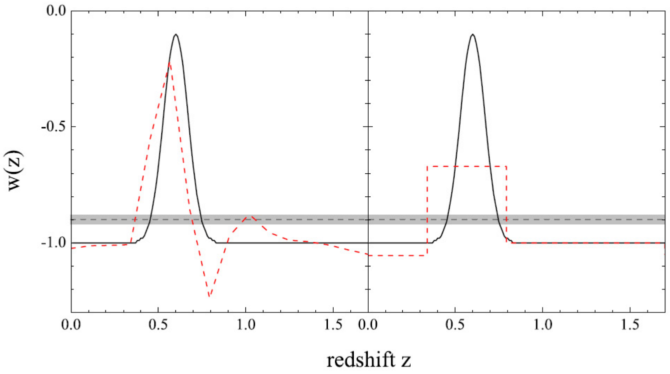

Figure 2.5: The hidden feature (black solid), and the reconstruction using D4 (red dashed, left panel) and Haar (red dashed, right panel) wavelets. The horizontal dashed line and the shaded band illustrate the fit with the constant w model and the 68%CL errors. From [115].

To answer this question, we fit the model with a constant w (wCDM) in a flat universe and apply the model selection criteria to determine the degree to which the wavelet model is preferred in comparison. In particular, we calculate the change in χ^2 per additional degree of freedom, the difference in the BIC and AIC. As one see from the numbers in Table 2.3, the wavelet fit is strongly preferred according to all three criteria.

In addition to using D4 wavelets, we have followed the same procedure and tried to recover the bump feature using the Haar wavelets. We find again that a model with two wavelet parameters is optimal and is preferred to wCDM at a similar significance level as in the D4 case. The plot of $w(z)$ reconstructed using two Haar wavelets is plotted in the right panel of Fig. 2.5.

As a test, we have repeated the same procedure using data simulated according to parameters of existing data sets. We confirmed that the bump feature cannot be detected today at any significance. We have also checked if we can accurately recover $w(z)$ if ΛCDM was the true model for the universe. In this case all the wavelet coefficients should be zero or the difference from zero should not be statistically significant. To test that, we consider simulated data for ΛCDM model and followed the same procedure of selecting the first few coefficients with the highest signal to noise, and then trying all different combinations of the these selected wavelets. Our MCMC results in this case show no evidence of detection of departure from zero for any of the wavelet coefficients, and ΛCDM is correctly

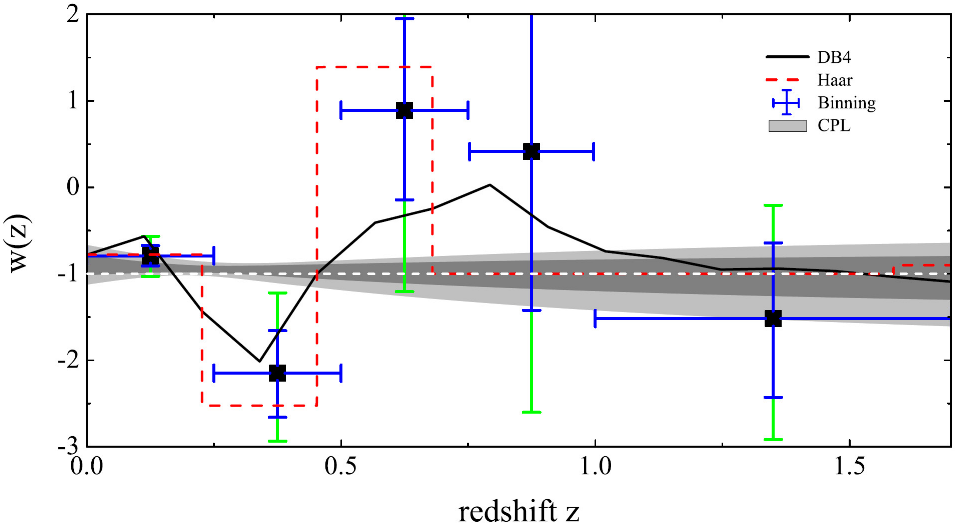

Figure 2.6: Reconstruction of $w(z)$ from current data using D4 (black solid line), Haar (red dashed line) wavelts, binning (error bars) and CPL parametrization (shaded regions). The inner blue error bars (inner shaded dark grey band) and outer green error bars (outer shaded light grey band) show the 68 and 95% CL. constraints respectively. From [115].

recovered as the best model.

2.4.5 Searching for features in current data

In this section, we apply our method to the current SNe Ia, CMB and BAO data to search for the deviation of $w(z)$ from -1. We use the "Constitution" SNe data sample with 397 data points [136], apply the distance priors measured by the WMAP5 team [125], and assume a flat universe.

Table 2.4 shows the main results. We find that using 16 D4 or Haar wavelet coefficients reduces the χ^2 and gives a hint that w may have deviations from ΛCDM. However, a model with 16 parameters is not preferred by any of the information criteria. With D4 wavelets, parameters $P1$, $P4$, and $P8$ give the optimal model with a $\Delta\chi^2/\Delta(\mathrm{DoF})$ of -1.6. With Haar wavelets, this number is -1.9 with the three wavelet parameters being $P2$, $P4$ and $P5$. We also find that none of the wavelet fits are favored by the AIC and BIC.

Plots of $w(z)$ reconstructed using the wavelet method with D4 and Haar are shown in Fig. 2.6. We also plot the results obtained using the binning method and the CPL parametrization [133, 134]

$$w^{CPL}(z) = w_0 + w_a \frac{z}{1+z}, \tag{2.53}$$

taken from [135]. As one can see, the best fit wavelet models show weak hints of dark energy dynamics. In particular, $w(z) < -1$ for $z <\in [0.25, 0.5)$ and $w > -1$ for $z \in [0.5, 1]$, implying that w crosses -1 during its evolution. This is consistent with the analysis of the "Constitution" data set in [135], which reported weak evidence for a similar evolution history. Regardless of whether such evolution is real or not, the CPL parametrization would not be able to see it.

As mentioned, a significant deviation from 0 for any of the wavelet parameters shows deviation from ΛCDM. Table 2.5 shows the eigenvalues of principal components for each model together with their errors, separately. There is a 1σ and 2σ detection from D4 and Haar respectively, which can be interpreted as weak hints that w may have a departure from -1.

We note that although Ref. [135] obtained similar results, they used a 5 w bin model. They found this optimal 5-bin model after performing a model-selection on 10 different binning models, which is computationally expensive. With the wavelet approach, we recover the same feature in $w(z)$ with only 3 wavelet parameters after running MCMC just a few times. This is possible because of the multi-resolution nature of the wavelets.

Model	$\Delta\chi^2/\Delta$(DoF)	ΔAIC	ΔBIC
ΛCDM	0	0	0
CDM-D4-16Ps	-0.3	32.7	91
CDM-Haar-16Ps	-0.4	31.1	89
CDM-D4-1,4,8	-1.6	0.9	13
CDM-Haar-2,4,5	-1.9	0.2	12.3

Table 2.4: Differences in the model selection criteria for the analysis of the current data.

Model	PC1	PC2	PC3
D4-1,4,8	0.25±1.04	0.36±0.39	0.07±0.13
Haar-2,4,5	-4.03±1.81	-0.26±0.46	0.10±0.15

Table 2.5: Principal Components for wavelet coefficients of optimum w models with current cosmological data

2.5 Summary

We investigated the utility of the wavelet expansion method for recovering a local redshift-dependence in the dark energy equation of state $w(z)$ with cosmological distance data. The advantage of wavelets over other methods is that there is no need to assume a scale or a position for a feature in $w(z)$. With wavelets, one is able to search for small scale features, while looking at the large scale picture at the same time. Our results show that a bump-like feature in $w(z)$, which is not ruled out by today's data, can be recovered using wavelets at a high significance with future data.

We have tried relaxing the flatness assumption and considered curvature as an additional parameter. In this case, we found that the bump feature we put in becomes undetectable, even with the wavelet technique, due to the degeneracy between w and the curvature Ω_K. There is sufficient freedom for Ω_K and Ω_m to adjust themselves to mimic the effect of a featured $w(z)$ in the luminosity distance observations. More specifically, we find that a model with $w = -1.2$, $\Omega_m h^2 = 0.137$, $\Omega_b h^2 = 0.0227$, $\Omega_\Lambda = 0.6$, $\Omega_K = 0.1$ and $h = 0.68$ has nearly the same goodness-of-fit as the bump model.

Applying the wavelet method to current cosmological data we find a hint of departure from ΛCDM at a 2σ level. The same behavior has been found independently using the binning method [135] at the same significance level. We have shown that such local features can be found more efficiently by using wavelets. The feature we found in current data will require further investigation as the SNe Ia and other cosmological data improves.

Chapter 3

Modified gravity

An alternative approach to DE for describing the observed cosmic acceleration is to modify the underlying theory of gravity, i.e. GR. In the previous chapter, the assumption was that GR was correct, but that the universe contained a DE component that drove the cosmic acceleration. In other words, the right-hand side of Einstein's equation was modified by adding a new component to $T_{\mu\nu}$, while the left-hand side, ($G_{\mu\nu}$), remained unaltered.

Here the idea is that we might need to alter GR, i.e., modify the left-hand side of Einstein's equation. Different approaches have been taken to modify GR in a way that is both consistent with fundamental laws of physics and can produce the desired cosmic acceleration on the cosmological times and scales. We start this chapter by a brief review of different attempts to provide such an alternative gravity theory.

3.1 Alternative gravity theories

3.1.1 Scalar-tensor theories

Scalar-tensor theories are the most studied class of alternative gravity (modified gravity) theories. Their observational consequences are explored in detail, for example, in [137]. They can be viewed as the low-energy limit of more fundamental theories such as string theory .

The general action for scalar-tensor theories is [138]

$$S = \int d^4x\sqrt{-g}\left[b(\lambda)R - \frac{1}{2}h(\lambda)g^{\mu\nu}(\partial_\mu\lambda)(\partial_\nu\lambda) - U(\lambda) + \mathcal{L}_M(g_{\mu\nu},\psi_i)\right], \tag{3.1}$$

where $\lambda(\vec{x},t)$ is a scalar field, $b(\lambda)$ is a non-minimal coupling of the field λ to gravity $U(\lambda)$ represents the potential of the scalar field and $\mathcal{L}(g_{\mu\nu},\psi_i)$ is the matter Lagrangian as before. The equations of motion are derived from variation of the action with respect to the metric (the analogue of Einstein's equation) [69]

$$G_{\mu\nu} = b^{-1}(\lambda)\left[\frac{1}{2}T^{(M)}_{\mu\nu} + \frac{1}{2}T^{(\lambda)}_{\mu\nu} + \nabla_\mu\nabla_\nu b - g_{\mu\nu}\Box b\right], \tag{3.2}$$

with the scalar field's energy-momentum tensor defined as

$$T^{(\lambda)}_{\mu\nu} = h(\lambda)(\nabla_\mu\lambda)(\nabla_\nu\lambda) - g_{\mu\nu}\left[\frac{1}{2}h(\lambda)g^{\rho\sigma}(\nabla_\rho\lambda)(\nabla_\sigma\lambda) + U(\lambda)\right]. \tag{3.3}$$

The equation of motion for the scalar field is

$$h\Box\lambda + \frac{1}{2}h'g^{\mu\nu}(\nabla_\mu\lambda)(\nabla_\nu\lambda) - U' + b'R = 0, \tag{3.4}$$

with the prime denoting a derivative with respect to λ.

For a FRW universe these equations imply a modified Friedmann equation for the scale factor

$$H^2 \equiv \left(\frac{\dot{a}}{a}\right)^2 = \frac{\rho}{6b} + \frac{h\dot{\lambda}^2}{6b} - H\frac{\dot{b}}{b} + \frac{U}{6b}, \tag{3.5}$$

and an equation of motion for the scalar-field

$$\ddot{\lambda} + 3H\dot{\lambda} = 3\frac{b'}{h}\left(\dot{H} + 2H^2\right) - \frac{h'\dot{\lambda}^2}{2h} - \frac{1}{2}\frac{U'}{h}. \tag{3.6}$$

A scalar-tensor model is defined by the form of $b(\lambda)$, $h(\lambda)$ and $U(\lambda)$. But, to determine the phenomenology, the initial conditions for the above equations should also be specified.

An example: Brans-Dicke theory

This is an example of a scalar-tensor theory with $b(\lambda) = \lambda/(16\pi G)$, $h(\lambda) = \omega/(8\pi\lambda G)$, and $U(\lambda) = 0$, where the Brans-Dicke parameter ω is a constant [140]. This theory has been studied in detail and its solutions are explored.

In the solar system, deviations of the solution of a modified gravity theory from that of the GR are parametrized by a *parameterized-post-Newtonian* (PPN) parameter, $\gamma_{\rm PPN}$, defined as

$$g_{ij} = (1+2\,\gamma_{\rm PPN} V)\delta_{ij} + O(V^2)\,, \tag{3.7}$$

where V is the Newtonian potential. For the Brans-Dicke theory, $\gamma_{\rm PPN}$ is calculated to be

$$\gamma_{\rm PPN} = (\omega+1)/(\omega+2)\,. \tag{3.8}$$

Measurements of $\gamma_{\rm PPN}$ parameter from time-delay experiments in the Solar System give [141]

$$\gamma_{\rm PPN} = 1 + (2.1 \pm 2.3) \times 10^{-5}\,, \tag{3.9}$$

which translates to a bound on the Brans-Dicke parameter: $\omega \gtrsim 5 \times 10^4$.

3.1.2 $f(R)$ theory

This class of modified gravity theories has received special attention. For the case of $f(R)$, the Einstein-Hilbert action is modified as [142]

$$S = \frac{1}{16\pi G}\int d^4x\sqrt{-g}\,[R + f(R)] + + \int d^4x\sqrt{-g}\,\mathcal{L}_{\rm m}[\Psi_i, g_{\mu\nu}]\,, \tag{3.10}$$

and the field equations are

$$(1+f_R)\,R_{\mu\nu} - \frac{1}{2}g_{\mu\nu}\,(R+f) + \left(g_{\mu\nu}\Box - \nabla_\mu\nabla_\nu\right) f_R = 8\pi G T_{\mu\nu}\,, \tag{3.11}$$

where $f_R \equiv df/dR$. For FRW universe, the Friedmann and acceleration equations are modified as

$$\begin{aligned} H^2 + \frac{f}{6} + H\dot{f}_R &= \frac{8\pi G}{3}\rho\,, \qquad (3.12) \\ \frac{\ddot{a}}{a} - H^2 f_R + a^2\frac{f}{6} + \frac{3}{2}H\dot{f}_R + \frac{1}{2}\ddot{f}_R &= -\frac{8\pi G}{6}(\rho + 3P)\,. \qquad (3.13) \end{aligned}$$

Here, instead of a DE component on the R.H.S. of Eq. (3.13), the extra terms on the L.H.S. are responsible for producing the acceleration, while the universe is filled only with ordinary matter components.

An example: $1/R$ theory

In this theory $f(R) \equiv -\mu^4/R$, where μ is a constant [143]. This example illustrates how the difference between $f(R)$ and GR predictions can arise in the experimental observations. The field equation are

$$8\pi G T_{\mu\nu} = \left(1 + \frac{\mu^4}{R^2}\right) R_{\mu\nu} - \frac{1}{2}\left(1 - \frac{\mu^4}{R^2}\right) R g_{\mu\nu} + \mu^4 \left(g_{\mu\nu}\Box - \nabla_{(\mu}\nabla_{\nu)}\right) R^{-2}. \tag{3.14}$$

In the solar system, the pressureless matter is the dominant component with $T \equiv g^{\mu\nu}T_{\mu\nu} = -\rho$ where ρ is the mass density in the solar system. The trace of the Eq. (3.14) gives

$$\Box\frac{\mu^4}{R^2} - \frac{R}{3} + \frac{\mu^4}{R} = \frac{8\pi G T}{3}, \tag{3.15}$$

which should be compared with the trace of Einstein's equation

$$R = 8\pi G\rho\,. \tag{3.16}$$

Due to the quadratic nature of Eq. (3.15), there are two solutions. Considering that $\mu^2 \sim H \ll G\rho$ in the solar system [69], there is a solution similar to GR solution

$$R \simeq 8\pi G\rho\,, \tag{3.17}$$

which is shown to be unstable for small-wavelength perturbations [144]. But the second solution,

$$R^2 \simeq \mu^2 , \tag{3.18}$$

is stable but predicts a PPN parameter $\gamma_{PPN} = 1/2$, which disagrees with experimental constraints [145, 146].

There are a set of common conditions applicable to viable $f(R)$ models:

- $f_{RR} > 0$: which guarantees that the dynamical behavior is stable in the high-curvature regime [147].
- $1 + f_R > 0$ for all R: in theories such as $f(R)$ the effective value of Newton's constant measured in the terrestrial experiments, $G_{eff} = G/(1 + f_R)$, is not necessarily equal to G. This condition guarantees a positive G_{eff}.
- $f_R < 0$: so that GR is recovered in the early universe.

Choice of frame and equivalence between $f(R)$ and scalar-tensor theories

Since the original Brans and Dickie work [140], it was known that scalar-tensor theories can be expressed in two frames: the *Jordan frame*, and the *Einstein frame*, which are related to each other by a conformal transformation of the metric:

$$\tilde{g}_{\mu\nu} = (1 + f_R) g_{\mu\nu} , \tag{3.19}$$

where $\tilde{g}_{\mu\nu}$ and $g_{\mu\nu}$ are the metric in the Einstein and Jordan frame, respectively. This local redefinition of the metric amounts to a choice of a ruler, or units in which one measures distances and all other dimensionful quantities. Essentially, in one frame the rulers are not changing, while distances depend on the extra degree of freedom. In the other frame, distances are kept unchanged, while rulers vary.

The action (3.10) is expressed in the Jordan frame, where matter fields are minimally coupled to gravity. Using Eq. (3.19), it can be written in the Einstein frame as

$$\begin{aligned} S &= \frac{1}{16\pi G} \int d^4x \sqrt{-\tilde{g}}\, \tilde{R} + \int d^4x \sqrt{-\tilde{g}} \left[-\frac{1}{2} \tilde{g}^{\mu\nu} (\tilde{\nabla}_\mu \phi) \tilde{\nabla}_\nu \phi - V(\phi) \right] , \\ &+ \int d^4x \sqrt{-\tilde{g}}\, e^{-2\beta\phi/M_p} \mathcal{L}_{\rm m}[\Psi_i, e^{-\beta\phi/M_p} \tilde{g}_{\mu\nu}] , \end{aligned} \tag{3.20}$$

where $\beta\phi \equiv \ln(1+f_R)/\sqrt{8\pi G}$, with $\beta \equiv \sqrt{2/3}$, and the potential $V(\phi)$, determined entirely from the original form of the action, is given by

$$V(\phi) = \frac{1}{16\pi G}\frac{Rf_R - f}{(1+f_R)^2}\,. \tag{3.21}$$

Eqs. (3.10) and (3.20) are dynamically equivalent and should lead to the same physical predictions. Action in the Einstein frame has a simpler form but, instead, there is a non-minimal coupling between matter fields and the Einstein metric. In addition, now there is an explicit scalar DoF ϕ appearing in the action. In this frame, the equations of motion for the scalar field and matter fluid are

$$\ddot{\phi} + 3\tilde{H}\dot{\phi} + V_{,\phi} = 4\pi G\beta(\tilde{\rho} - 3\tilde{P})\,, \tag{3.22}$$

$$\dot{\tilde{\rho}} + 3\tilde{H}(\tilde{\rho} + \tilde{P}) = -4\pi G\beta(\tilde{\rho} - 3\tilde{P})\,, \tag{3.23}$$

where $\tilde{\rho} \equiv e^{-16\pi G\beta\phi}\rho$ and $\tilde{P} \equiv e^{-16\pi G\beta\phi}P$ are the Einstein frame energy density and pressure. As a consequence, the matter energy-momentum tensor is not covariantly conserved, and particle physics parameters such as masses of particles and dimensionful coupling constants are space-time dependent. That is why some physicist prefer to work in the Jordan frame. In this frame, all the quantities relevant to the particle physics are easily calculated, since the energy-momentum conservation holds.

Working in the Einstein frame can be easier when gravitational equations are concerned. The modified Friedmann and acceleration equations are

$$\tilde{H}^2 = \frac{8\pi G}{3}\left[\tilde{\rho}(\phi) + \frac{1}{2}\dot{\phi}^2 + V(\phi)\right], \tag{3.24}$$

$$\frac{\ddot{\tilde{a}}}{\tilde{a}} = -\frac{4\pi G}{3}\left[\tilde{\rho}(\phi) + 3\tilde{P}(\phi) + 2\dot{\tilde{\phi}}^2 - 2V(\phi)\right]. \tag{3.25}$$

Thus, it is convenient to use the Einstein frame to solve the field equations, and then translate the results into the Jordan frame to compare with observations [150, 151].

3.1.3 Theories with extra dimensions

Another class of alternative-gravity theories is inspired by the idea of changing the dimensionality of space. One of the most widely studied models assumes that we are living on a 3-D brain which itself resides in a higher dimensional "bulk". Matter and all non-gravitational forces are confined to "live" on the brane while gravity is not confined to 4-D spacetime and can "leak" into the extra dimensions. An example of such a braneworld scenario has been constructed by Dvali, Gabadadze and Porratti (the *DGP* model [153]). We briefly describe the cosmological implications of this model, as outlined in [154].

The DGP model

In this model, the bulk is a 5-D flat, Minkowski space-time with infinite volume. The 5-D action of the model is

$$S = \int d^5x \, \sqrt{-g_5} \frac{3R_5}{16\pi G_5} + \int d^4x \sqrt{-g_4} \, \frac{R_4}{16\pi G_4} \left[R_4 + \mathcal{L}_m\right] , \tag{3.26}$$

where X_n represent the quantity X in n dimensions.

The cosmic acceleration on the brane is due to an effective theory of gravity. There is a transition scale r_c:

$$r_c = \frac{G_5}{2 \, G_4} , \tag{3.27}$$

such that on smaller distances from a point source, $r < r_c$, we have a normal 4-D gravity with $V(r) \propto 1/r$, while on large scales the gravity is weakened, with $V(r) \propto 1/r^2$. This is due to interaction of gravitons with the fifth dimension that has a non-negligible contribution on large scales. What makes DGP model distinct from other extra dimensional models is the size of the extra dimension. In DGP, the extra dimension is large. As a result, there is an energy cost for the gravitons with small wavelengths ($\lesssim r_c$) to propagate into the bulk and, therefore, they are confined to the brane.

The Friedmann equation on the brane is

$$H^2 + \frac{K}{a^2} - \varepsilon \frac{1}{r_c} \sqrt{H^2 + \frac{K}{a^2}} = \frac{8\pi G}{3} \rho \, . \tag{3.28}$$

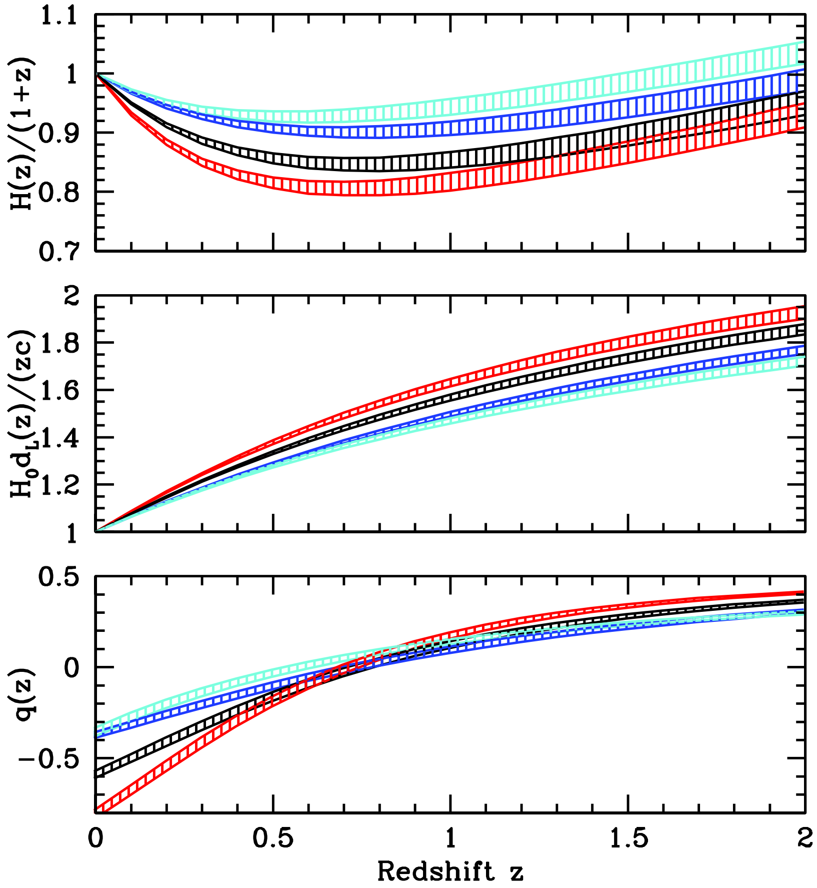

Figure 3.1: $H(z)$, luminosity distance $d_L(z)$, and deceleration $q(z) \equiv -\ddot{a}/(a\,H^2)$ are shown for ΛCDM (black), DGP (cyan) and $w_{DE} = -1.2$ (red) and $w_{DE} = -0.8$ (blue) models with thickness of the curves indicating the uncertainties in Ω_m. From [69]; Used with permission.

This quadratic equation has two solutions: $\varepsilon = +1$ gives the self accelerating solution which happens when $H^{-1} \gtrsim r_c$. With $\varepsilon = -1$, one needs a CC component to generate the acceleration. It has been shown that the expansion history, given by the $\varepsilon = +1$ branch, does not fit the observational constraints [155, 156]. Fig. 3.1 compares some of the background expansion parameters for ΛCDM, DGP and two different wCDM models. With accurate measurements of expansion history, one can discriminate between these models.

3.1.4 Other approaches

Degravitation theory

In this approach, the Einstein equation is modified as [157, 158]

$$\left[1+F(L^2\Box)\right] G_{\mu\nu} = 8\pi G T_{\mu\nu}\,, \tag{3.29}$$

where $F(x) \gg 1$ for $x \to 0$ and $F(x) \to 0$ for $x \to \infty$. $L \sim H_0^{-1}$ is a characteristic scale beyond which gravity weakens.

Theories with modified dynamics

Generalizations of the DGP model can provide new ranges of dynamics for the 3-D brane in the bulk, resulting in a modified Friedmann equation of the form [161, 162]

$$H^2 \propto \rho^n\,. \tag{3.30}$$

The general trend in these theories is that w_{eff} asymptotes to a CC value at late times leading to the desired acceleration. However, the range of n is constrained by observations.

Palatini formalism

In this formalism, instead of metric $g_{\mu\nu}$, the equations of motion (Einstein equations) are derived from variation of the metric action with respect to both the connection $\Gamma^{\rho}_{\mu\nu}$ and the metric.

With the Einstein-Hilbert action, both approaches yield the same equations. However, for a more general action, the Palatini formalism gives rise to a different theory. It is shown that solutions containing accelerated expansion can be obtained [159] without violating the solar system constraints. Such approach is not flawless and for example, produces matter couplings that leads to violations of the equivalence principle [160].

Back reaction of cosmological perturbations

In this approach, the idea is that rather than new form of DE, or a modification of gravity, the observed acceleration of the universe is due to the back reaction of either super or sub-horizon cosmological perturbations [163, 165, 166, 167, 168].

This idea originates from investigations of the quantum gravitational back-reaction on an initially inflating, homogeneous and isotropic universe [169, 170, 171, 172]. It was shown that the long wavelength gravitational waves back-react on an inflationary background and change the rate of inflation. However it was shown that such back-reactions do not lead to a plausible acceleration in the framework of GR, unless there is already a DE component present in the universe [173, 174]. Recently, it was demonstrated that the scalar field DE can be emerging from the *kinematical* back-reaction effects. Hence, the quintessence scenario could be physically originated from inhomogeneities in the universe [175]. Such idea would allow a universe with conventional gravity and no DE component, but has not been successful.

3.2 Phenomenological approaches to modified gravity

As we saw in the previous section, there is a large number of alternative gravity proposals to explain the observed acceleration of the universe. One should add to this a list of the DE theories from the previous chapter and also the new theories that might be introduced in the future. These theories will be confronted with cosmological data, which can be a very time-consuming task. To be tested with the large-scale structure data, perturbation equations for each of these theories need to be calculated and solved numerically. Finally, the observable quantities need to be calculated and then compared to data.

In 1970s, a similar situation existed for experimental tests of GR. At the time, the Parameterised Post-Newtonian (PPN) method was invented to test alternative theories of gravity that needed to be confronted with the constraints from solar system experiments. With PPN, a set of generic parameters are calculated for each theory and then compared with the observational constraints [176]. A similar approach has been taken for the case of alternative gravity/DE theories. The goal here is to come up with a general parametrization of cosmological perturbation equations such that it covers all the alternative theories discussed before.

These parameters can be classified into two types, the *trigger* parameters and the *model* parameters [177]. Trigger parameters [37, 178, 179, 181], are directly measured from observations with no need to evolve perturbation equations. Such parameters are useful for detecting a breakdown of a theory, based on the prediction of the theory for the parameter value. However, one can not calculate observables from trigger parameters. The model parameters [38, 39, 182, 41, 46] have physical meanings and, in some cases, unique values in a theory. The theoretical predictions of the theory, based on these parameters, can then be compared to observations. We will work with both types of parameters in the following chapters.

3.2.1 Parametrization of the field equations

As discussed in 1.2.2, there are two DoF in the linear scalar perturbations of the metric. The role of the gravity theory is to provide two equations which relates the two metric potential scalar DoF to each other and to the perturbations in the content of the universe. In GR, this is done by the Poisson and anisotropy equations

$$k^2\Phi = -4\pi G a^2 \sum_i \rho_i \Delta_i \,, \tag{3.31}$$

$$k^2(\Phi - \Psi) = 12\pi G a^2 \sum_i (\rho_i + P_i)\sigma_i \,, \tag{3.32}$$

where $\rho\Delta = \rho\delta + 3\frac{aH}{k}(\rho + P)$ is the comoving density perturbation, σ is the anisotropic stress defined as $(\rho + P)\sigma \equiv -(\hat{k}^i\hat{k}_j - \frac{1}{3}\delta^i_j)\pi^i_j$ and the sum is over all the species present in the universe.

Working in the framework of parametrized modified gravity, one can then use two functions to parametrize a set of general field equations analogous to the Poisson and anisotropy equations in GR. In the conformal Newtonian gauge and for late times, when radiation energy density in the universe is negligible, such parametrized equations can be written as

$$k^2\psi \equiv -4\pi a^2 G\mu(a,k)\rho\Delta \,, \tag{3.33}$$

$$\frac{\phi}{\psi} \equiv \gamma(a,k) \,, \tag{3.34}$$

where $\rho\Delta$ is dominated by the cold dark matter. The product μG is sometimes interpreted as the effective Newton constant, $G_{\mathrm{eff}} \equiv \mu G$ and γ as the *gravitational slip*. $\mu(a,k)$ and $\gamma(a,k)$ are generic functions of time and scale that parametrize *solutions* in alternative gravity theories and depend on the choice of the initial conditions. In some theories, one can calculate their approximate form analytically in the quasi-static approximation. For instance, perturbation equations have been derived for some classes of scalar-tensor theories in [41, 45, 183, 184, 185, 186, 187, 188], and for the DGP theory and its higher-dimensional extensions in [153, 189, 190, 191, 192, 193]. for some of these theories [193].

At late times, the growth of matter on sub-horizon scales is governed by the potential ψ, not ϕ. To see this, one can combine Eqs. (1.49) and (1.50) in the limit of $k/(aH) \to \infty$ to get

$$\ddot{\delta} + \mathcal{H}\dot{\delta} + k^2\psi = 0\,, \tag{3.35}$$

where time derivative is w.r.t. conformal time. Hence, having a parametrized Poisson-like equation in terms of ψ is more directly relevant to observations.

At linear order, on needs to evolve four quantities, the two gravitational potentials ϕ and ψ, and Δ and v. Hence, four evolution equations are needed. Eqs. (3.33) amd (3.34) provide two while the other two come from conservations of energy-momentum, Eqs. (1.49) and (1.50). Defining the new dimensionless variables [177]:

$$p \equiv \frac{k}{aH} \quad u \equiv pv \quad E_m = \frac{\Omega_M}{a^3} \quad E = \frac{H^2}{H_0^2}\,, \tag{3.36}$$

we can combine Eqs. (3.33,3.34,1.49,1.50), and arrive at the following evolution equations

$$\begin{aligned} \Delta' &= \frac{-\frac{9E_m}{2E}\gamma\mu\left[\frac{1-\gamma}{\gamma} + \frac{(\gamma\mu)'}{\gamma\mu}\right]\Delta + \left[3\frac{H'}{H} - p^2\right]u}{p^2 + \frac{9E_m}{2E}\gamma\mu} && (3.37) \\ u' &= -\left[2 + \frac{H'}{H}\right]u - \frac{3}{2}\frac{E_m}{E}\mu\Delta\,, && (3.38) \end{aligned}$$

where prime denotes a derivative w.r.t. $\log a$. Once μ and γ are specified, Δ and u can be calculated from the above equations. One can also combine Eqs. (3.37) and (3.38) into one second-order equation. For ΛCDM model, where by definition $\mu = \gamma = 1$, it becomes [177]

$$\Delta'' + \left[2 + \frac{H'}{H}\right]\Delta' - \frac{3}{2}\frac{E_m}{E}\Delta = 0 \tag{3.39}$$

which is the usual scale-independent GR equation.

Super-horizon evolution

It has been shown [15] that the evolution of perturbation on very large scales can be determined from the evolution of the background equations. Consider a background with scale factor $a(\tau,\kappa)$ where κ is the spatial curvature of a hypersurface of constant τ:

$$ds^2 = a^2\left[-d\tau^2 + d\chi^2 + \frac{1}{\kappa}\sinh^2_\kappa(\sqrt{\kappa}\chi)d\Omega\right] \tag{3.40}$$

where $\sinh_\kappa(x)$ is equal to $\sin(x)$ for $\kappa > 0$, equal to x for $\kappa = 0$, or equal to $\sinh(x)$ for $\kappa < 0$. If we perturb this space-time by

$$\kappa \to \kappa(1+\delta_\kappa)\,, \tag{3.41}$$

we can compensate for it by a change in the coordinates

$$\begin{aligned} \tau &\to \tau + \alpha\,, \\ \chi &\to \chi(1 - \frac{1}{2}\delta_\kappa)\,. \end{aligned} \tag{3.42}$$

Here δ_κ is a constant, while $\alpha = \alpha(\tau)$ [180]. This new geometry can be re-written in the form of a perturbed FRW metric:

$$ds^2 = a^2\left\{-(1+2\psi)d\tau^2 + (1-2\phi)\left[d\chi^2 + \frac{1}{\kappa}\sinh^2_\kappa(\sqrt{\kappa}\chi)d\Omega\right]\right\}, \tag{3.43}$$

where κ is the background curvature and

$$\psi(\tau) = \frac{\partial \ln a}{\partial \ln \kappa}\delta_\kappa + \alpha' + \mathcal{H}\alpha, \tag{3.44}$$

$$\phi(\tau) = \left(\frac{1}{2} - \frac{\partial \ln a}{\partial \ln \kappa}\right)\delta_\kappa - \mathcal{H}\alpha. \tag{3.45}$$

One can now eliminate α to find a generic evolution equation that relates δ_κ with ϕ and ψ *without* specifying any particular theory of gravity [180]:

$$\frac{1}{a^2}\frac{d}{d\tau}\left(\frac{a^2\phi}{\mathcal{H}}\right) = \phi - \psi + \left[\frac{1}{2a}\frac{d}{d\tau}\left(\frac{a}{\mathcal{H}}\right) - \frac{\partial \ln \mathcal{H}}{\partial \ln \kappa}\right]\delta_\kappa, \tag{3.46}$$

A number of assumption have been made in deriving Eq. (3.46): entropy perturbations have been neglected (perturbations are adiabatic); shear perturbations are negligible on large scales; local energy-momentum is conserved; and spatial gradients can be discarded. In terms of variables (3.36), this *super-horizon consistency condition* translates into

$$\zeta' \equiv (\delta - 3\phi)' = O(p^2) \;, \tag{3.47}$$

where ζ is the curvature perturbation on hypersurfaces of uniform density [194]. The conservation of ζ on super-horizon scales gives the following second order differential equation for the metric potentials [15, 177, 195]

$$\begin{aligned} &\psi'' + \left(2\frac{\gamma'}{\gamma} - \frac{H''}{H'} + \frac{1}{\gamma}\right)\psi' \\ &+ \left[\frac{\gamma''}{\gamma} - \frac{H''}{H'}\frac{\gamma'}{\gamma} + \left(\frac{H'}{H} - \frac{H''}{H'}\right)\frac{1}{\gamma}\right]\psi = O\left(\frac{p^2}{\mu\gamma}\right) \;. \end{aligned} \tag{3.48}$$

One sees that the evolution of perturbations outside the horizon is independent of μ up to linear order and any effect due to μ is completely hidden by cosmic variance [177]. Once H and γ are specified, Eq. (3.48) can be integrated to solve for the perturbation variables on super-horizon scales.

Sub-horizon evolution

From Eqs. (3.37) and (3.38), the second-order differential equation for sub-horizon scales, $k >> aH$, is [177]

$$\Delta'' + \left[2 + \frac{H'}{H}\right]\Delta' - \frac{3}{2}\frac{E_m}{E}\mu\Delta = 0 \;, \tag{3.49}$$

which is a μ-dependent equation, leading to a $G_{eff} \neq G$, but is γ-independent. Hence, on sub-horizon scales, the primary effect on the growth of structure is through μ. The time evolution of the matter density contrast can then be a sensitive probe of the underlying dynamics.

The evolution of Δ_m with time can be quantified by the *growth function*, f, defined as

$$f \equiv \frac{d}{d\ln a}\left(\ln\frac{\Delta(k,a)}{\Delta(k,a_i)}\right) \approx \Omega_m(a)^{\gamma_L}\,. \tag{3.50}$$

where γ_L [1] is a trigger parameter parametrizing the growth function [178, 179]. In a flat, matter dominated universe we have that δ_m evolves as $\delta_m \propto a$ and thus, we can parametrize deviations from this behavior in terms of γ_L via the growth function.

For the ΛCDM model, $\gamma_L \approx 6/11$ to a very good approximation, although this can change with Ω_M. For the case of GR with a DE component [180]

$$\gamma_L = \gamma_0 + \gamma_1\Omega_{DE} + O(\Omega_{DE}^2)\,, \tag{3.51}$$

where γ_0 and γ_1 are given by

$$\begin{aligned} \gamma_0 &= \frac{3(1-w)}{5-6w}, \\ \gamma_1 &= \frac{\gamma_0}{2w}\left[\frac{6w^2-7w+2}{5-12w} - \frac{2-3w}{3}\gamma_0\right]. \end{aligned} \tag{3.52}$$

In the case of $w=-1$, these expressions reduce to

$$\gamma_L = \frac{6}{11} + \frac{15}{2057}\Omega_{DE} + \dots\;. \tag{3.53}$$

Our goal, however, is to work in a parametrized framework and account for modified gravity in a model-independent manner. Using Eq. (3.49) and (3.50), it was shown that μ can be expressed in terms of γ_L [177] as

$$\mu = \frac{2}{3}\Omega_m^{\gamma_L-1}\left[\Omega_m^{\gamma_L} + 2 + \frac{H'}{H} + \gamma_L\frac{\Omega_m'}{\Omega_m} + \gamma_L'\ln\left(\Omega_m\right)\right]\,, \tag{3.54}$$

where prime is derivative w.r.t. $\log a$. In a flat ΛCDM background, Eq. (3.54) simplifies to

$$\mu = \frac{2}{3}\Omega_m^{\gamma_L-1}\left[\Omega_m^{\gamma_L} + 2 - 3\gamma_L + 3\left(\gamma_L - \tfrac{1}{2}\right)\Omega_m + \gamma_L'\ln\left(\Omega_m\right)\right]\,. \tag{3.55}$$

---

[1] A subscript L is introduced here to avoid confusion with our parametrization function γ defined in Eq. (3.34).

For a given γ_L, and with an additional specification of γ, one can use (3.54) in Eqs. (1.49), (1.50) and (3.33) to find consistent solutions for the linear perturbations.

3.2.2 Other parametrizations and their connection to (μ,γ)

In the parametrization method described above, it was made clear that in addition to the equations of the energy-momentum conservation, we need to define two equations relating the metric potentials to each other and to the energy-momentum perturbations. Within those two equations, we introduce two parametrizing functions that are responsible for capturing any deviations from the evolution predicted by our fiducial model, e.g. the ΛCDM model. However, the choice of the two equations that define such two functions is not unique. Different parametrizations have certain advantages and disadvantages, as we will see later. Our choice of these functions, the (μ,γ) parametrization in Eqs. (3.33) and (3.34), has the advantage that on super-horizon scales only γ affects the perturbations, while μ naturally becomes irrelevant. On the other hand, on sub-horizon scales, only μ affects the growth of matter over-densities and γ is irrelevant. This is due to the fact that evolution of perturbations on super-horizon scales is not necessarily related to their sub-horizon dynamics.

In the Parameterized Post-Friedmann (PPF) Framework of [182], this fact has been made explicit. In PPF, the parametrization is defined as

$$\begin{aligned} g &\equiv \frac{1-\gamma}{1+\gamma}, \\ f_G &\equiv -\left[1+8\pi G\,\frac{a^2\rho\Delta}{k^2(\phi+\psi)}\right]. \end{aligned} \tag{3.56}$$

On super-horizon scales, only g is relevant while on sub-horizon scales one needs g and f_G. In addition, a transition scale between the two regimes needs to be specified. The advantage of the PPF is that no assumption on g and f_G is needed in order to satisfy the consistency conditions, Eq. (3.47), while for the (μ,γ) parametrization, the condition $p^2/(\mu\eta) \to 0$ must be obeyed for small p to satisfy the super-horizon consistency condition [177]. This is a very mild assumption, likely to be satisfied in any reasonable modified gravity theory.

Another useful parametrization function is

$$\Sigma(a,k) \equiv -\frac{k^2 M_P^2 (\phi+\psi)}{\rho a^2 \Delta} = \frac{(1+\gamma)}{2}\mu \,. \tag{3.57}$$

$\Sigma(k,a)$ is directly related to the WL potential $\phi+\psi$ and, therefore, WL data is a direct probe of Σ. ISW power spectrum, Eq. (1.78), is also related to the time variation of the lensing potential. Thus, observational data is more sensitive to Σ than μ or γ.

Below, is a list of the other parametrizations used in the literature and how they are related to the (μ,γ) parametrization of Eqs. (3.33)-(3.34):

- In [196], Caldwell, Cooray and Melchiorri introduced

$$\begin{aligned} \mu\gamma &\equiv 1\,, \\ \varpi &\equiv \frac{\gamma-1}{\gamma}\,. \end{aligned} \tag{3.58}$$

- Amendola, Kunz and Sapone [39] considered the two functions Q_A and η_A:

$$\begin{aligned} Q_A &\equiv \mu\gamma, \\ \eta_A &\equiv \frac{1-\gamma}{\gamma}\,. \end{aligned} \tag{3.59}$$

- Zhang *et al*. [37] proposed

$$\begin{aligned} \eta_{ZL} &\equiv \gamma, \\ \tilde{G}_{eff} &\equiv \mu(\frac{\gamma+1}{2}). \end{aligned} \tag{3.60}$$

- Amin, Blandford and Wagoner [197] have introduced

$$\begin{aligned} B_A(\mathcal{H}_k,a) &= \mu = \beta_0(a)+\beta_1(a)\mathcal{H}_k+\beta_2(a)\mathcal{H}_k^2+\dots\,, \\ \Gamma_A(\mathcal{H}_k,a) &= \mu\gamma = \gamma_0(a)+\gamma_1(a)\mathcal{H}_k+\gamma_2(a)\mathcal{H}_k^2+\dots\,. \end{aligned} \tag{3.61}$$

which is a parametrisation designed for small scales with the matter density fluctuation parametrised as

$$\delta_m(a,k) = \delta(k)_i \left[\delta_0(a) + \delta_1(a)\mathcal{H}_k + \delta_2(a)\mathcal{H}_k^2\right], \tag{3.62}$$

where $\delta(k)_i$ is specified by initial conditions. In this approach different theories correspond to different sets of the functions $\{\beta_i, \gamma_i, \delta_i\}$.

3.3 Summary

In this chapter we briefly reviewed a wide range of alternative-gravity theories that modify the Einstein's equations of GR in order to achieve a late time acceleration phase of expansion in the universe, without the need for an extra dark fluid with unusual properties. It was shown how some classes of these theories are in fact related via transformation of coordinate frames.

We then reviewed phenomenological approaches to modified gravity, based on the idea that there are a large number of alternative-gravity theories and they all might be wrong, while testing each of them is a time-consuming procedure. One could instead focus on extracting information from data with model-independent parametrizations of perturbation equations. Developing techniques for efficiently constraining such phenomenological parameters can help detect deviations of these parameters from their default values, if there is any. Of course, one would eventually need to relate a modified behavior to a theoretical foundation.

In Section 3.2.1 we introduced two functions needed to parametrize the evolution of cosmological perturbations on linear scales. We emphasized that there is not a unique choice of these functions, and presented different choices made in the literature. The main benefit of using these functions is that they allow for a model-independent test of the growth dynamics on cosmological scales even though they do not necessarily have a simple form in specific models of MG. In fact, they are defined through solutions of the equations of motion and depend on the choice of the initial conditions; still one can store observable information in these functions in a model independent way, and be careful to correctly translate the findings on these functions into results on the parameters of specific models.

So far, we have explained how the two functions, μ and γ for example, can be used to parametrize the linear growth of perturbations in a general modification of gravity. But, we have not yet introduced any parametrization of such functions yet. When working with a specific theory, our parametrizing functions can be directly calculated. However, we may want to measure these functions from data without any assumption about the underlying theory. Since, in general, we can have as many parameters in these function as we want, the question then is how to balance between simplicity, i.e working with as few parameters as possible, and flexibility in these functions, to capture all of the information contained in the data. In the following chapters, we try to answer this question.

With our closed set of parametrized evolution equations defined, there are two tasks to be fulfilled. One needs to evolve these equations and calculate cosmological observables so that they can be compared to observational data. This will be the subject of the next chapter, where we discuss how the parametrized equations can be implemented into numerical Boltzmann codes. The second task would be to measure these parametrizing functions from data and constrain their values. In Chapters 5 and 6, we discuss the constraints on parametrized modifications to gravity from currently available cosmological observation as well as forcasted constraints from the upcoming experiments.

Chapter 4

MGCAMB

In Chapter 3, we introduced a set of parametrized perturbation equations in the conformal Newtonian gauge, describing the growth of cosmological perturbations at the linear level, while preserving the covariant conservation of the energy-momentum. One then needs to evolve these equations and calculate the predictions for cosmological observables with specific choices of the parametrization. In this chapter, we review the perturbation equations in the synchronous gauge and define their parametrized form corresponding to the ones introduced in Chapter 3 in the conformal Newtonian gauge. We then describe how these equations can be implemented in a commonly used public code, CAMB.

Code for Anisotropies in the Microwave Background (CAMB) [201, 202] uses the equations of GR together with Boltzmann (conservation) equations to calculate cosmological observables. We have introduced a modified version of it, called *Modified Growth with CAMB* (MGCAMB), where we have implemented the parametrized equations[1] [200]. MGCAMB is also compatible with CosmoMC [203], an accompanying code to CAMB for performing Monte-Carlo sampling and constraining cosmological parameters, using CAMB for calculating the theoretical observables.

We introduce some of the functional forms for the (μ, γ) parametrization formulated in 3.2.1 which can describe perturbation equations in specific classes of alternative-gravity theories. We also introduce some of the functional forms for other parametrizations, described in 3.2.2, that have been implemented in MGCAMB.

---

[1] This patch replaces the previously publicly released code MGCAMB [46], while also extending it in several ways as described in [200].

To demonstrate the use of the patch, we obtain joint constraints on the neutrino mass and parameters of a scalar-tensor gravity model from CMB, SNe Ia and the correlation of CMB with large scale structure.

4.1 Linear perturbation equations in the synchronous gauge

In the synchronous gauge, the linearly perturbed line element is

$$ds^2 = a(\tau)^2[-d\tau^2 + (\delta_{ij} + h_{ij})dx^i dx^j]\,, \tag{4.1}$$

where the two scalar DoF of h_{ij} are represented by functions η and h, defined in Fourier space as [18]

$$h_{ij}(\vec{x},\tau) = \int d^3k e^{i\vec{k}\cdot\vec{x}} \left\{ \hat{k}_i\hat{k}_j h(\vec{k},\tau) + (\hat{k}_i\hat{k}_j - \frac{1}{3}\delta_{ij})\, 6\eta(\vec{k},\tau) \right\} . \tag{4.2}$$

The coordinate system in the synchronous gauge, x^μ, can be related to the coordinate system in the conformal Newtonian gauge, $\hat{x}^\mu$, via a transformation of the form

$$x^\mu \rightarrow \hat{x}^\mu = x^\mu + d^\mu(x^\nu)\,. \tag{4.3}$$

Then, the invariance of the line element, ds^2, under this coordinate transformation provides the following relations between the variables in the two gauges [18]

$$\psi = \dot{\alpha} + \mathcal{H}\alpha\,, \tag{4.4}$$

$$\phi = \eta - \mathcal{H}\alpha\,, \tag{4.5}$$

where $\alpha = (\dot{h} + 6\dot{\eta})/2k^2$ is the equivalent of $d^0(x^\nu)$ in Eq. (4.3):

$$\hat{x}^0 = x^0 + \alpha(\vec{x},\tau)\,. \tag{4.6}$$

By substituting Eqs. (4.4)-(4.5) into the Poisson and anisotropy equations in the conformal Newtonian gauge, Eqs. (3.31) and (3.32), we get their analogue form in the synchronous gauge

$$k^2(\dot{\alpha}+\mathcal{H}\alpha) = -\frac{\kappa}{2}\{\rho\Delta+3(\rho+P)\sigma\}\,, \tag{4.7}$$
$$\eta-\mathcal{H}\alpha-(\dot{\alpha}+\mathcal{H}\alpha) = \frac{3\kappa}{2k^2}(\rho+P)\sigma\,. \tag{4.8}$$

We can now parametrize the above equations as

$$k^2(\dot{\alpha}+\mathcal{H}\alpha) = -\frac{\kappa}{2}\mu\{\rho\Delta+3(\rho+P)\sigma\}\,, \tag{4.9}$$
$$\eta-\mathcal{H}\alpha-\gamma(\dot{\alpha}+\mathcal{H}\alpha) = \frac{3\kappa}{2k^2}\mu(\rho+P)\sigma\,, \tag{4.10}$$

where $\kappa \equiv 8\pi G a^2$.

To evolve the four variables $\{\eta, h, \Delta, v\}$ we need two additional equations. As we saw before, the other two equations come from the conservation of the perturbed energy-momentum tensor. In the synchronous gauge, they are [18]

$$\begin{aligned}\dot{\delta} &= -(1+w)\left(\theta+\frac{\dot{h}}{2}\right)-3\frac{\dot{a}}{a}\left(\frac{\delta P}{\delta\rho}-w\right)\delta\,,\\ \dot{\theta} &= -\frac{\dot{a}}{a}(1-3w)\theta-\frac{\dot{w}}{1+w}\theta+\frac{\delta P/\delta\rho}{1+w}k^2\delta-k^2\sigma\,,\end{aligned} \tag{4.11}$$

which are valid separately for each fluid component in the universe. Eqs. (4.9)-(4.11) provide a closed system of equations for evolving our variables in the synchronous gauge.

4.2 Modifying CAMB to implement the parametrized perturbation equations

Following the notation in CAMB, we can define the perturbation to the expansion rate, $\mathcal{Z}$, and shear, σ^* (not to be confused with the anisotropic stress σ), as

$$\mathcal{Z} = \frac{\dot{h}}{2k}\,, \tag{4.12}$$
$$\sigma^* = k\alpha\,. \tag{4.13}$$

With $\mathcal{Z}$ and σ^*, the perturbed Einstein equations are written as [201, 202]:

$$k^2\eta = k\mathcal{H}\mathcal{Z} - \frac{1}{2}\kappa\rho\delta\,, \tag{4.14}$$

$$\frac{2}{3}k^2(\sigma^* - \mathcal{Z}) = \kappa\rho q\,, \tag{4.15}$$

where $\rho q = (\rho + P)v$. As we are interested in testing modifications to GR, we can no longer use Einstein's equations, and instead need an alternative way of evaluating $\mathcal{Z}$ and σ^* based on Eqs. (4.9) and (4.10), combined with the conservation equations. We do this by deriving α and $\dot{h} = 2k^2\alpha - 6\dot{\eta}$ from known quantities, as explained below.

To derive α, we substitute (4.9) into (4.10) and obtain

$$\alpha = \left\{\eta + \frac{\mu\kappa}{2k^2}\left[\gamma\rho\Delta + 3(\gamma-1)(\rho+P)\sigma\right]\right\}/\mathcal{H}\ . \tag{4.16}$$

Then, to get $\dot{\eta}$, we first substitute $\dot{\alpha}$ from (4.9) into (4.10) to write

$$\eta = \mathcal{H}\alpha - \frac{\mu\kappa\rho}{2k^2}\Gamma\,, \tag{4.17}$$

where

$$\Gamma = \gamma\Delta + 3(1+w)\sigma(\gamma-1)\ . \tag{4.18}$$

The time derivative of (4.17) gives

$$\dot{\eta} = \dot{\mathcal{H}}\alpha + \mathcal{H}\dot{\alpha} - \frac{\mu\kappa\rho}{2k^2}\left\{2\mathcal{H}\Gamma - 3\mathcal{H}(1+w)\Gamma + \frac{\dot{\mu}}{\mu}\Gamma + \dot{\Gamma}\right\}\ . \tag{4.19}$$

Using the conservation equations (4.11) in the above, we have the final expression for $\dot{\eta}$:

$$\begin{aligned}\dot{\eta} \;=\;& \frac{\kappa\rho}{2\mathcal{D}}\{(1+w)\left[\mu\gamma\theta\left(1+\frac{3\kappa\rho}{2k^2}(1+w)\right)+k^2\alpha(\mu\gamma-1)\right]+\Delta\left[\mu(\gamma-1)\mathcal{H}-\dot{\mu}\gamma-\dot{\gamma}\mu\right]\\ &+\;3\dot{\sigma}(1+w)(1-\gamma)\mu+3\sigma(1+w)\left[3w\mu(\gamma-1)\mathcal{H}-(\gamma-1)\dot{\mu}-\mu\dot{\gamma}\right]\}\ ,\end{aligned} \tag{4.20}$$

where $\mathcal{D}$ is

$$\mathcal{D} = k^2 + \frac{3\kappa}{2}\gamma\mu\rho(1+w)\ . \tag{4.21}$$

With α, $\dot{\eta}$ and $\dot{h}$ in hand, we can evaluate $\mathcal{Z}$ and σ^* in Eqs. (4.12)-(4.13).

In CAMB, cosmological observables are calculated in the form of angular power spectra. For computing these power spectra, GR equations are used to simplify the expressions in the code. Hence, one needs to identify the occasions where GR equations are used and replace them with the parametrized expressions. In the following, we describe how this is done for two power spectra which we will later use: CMB temperature and CMB/LSS cross-correlation power spectra.

Alterations to the CMB source function in CAMB.

The CMB temperature angular spectrum C_ℓ^{TT} can be written as

$$C_\ell^{TT} = (4\pi)^2 \int k^2 dk P(k) [I_\ell^T(k)]^2 \,, \tag{4.22}$$

where $P(k)$ is the primordial power spectrum and

$$I_\ell^T(k) = \int_0^{\tau_0} d\tau S_T(k,\tau) j_\ell(k\tau) \,, \tag{4.23}$$

where τ is the conformal time, $S_T(k,\tau)$ is the source term, and $j_\ell(x)$ are spherical Bessel functions. In GR, the source term in terms of the synchronous gauge variables is [204]

$$\begin{aligned} S_T(k,\tau) &= g\left(\Delta_0^T + 2\dot{\alpha} + \frac{\dot{v}_b}{k} + \frac{\Pi}{4} + \frac{3\ddot{\Pi}}{4k^2}\right) \\ &+ e^{-\kappa}(\dot{\eta} + \ddot{\alpha}) + \dot{g}\left(\alpha + \frac{v_b}{k} + \frac{3\dot{\Pi}}{2k^2}\right) + \frac{3\ddot{g}\Pi}{4k^2} \end{aligned} \tag{4.24}$$

where,κ is the optical depth [2], g is the visibility function defined in terms of the optical depth as

$$g(\tau) \equiv \dot{\kappa} \exp(-\kappa) \,, \tag{4.25}$$

and $\Pi = \Delta_2^T + \Delta_2^P + \Delta_0^P$. $\Delta_\ell^T (\Delta_\ell^P)$ are the ℓ'th moments of $\Delta^T (\Delta^P)$ in term of Legendre polynomials [204]:

$$\Delta^T(\hat{n}) = \sum_{l=0}^{\infty} \sum_{m=-l}^{l} a_{lm} Y_{lm}(\hat{n}) \,, \tag{4.26}$$

---

[2] Note that only in Eqs. (4.24)-(4.25), κ is considered as the optical depth.

where $\hat{n}$ is a direction in the sky.

In the default version of CAMB, the perturbed Einstein equations are used in the evaluation of the source $S_T(k,\tau)$. Since we have introduced modifications to the Poisson (4.9) and anisotropy (4.10) equations, it is important to avoid assuming GR in the expression for the source. The MGCAMB patch replaces the default CMB source in CAMB with the modified version of Eq. (4.24). In addition, the evaluation of the ISW term, $e^{-\kappa}(\dot{\eta}+\ddot{\alpha})$, in (4.24) is modified. Namely, it was originally given by

$$\dot{\eta}+\ddot{\alpha}=\frac{\kappa}{2k^2}\left[2(\dot{\rho}\Delta+\rho\dot{\Delta})+\frac{3}{2}(\rho+P)\dot{\sigma}+\frac{3}{2}(\dot{\rho}+\dot{P})\sigma\right] , \tag{4.27}$$

while in MGCAMB Eqs. (4.16-4.19) are used to modify the above expression as

$$\dot{\eta}+\ddot{\alpha}=\frac{\kappa}{2k^2}\left\{-\left[(\gamma+1)(\dot{\rho}\Delta+\rho\dot{\Delta})+\gamma\frac{3}{2}(\rho+P)\dot{\sigma}+\gamma\frac{3}{2}(\dot{\rho}+\dot{P})\sigma\right]+\dot{\gamma}\mu\left[(\rho\Delta)+\frac{3}{2}(\rho+P)\sigma\right]\right\} . \tag{4.28}$$

It can be easily checked that for $\mu=\gamma=1$, we get back the ISW term in GR.

Alterations to the CMB-LSS cross-correlation patch of Ho et al.

To be able to use the ISW data, we need to calculate the theoretical CMB-LSS cross-correlation angular spectrum, C_ℓ^{gT}. In the parametrized modified gravity formalism, the source terms should be modified. C_ℓ^{gT} can be written as[3]

$$C_\ell^{gT}=\frac{2}{\pi}\int k^2 dk P(k) g_\ell(k) T_\ell(k) , \tag{4.29}$$

with

$$g_\ell(k)=\int dz\, b(z) W(z) D(k,z) j_\ell(k\chi(z)) , \tag{4.30}$$

and

$$T_\ell(k)=3\frac{H_0^2}{c^2}\Omega_m T_{\rm CMB}\times\int dz\frac{d}{dz}\left[D(k,z)(1+z)\right]\frac{j_\ell(k\chi(z))}{k^2} , \tag{4.31}$$

where $W(z)$ is the normalized selection function, $T_{\rm CMB}$ is temperature of CMB today, $\chi(z)$ is the comoving distance to redshift z, $b(z)$ is the bias factor, integration over τ is replaced

---

[3] Note that the different pre-factor, $(2/\pi)$ in Eq. (4.29) rather than $(4\pi)^2$ in (Eq. (4.22)), is due to different Fourier conventions [205].

with integration over redshift and the growth factor $D(k,z)$ is defined as

$$\frac{\delta(k,z)}{\delta(k,0)} = \frac{D(k,z)}{D(k,0)} \,. \tag{4.32}$$

Expression (4.29) can be simplified for $\ell \gtrsim 10$ by working in the flat-sky approximation and substituting $k = (\ell+1/2)/\chi(z)$, which gives [206]

$$C_\ell^{gT} = \frac{3\Omega_m H_0^2 T_{\rm CMB}}{c^2(\ell+1/2)^2} \times \int dz b(z) W(z) \frac{H(z)}{c} D(k,z) \frac{d}{dz}[D(k,z)(1+z)] P\left(\frac{\ell+1/2}{\chi}\right) \tag{4.33}$$

In a general theory of gravity, the growth factor can have a complicated form depending both on scale and time. With Eqs. (4.9) and (4.10), it is straightforward to show that at late times, when the anisotropic stress due to relativistic species is negligible, Eq. (4.33) is modified to

$$C_\ell^{gT} = \frac{3\Omega_m H_0^2 T_{\rm CMB}}{c^2(\ell+1/2)^2} \times \int dz b(z) W(z) \frac{H(z)}{c} D(k,z) \frac{d}{dz}[D(k,z)(1+z)\mu(k,z)(1+\gamma(k,z))] P\left(\frac{\ell+1/2}{\chi}\right) \tag{4.34}$$

where $D(k,z)$ is still defined as Eq. (4.32) and we use MGCAMB to calculate $D(k,z)$ from Eq. (4.32) at each redshift and also the modified matter power spectrum today, $P((\ell+1/2)/\chi)$. The derivative of the growth factor with respect to redshift can be calculated using Eqs. (4.10)-(4.11) and the corresponding expressions for $\mu(k,z)$ and $\gamma(k,z)$.

4.3 Specific parametric forms of μ and γ

While MGCAMB works for any form of $\mu(k,a)$ and $\gamma(k,a)$ supplied by the user, we have coded in several specific parametrizations previously used in the literature. For example, a particular form of μ and γ that holds approximately in some classes of $f(R)$ and scalar-tensor theories was introduced in [41], hereafter referred to as the BZ parametrization:

$$\begin{aligned} \mu(k,a) &= \frac{1+\beta_1\lambda_1^2 k^2 a^s}{1+\lambda_1^2 k^2 a^s}\,, \\ \gamma(k,a) &= \frac{1+\beta_2\lambda_2^2 k^2 a^s}{1+\lambda_2^2 k^2 a^s}\,, \end{aligned} \tag{4.35}$$

where β_i's are dimensionless couplings and λ_i's have dimension of length. Specific sets of BZ parameter values can be chosen to correspond to particular $f(R)$ and scalar-tensor models. Moreover, not all of the BZ parameters are independent. For example, $f(R)$ models, with the action (3.10), can be tuned to reproduce any background expansion history, and the remaining relevant quantity is the squared Compton wavelength of the new scalar degree of freedom $f_R \equiv df/dR$ mediating the fifth force. In units of the Hubble length squared it is given by [207, 185]

$$B \equiv \frac{f_{RR}}{1+f_R}\frac{dR}{d\ln a}\left(\frac{d\ln H}{d\ln a}\right)^{-1}, \tag{4.36}$$

where R is the background Ricci scalar. Thus, for a fixed background expansion history, different $f(R)$ models can be parametrized by the parameter B_0, which is the value of B today. It was suggested in [208] that for $B_0 \lesssim 1$ the large scale growth in $f(R)$ models can be modelled using a BZ form with $\beta_1 = 4/3$, $\lambda_2^2 = \beta_1\lambda_1^2$ and $\beta_2 = 1/2$ as:

$$\mu(k,a) = \frac{1}{1-1.4\cdot 10^{-8}|\lambda_1|^2 a^3}\,\frac{1+\frac{4}{3}\lambda_1^2 k^2 a^4}{1+\lambda_1^2 k^2 a^4} \qquad \gamma(a,k) = \frac{1+\frac{2}{3}\lambda^2 k^2 a^4}{1+\frac{4}{3}\lambda^2 k^2 a^4}\,, \tag{4.37}$$

where the pre-factor is introduced to account for the background rescaling of the Newton's constant which becomes important when $B_0 \gtrsim 0.5$ and $\lambda_1^2 = B_0 c^2/(2H_0^2)$. We will use this parametrization in the next section to demonstrate the use of MGCAMB and to constrain the B_0 parameter.

Similarly, models with a Yukawa–type dark matter interaction can also be approximately expressed in terms of the extended BZ parametrization of [208]. In this type of models, the allowed ranges of the BZ parameter values are $0 < B_0 = 2\lambda_1^2 H_0^2/c^2 < 1$, $0 < \beta_1 < 2$ and $1 < s < 4$, while $\lambda_2^2 = \beta_1\lambda_1^2$ and $\beta_2 = 2/\beta_1 - 1$, where the parameter B_0 is again related to the Compton wavelength of the extra scalar degree of freedom. As shown in [208], and in the next section, the data considered here cannot constrain parameters B_0 and s in this model.

Parametric forms such as (4.35) or (4.37) are certainly not guaranteed to be accurate in representing solutions of all $f(R)$, scalar-tensor or other MG models at all values of the theoretical parameters. The validity of the original BZ form (4.35) has been questioned in [209], where a more accurate parametric form specific to $f(R)$ was suggested. At small B_0, which are not already ruled out, BZ parametrization still works fine. In Section 4.4 we demonstrate the use of MGCAMB by working with the modified BZ form (4.37) of [208] that has the additional pre-factor in μ.

Alternative parametrizations

As discussed before, the parametrized modification of perturbed Einstein equations can be done in different ways. Other forms may be useful when working with specific cosmological observables or when testing particular theories. Generally, it should be possible to express these other parametrizations in terms of μ and γ. For example, in certain circumstances, it can be desirable to work with functions μ and Σ, defined in Eq. (3.57). In [210] it was shown that working with these functions clearly captures the complementary information in weak lensing and peculiar velocity experiments. Another advantage of working with Σ is that in scalar-tensor or higher-dimensional theories, such as DGP, Σ is close to 1 on small scales [211].

In [212], functions $Q(k,a)$ and $R(k,a)$ were introduced as

$$\begin{aligned} k^2\Phi &= -4\pi G a^2 Q \rho\Delta\,, \\ k^2(\Psi - R\Phi) &= -12\pi G a^2 Q(\rho+P)\sigma\,, \end{aligned} \tag{4.38}$$

which we include as an alternative parametrization in MGCAMB. Namely, when the appropriate option is selected, Eqs. (4.38) are evolved in place of (4.9) and (4.10). A phenomenological functional forms of Eq. (4.38) is chosen in [212] as

$$\begin{aligned} Q(k,a)-1 &= \left[Q_0 e^{-k/k_c} + Q_\infty(1-e^{-k/k_c}) - 1\right] a^s \\ R(k,a)-1 &= \left[R_0 e^{-k/k_c} + R_\infty(1-e^{-k/k_c}) - 1\right] a^s \end{aligned} \tag{4.39}$$

which is implemented in MGCAMB accordingly. Functions Q and R are simply related to μ and γ in the limit of negligible anisotropic stress σ:

$$Q = \mu\gamma\,, \quad R = \gamma^{-1}\,, \tag{4.40}$$

although we do not rely on this conversion in practice. As a consistency check, we have reproduced some of the results in [212] using MGCAMB.

4.4 A worked example: joint constraints on massive neutrinos and modified gravity

To demonstrate the use of MGCAMB in conjunction with CosmoMC, we performed a joint analysis of CMB, ISW and SNe Ia data to constrain a particular set of modified gravity (MG) parameters together with the total neutrino mass. Massive neutrinos can modify the growth of structure on different scales and redshifts depending on their mass. This modification can, in principle, be degenerate with the effects of MG on the overlapping scales and redshifts. To study the degeneracy between MG parameters and basic cosmological parameters, including the neutrino mass, we chose two specific parametrized MG models, namely, the $f(R)$ and Yukawa-type models introduced in [208] (see Eq. (4.37)). Cosmological constraints on $f(R)$ models were also studied in [213].

On linear scales, modified gravity models, such as $f(R)$, generally predict enhanced growth on the scales smaller than the Compton wavelength due to the fifth force, while massive neutrinos can damp the structure within their free-streaming scale, which is determined by the neutrino mass. Therefore, it is interesting to study the degeneracy between the MG parameters and the neutrino mass. Fig 4.1 shows the CMB TT power spectra for ΛCDM, an "$f(R)$ model" described by Eq. (4.37) with $B_0 = 0.5$ and the case of massive neutrinos with $f_\nu \equiv \Omega_\nu/\Omega_{CDM} = 0.05$ corresponding to $\sum m_\nu \simeq 0.5$eV. We attempted to constrain four models: the $f(R)$ and Yukawa-type, described by (4.37), each with and without the presence of massive neutrinos. In all the cases, we varied the 7 primary parameters as explained in Table 4.1. In addition, we varied f_ν for the cases with neutrinos, B_0 in the case of $f(R)$ and $\{B_0, \beta_1, s\}$ for the Yukawa model.

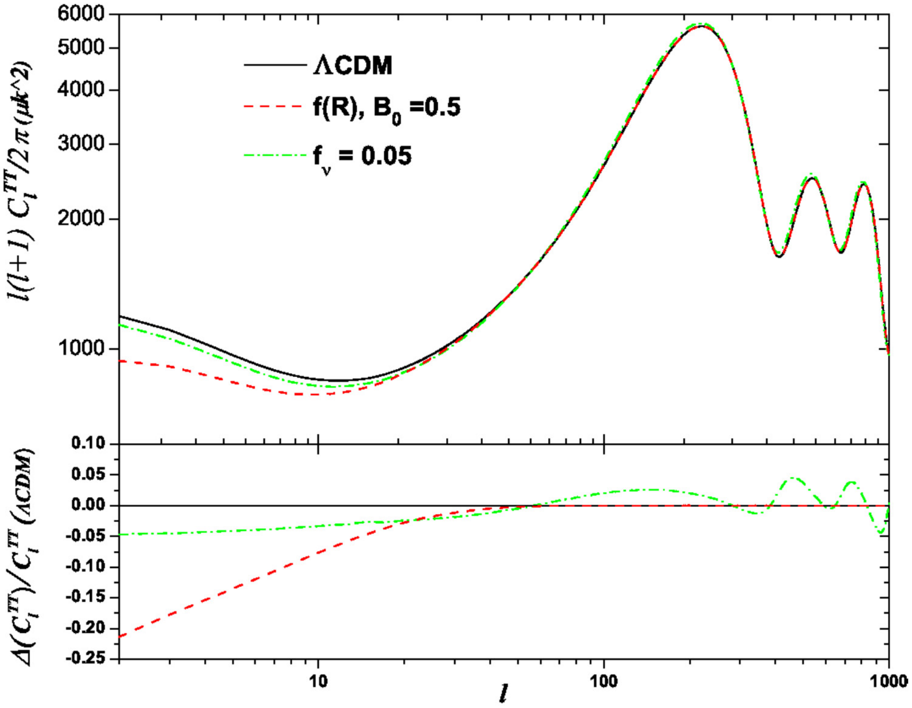

Figure 4.1: CMB TT power spectrum for ΛCDM (black solid), $f(R)$ model with $B_0 = 0.5$ (red dashed) and ΛCDM+massive neutrino models with $f_\nu = 0.05$ (green dash-dotted).

We utilized MGCAMB to calculate the CMB angular spectrum and the CMB/matter cross-correlation spectrum, as well as the SNe and BAO, and used a modified version of CosmoMC to fit the models to data. We used the CMB data from the WMAP seven year observation [214], and the CMB-large scale structure (LSS) cross-correlation data by Ho et al [206]. We also used the SNe Ia data (SDSS compilation) [215], the HST data from [216] and the BAO data from [21] to further constrain the background expansion history. In addition, we put a top hat prior of $[10,20]$ Giga years on the age of the universe. Given the observational data, we use CosmoMC to sample the parameter space using the Metropolis-

Parameter	Explanation	range (min, max)	
	Primary parameters	$f(R)$	Yukawa–type
ω_b	physical baryon density; $\omega_b = h^2\Omega_b$	$(0.005, 0.100)$	
ω_c	physical CDM density; $\omega_c = h^2\Omega_c$	$(0.01, 0.99)$	
ϑ_*	sound horizon angle; $\vartheta_* = 100 \cdot r_s(z_*)/D_A(z_*)$	$(0.5, 10.0)$	
κ	optical depth to reionisation	$(0.01, 0.80)$	
$\ln(10^{10}A_s^2)$	A_s is the scalar primordial amplitude	$(2.7, 4.0)$	
A_{SZ}	amplitude of the SZ template for WMAP and ACBAR	$(0, 2)$	
n_s	spectral index of primordial perturbations; $n_s - 1 = d\ln P/d\ln k$	$(0.5, 1.5)$	
	Neutrino parameters	$f(R)$	Yukawa–type
f_ν	fraction of dark matter density as massive neutrinos	$(0.0, 0.1)$	
	MG parameters	$f(R)$	Yukawa–type
B_0	present lengthscale of the theory (in units of the horizon scale)	$(0, 1)$	$(0, 1)$
β_1	coupling	$4/3$	$(0.001, 2)$
s	time evolution of the scalaron mass	4	$(1, 4)$

Table 4.1: List of the parameters used in the Monte Carlo sampling. The ranges of the flat priors are given if a parameter is varied, or the value is given if the parameter was fixed.

Hastings algorithm. Table 4.1 shows the parameters we used for sampling and the assumed priors. We run several chains, and obtained the constraints after the chains converged perfectly.

Figs. 4.2-4.4 show the 1-D posterior distributions, and the 2-D contour plots of the cosmological and MG parameters for the $f(R)$ and Yukawa-type models with and without massive neutrinos. We did not see a significant correlation between the neutrino mass and the MG parameters. This is because the MG models we have considered primarily affect the CMB spectrum via the ISW effect, which is relevant on large scales, or small ℓ. On the other hand, the effect of (small) neutrino mass on the CMB spectrum is quite subtle and the constraint comes primarily from ℓ around the acoustic peaks.

The correlation between the neutrino mass and MG would be more prominent if we considered their effect on the matter power spectrum data $P(k)$. However, adding the $P(k)$ information is non-trivial for the following reason. The MCMC module of Ho et al [206] is a compilation of clustering data from several surveys, and $P(k)$ from each data set is used in determining the bias, which is then used to determine the cross-correlation of clustering with CMB. So, in effect, $P(k)$ is used, but only in determining the bias, and not in constraining cosmological parameters. Same method was used in [217] and in [218]. In principle, one can include $P(k)$ into the data while properly accounting for the covariance with cross-correlation.

For the $f(R)$ model, we find that the B_0 parameter is constrained to be $B_0 < 0.4$ (95% C.L.), which corresponds to $\lambda_1^2 < 1900$ Mpc/h. The constraint on B_0 is practically unchanged after marginalizing over the neutrino mass. For the Yukawa model, we find that $0.7 < \beta_1 < 1.7$ (95% C. L.), while B_0 and s are very weakly constrained. In both cases, we find $f_\nu \lesssim 0.05$ at 95% C.L., implying $\sum m_\nu \lesssim 0.5$ eV. Our constraints on the MG parameters are consistent with those presented in Refs. [208, 217]. The analysis of Ref. [208] is based on a different compilation of ISW datasets – we used Ho et al. [206], while they used the compilation of Giannantonio et al. [218]. Our results are also in good agreement with those of Ref. [217], where the PPF framework [182, 219] employing a different set of equations was used. When the Ho et al. [206] dataset was considered in [217], it leads to a constraint of $B_0 < 0.4$ (95% C.L.) on $f(R)$ models.

4.5 Summary

In this chapter, we reviewed the linear equations for scalar perturbation of the FRW metric in the synchronous gauge and described how they can be parametrized to accommodate modifications to GR equations from alternative gravity models. We then introduced a patch to CAMB and CosmoMC, called MGCAMB, that makes it possible to evaluate cosmological observables using the parametrized equations. The motivation for this parametrization in terms of functions $\mu(a,k)$ and $\gamma(a,k)$, its consistency, and the relation to other models in the literature has been discussed in Chapter 3. Its main value is in allowing for a model-independent way of looking for departures from GR [220]. However, it is also possible to derive approximate expressions for $\mu(a,k)$ and $\gamma(a,k)$ in terms of fundamental parameters of particular theories [187, 208].

We have demonstrated the utility of the MGCAMB code by obtaining joint constraints on the neutrino mass and parameters of two models of modified gravity previously considered in [208]. We found that GR remained a good fit in all cases. In the case of $f(R)$ we found that the B_0 parameter was constrained to be $B_0 < 0.4$ (95% C.L.), which corresponded to $\lambda_1^2 < 1900$ Mpc/h. In the case of Yukawa type models we found that $0.7 < \beta_1 < 1.7$ (95% C. L.), while B_0 and s were very weakly constrained. In both models there was little degeneracy between the neutrino mass and the MG parameters, with the neutrino fraction constrained to be $f_\nu \lesssim 0.05$ at 95% C.L.

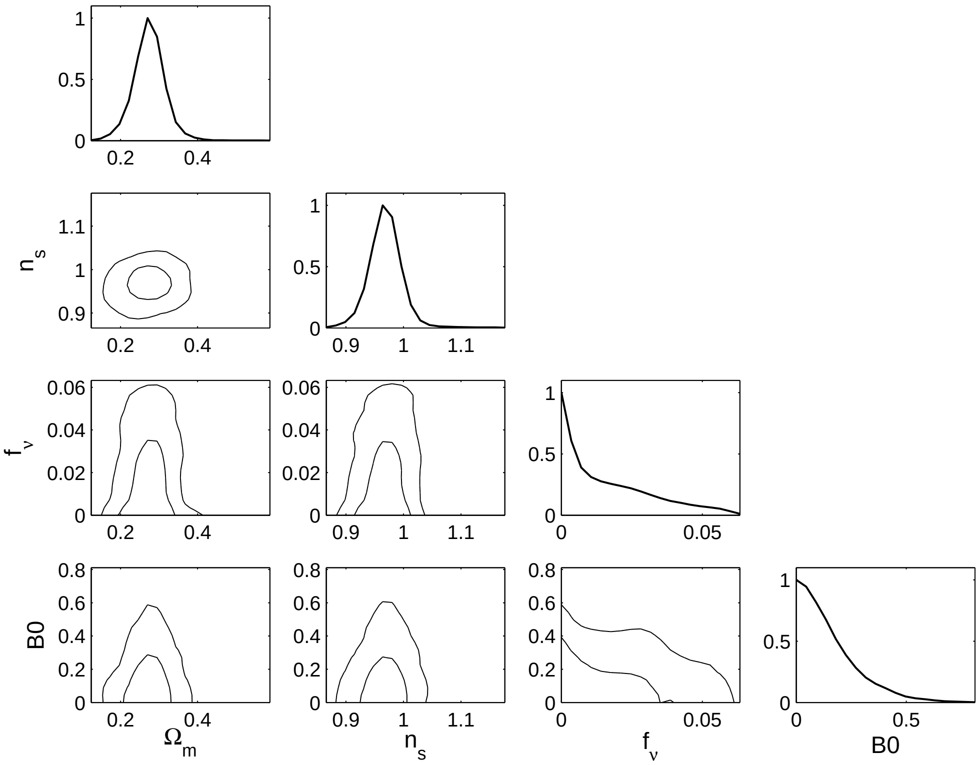

(a) With massive neutrinos

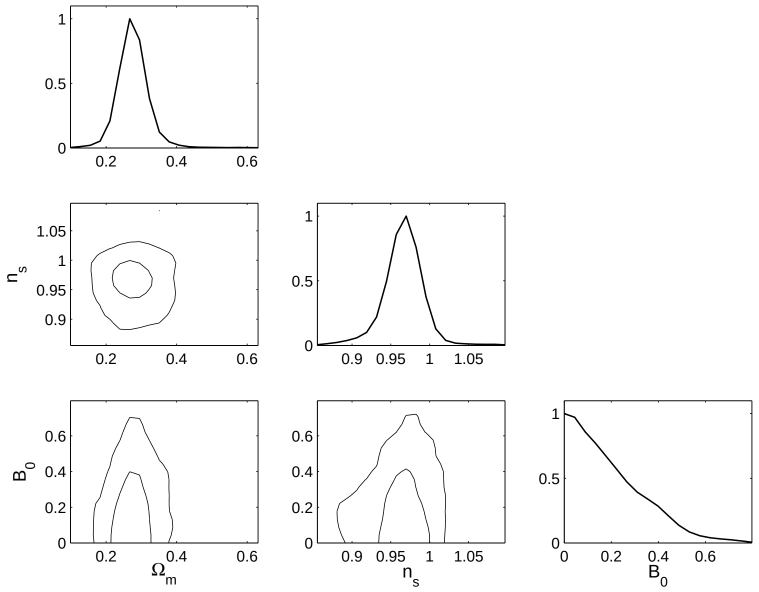

(b) Without massive neutrinos

Figure 4.2: Marginalized posterior distribution for the $f(R)$ model parameters and 2-D contour plots showing the ranges of and correlations between parameters of interest and the 68 and 95% confidence limits.

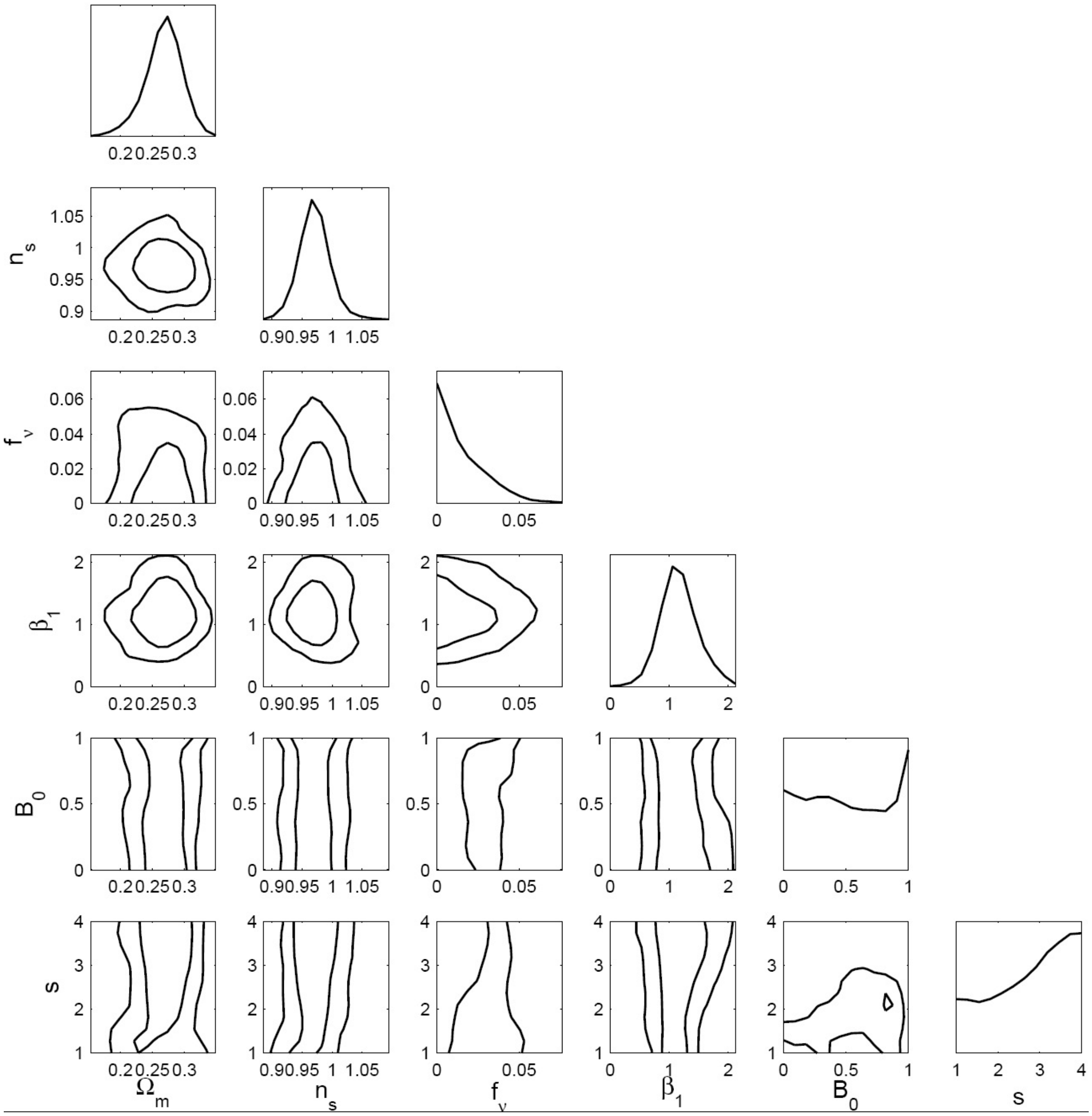

Figure 4.3: Same as in Fig 4.2 but for the Yukawa-type model with massive neutrinos.

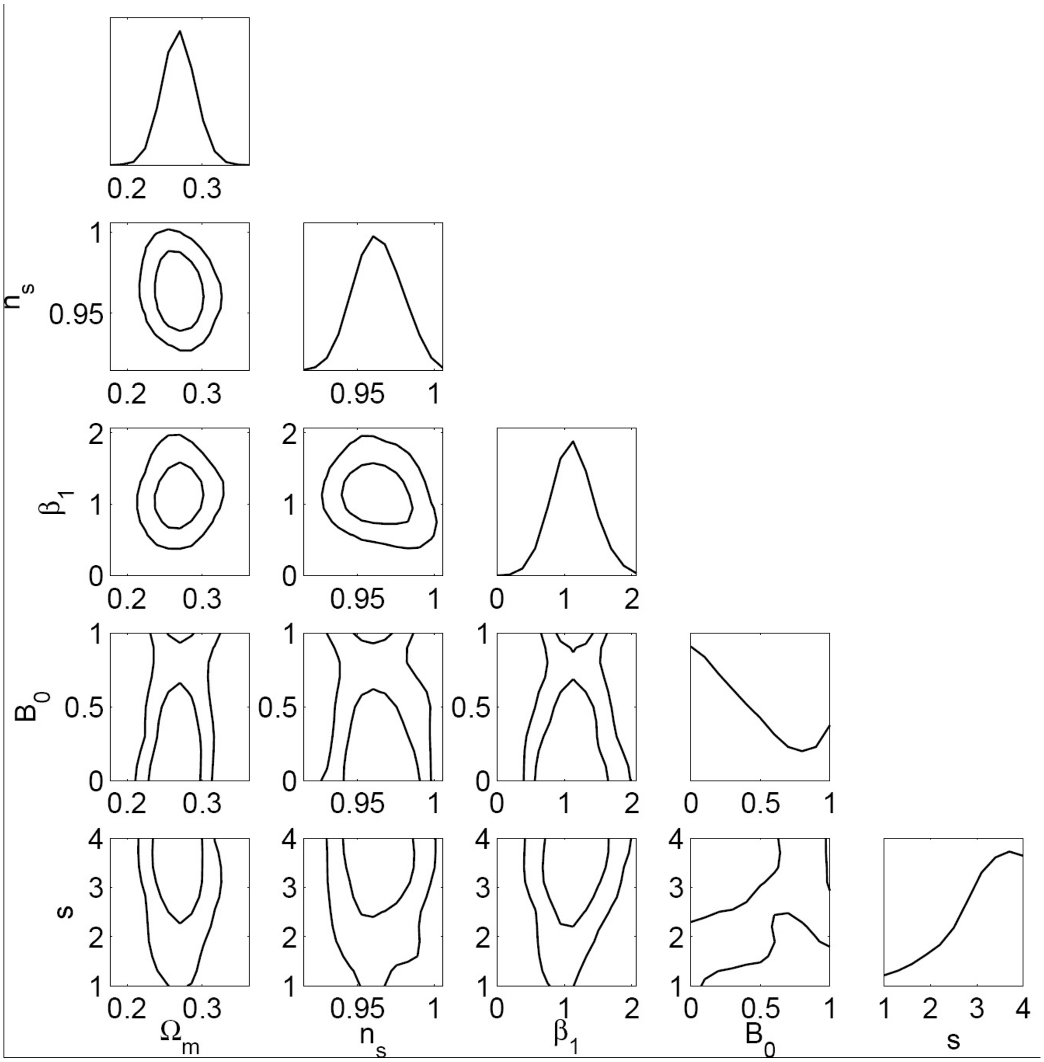

Figure 4.4: Same as in Fig 4.2 but for the Yukawa-type model without massive neutrinos.

Chapter 5

Cosmological tests of general relativity: a PCA approach

The next generation of large scale structure surveys are sensitive enough to discriminate between different theories of alternative gravity and exotic DE and enable us to test the ΛCDM model. These surveys will trace the evolution of matter perturbations and gravitational potentials from the matter dominated epoch until today. Along with constraining the dynamics of DE, they will probe the relations between matter overdensities, local curvature, and the Newtonian potential. The parametrized framework introduced in Chapters 3 and 4 can, in principle, accommodate any modifications of these relations in the linear regime from the ΛCDM predictions.

In this chapter, we treat the functions parametrizing the linear equations of motion (MG functions) in a less model-dependent way by working with bins of these functions on a grid of scale and redshift. We take these 2-D bins (MG pixels) to be part of the model parameters and perform a Fisher information analysis (5.3) to estimate the constraints on the MG pixels for surveys like DES [35] and LSST [36]. We then perform a PCA (5.4) to find the eigenmodes and eigenvalues of these functions. The number of well-constrained modes approximately corresponds to the number of degrees of freedom (DoF) of these functions that can be measured by the surveys. Their scale and time dependence indicate the ranges where the surveys will be most likely to detect deviations from ΛCDM. This approach was first introduced in [220] and developed in [47].

we consider the impact of some of the systematic effects expected in weak lensing surveys. We also present the PCA in terms of other choices of the two MG functions needed to parameterize modified growth on linear scales, and discuss their merits. In addition, we analyze the degeneracy between the MG functions and other cosmological parameters, paying special attention to the effective equation of state $w(z)$. Finally, we demonstrate the utility of the PCA in storing data about the linear growth of structure, efficiently and compressed. We demonstrate how having this information stored in PCs will also enable one to easily derive constraints on parameters of specific models without recalculating Fisher matrices from scratch for each model separately.

5.1 MG pixels as model parameters

Our goal is to determine how well μ and γ can be constrained by future surveys, minimizing any assumption on the functions themselves. Therefore, rather than employing a specific expression for μ and γ, we will treat them as unknown functions of both time and scale, and *bin* them on a grid in the (z,k) space. With m z-bins and n k-bins, we have $m \times n$ grid points to which we associate a pair of values of the two functions. This is a 2×2-dimensional problem, with the value of the functions at each pixel represented by μ_{ij} and γ_{ij}. However, in practice, one can transform the 2-D problem into a 1-D one by mapping the grid into a chain, therefore transforming the matrices of values into two $m \times n$-dimensional vectors [220]. We indicate the components of the vectors with μ_i and γ_i where $i = 1, \ldots, m \times n$. In addition, we also bin the DE equation of state $w(z)$ in redshift, creating a m-dimensional vector and vary the usual cosmological parameters: the Hubble constant h, cold dark matter density $\Omega_c h^2$, the baryon density $\Omega_b h^2$, the optical depth τ, the scalar spectral index n_s, and the amplitude of scalar perturbations A_s. We assume that the bias is scale-independent on the linear scales considered in our analysis and introduce N_b constant bias parameters, one for each photometric bin of the survey.

We use the Fisher matrix formalism to estimate the anticipated covariance of our parameters p_i, $i = 1, \ldots, 2 \times m \times n + m + 6 + N_b$. After choosing our observables and experiments as described in next section, we build the Fisher information matrix for the parameters p_i. Then, we invert it to determine the anticipated covariance matrix

$$C_{ij} \equiv \langle (p_i - \bar{p}_i)(p_j - \bar{p}_j) \rangle \ , \tag{5.1}$$

where $\bar{p}_i$ are the assumed best fit, or "fiducial", values.

5.1.1 Covariance matrix for Σ

Depending on the circumstances, it can be preferable to replace γ with the function Σ defined in Eq. (3.57), and work with the combination (μ,Σ). In that case, one way to proceed is to repeat the procedure outlined in Sec. 5.4 for the new combination (μ,Σ). Alternatively, one can use the information already stored in the (μ,γ) pixels to infer the covariance matrix for Σ, which is what we will do. From Eqs. (3.33)-(3.34) and (3.57), we have

$$\Sigma = \frac{1}{2}\mu(1+\gamma)\,. \tag{5.2}$$

Then, pixelizing Σ on the same (k,z) grid, we can derive its covariance matrix in terms of the covariance matrix elements for μ and γ as

$$\begin{aligned} C_{ij}^{\Sigma\Sigma} &= \frac{1}{4}[\mu_i\mu_j C_{ij}^{\gamma\gamma} + (1+\gamma_i)(1+\gamma_j)C_{ij}^{\mu\mu} \\ &+ \mu_i(1+\gamma_j)C_{ij}^{\gamma\mu} + \mu_j(1+\gamma_i)C_{ij}^{\mu\gamma}], \end{aligned} \tag{5.3}$$

where, for example, $C_{ij}^{\gamma\mu}$ is the covariance between γ_i and μ_j. Analogously, one can derive the covariance of Σ with μ, $C^{\Sigma\mu}$.

5.2 Observables

The ongoing and future tomographic large scale structure surveys (like DES [35], PAN-STARR [221] and LSST [36]) will provide measurements of galaxy number counts (GC) and weak lensing (WL) on the same patch of sky, as well as a large number of SNe Ia. This, in combination with the full sky CMB data from WMAP and Planck, allows us to consider all possible cross-correlations: CMB-WL, CMB-LSS, LSS-WL, in addition to the three auto-correlation functions. Measuring the lensing and the Newtonian potentials via these observables will constrain μ and γ. In what follows, we provide a brief overview of the observables we used for the analysis and the assumptions we have made about the experiments .

We numerically evaluate the transfer functions I_ℓ, Eq. (1.67), using MGCAMB [45] and obtain the angular spectra C_l^{XY}. A joint analysis of CMB and data from a tomographic lensing survey with M GC redshift bins and N WL bins will give us a total of $3+M(M+1)/2+N(N+1)/2+M+N+MN$ different types of C_ℓ's respectively from CMB, GC, WL, GC×CMB, WL×CMB and WL×GC, (we do not correlate CMB polarization with GC and WL because the signal is too weak). For example, combining Planck with DES, with $M=4$ GC bins and $N=4$ WL bins, gives us 47 different types of spectra. A combination of Planck with LSST, with 10 GC bins and 6 WL bins, gives us 155 different C_ℓ's.

We only use the parts of the spectra that correspond to the linear cosmological regime. Including higher ℓ, or smaller scales, would require us to account for non-linear effects which, strictly speaking, are not allowed within our framework. To accurately model growth on non-linear scales, one needs input from N-body simulations, which can only be performed for specific modified gravity theories. The fact that we are not testing a specific model, but constraining a general departure from GR, defined in terms of linear perturbation variables, precludes us from having a reliable description of non-linear corrections. We restrict ourselves to the linear regime by cutting off the C_ℓ^{XY} spectra at $\ell_{\rm max} \sim 0.2\, h\, r(z_s)$. This cutoff roughly corresponds to $k_{\rm max} \sim 0.2\, h\text{Mpc}^{-1}$ at $z=0$. There is certainly a wealth of information about MG parameters on smaller scales [222], and while it would be tempting to include it in our analysis, it would make our predictions unreliable since our analysis is limited to linear theory.

5.2.1 Experiments

For this analysis, we include CMB temperature and polarization (T and E), WL of distant galaxies, GC, their cross-correlations, and SNe observations. We assume CMB T and E data from the Planck satellite [226], the galaxy catalogues and WL data by the Dark Energy Survey [35] and Large Synoptic Survey Telescope (LSST) [36], complemented by a SNe data set provided by the futuristic Euclid-like survey [223].

DES and LSST

DES is a project aimed at studying the nature of the cosmic acceleration, and is planned to start observations in 2012 [35]. DES includes a 5000 square degree multi-band, optical survey probing the redshift range $0.1 < z < 1.3$ with a median redshift of $z = 0.7$ and an approximate 1-σ error of 0.05 in photometric redshift (see 1.3.2 for details on galaxy number count). In the simulation, for both WL and GC, a sky fraction $f_{\rm sky} = 0.13$, and an angular density of galaxies $N_G = 10$ gal/arcmin^2 is assumed. We also assume $\gamma_{\rm rms} = 0.18 + 0.042\,z$, which is the rms shear stemming from the intrinsic ellipticity of the galaxies and measurement noise, and the photometric redshift uncertainty given by $\sigma(z) = 0.05(1+z)$.

LSST is a proposed large aperture, ground-based, wide field survey telescope [36]. It is expected to cover up to half of the sky and catalogue several billion galaxies out to redshift $z \sim 3$. For LSST forecasts, we adopt parameters from the recent review paper by the LSST, we use $f_{\rm sky} = 0.5$, $N_G = 50$ gal/arcmin^2 for both WL and counts, $\gamma_{\rm rms} = 0.18 + 0.042\,z$, and $\sigma(z) = 0.03\,(1+z)$ [227].

For both DES and LSST, we take the GC photometric bins to be separated by $5\sigma(z)$. This leads to four redshift bins for DES and ten for LSST. For WL (source) galaxies, we use four bins for DES and six for LSST.

CMB, SNe Ia, and other priors on cosmological parameters

In our forecasts, we assume spatially flat geometry and parametrize the dark energy equation of state using 20 bins from $z = 0$ to $z = 3$ uniform in z, and one wide bin from $z = 3$ to $z = 1100$. In addition to the MG parameters, and the $N_b \equiv M$ bias parameters, we vary h, $\Omega_c h^2$, $\Omega_b h^2$, τ, n_s, and A_s. Their fiducial values are taken to be those from the WMAP 7-year data best fit [52]: $\Omega_b h^2 = 0.023, \Omega_c h^2 = 0.11, h = 0.71, \tau = 0.088, n_s = 0.963$. The fiducial values for bias parameters are motivated by the parametrized halo model described in [224]. Imposing a prior on the value of h from the Hubble Space Telescope (HST) did not make a noticeable difference in our results.

We assume the expected CMB data from the Planck mission [226] of the European Space Agency (ESA) using the same parameters as in [45]. In addition, to better constrain the background expansion parameters, we include simulated SNe luminosity data for a Euclid-like survey, *e.g.*, the one proposed in [223]. We generate 4012 data points randomly distributed in 14 redshift bins from $z = 0.15$ to $z = 1.55$, and add 300 low-z SNe from the Nearby Supernova Factory (NSNF) survey [225]. We calculate the exact distance modulus for each model, and put a Gaussian noise with rms error of $\sigma = 0.13$ to displace all the data points. The absolute magnitude, or the so-called nuisance parameter $\mathcal{M}$, is treated as an undetermined parameter in our analysis.

5.3 Fisher information analysis

To estimate how accurately one can constrain a set of model parameters let us consider the *Fisher information matrix*, defined as

$$F_{ij} \equiv \left\langle \frac{\partial^2 \mathcal{L}}{\partial\theta_i \partial\theta_j,} \right\rangle \tag{5.4}$$

where $\mathcal{L} \equiv -\ln L$ with $L(\mathbf{P}, \mathbf{d})$ being the probability distribution function as a function of model parameters $(\mathbf{P})$ and data $(\mathbf{d})$. According to the *Cramer-Rao* theorem, for any unbiased estimators of the parameters [228, 229]

$$\Delta d_i \geq (F^{-1})_{ii}^{1/2}, \tag{5.5}$$

and that maximum likelihood estimator is the best unbiased estimator in the limit of large data set. The Cramer-Rao inequality puts a lower limit on the errors of the model parameters so that they can not be less than their corresponding component in the inverse of the Fisher matrix.

For zero-mean Gaussian-distributed observables, like the angular correlations C_ℓ^{XY}, the Fisher matrix is given by [230]

$$F_{ab} = f_{\mathrm{sky}} \sum_{\ell=\ell_{\mathrm{min}}}^{\ell_{\mathrm{max}}} \frac{2\ell+1}{2} \mathrm{Tr}\left(\frac{\partial \mathbf{C}_\ell}{\partial p_a} \tilde{\mathbf{C}}_\ell^{-1} \frac{\partial \mathbf{C}_\ell}{\partial p_b} \tilde{\mathbf{C}}_\ell^{-1} \right) , \tag{5.6}$$

where p_a is the a^{th} parameter of our model and $\tilde{\mathbf{C}}_\ell$ is the "observed" covariance matrix with elements $\tilde{C}_\ell^{XY}$ that include contributions from noise:

$$\tilde{\mathbf{C}}_\ell^{XY} = \mathbf{C}_\ell^{XY} + \mathbf{N}_\ell^{XY} . \tag{5.7}$$

Eq. (5.6) assumes that all fields $X(\hat{\mathbf{n}})$ are measured over contiguous regions covering a fraction f_{sky} of the sky. The value of the lowest multipole can be approximately inferred from $\ell_{\mathrm{min}} \approx \pi/(2 f_{\mathrm{sky}})$.

The noise matrix N_ℓ^{XY} includes the statistical noise as well as the expected systematic errors. Systematics are very difficult to predict, and are often ignored in forecasts. However, we consider two cases here – the case when N_ℓ^{XY} includes the statistical noise only, and the case when certain types of systematics are included. Following [25, 231], three sources of systematics are considered here for future tomographic surveys:

- *photo-z* errors: these errors arise due to uncertainties in the redshift measurements of observed object in the sky.

- *Point Spread Function* (PSF) measurement errors: these are errors arising from inferring the shape and geometry of an object from the signal received from CCD camera.

The details of the modeling of the systematic effects are presented in Appendix A and one can refer to [25, 231] for a detailed discussion.

For SNe Ia, the information matrix is

$$F_{ab}^{\mathrm{SN}} = \sum_i^N \frac{1}{\sigma(z_i)^2} \frac{\partial m(z_i)}{\partial p_a} \frac{\partial m(z_i)}{\partial p_b}. \tag{5.8}$$

where $m(z)$ is redshift-dependent magnitude in Eq. (1.59), the summation is over the redshift bins, and $\sigma(z_i) = 0.13$ (see 1.3.2 for details).

In Eq. (5.6) and (5.8), the derivatives are either calculated analytically or by numerically using finite differences. For example, when p^a is one of the MG pixels (μ^a or γ^a), an observable is calculated for μ^a and $\mu^a + \delta\mu^a$ and calculate the derivative as

$$\frac{\partial \mathbf{C}_\ell}{\partial \mu^a} \approx \frac{\mathbf{C}_\ell(\mu^a + \delta\mu^a) - \mathbf{C}_\ell(\mu^a)}{\delta\mu^a}. \tag{5.9}$$

5.4 PCA of MG functions

If we want to know how well a given combination of experiments will measure μ, for example, we consider the μ block of the covariance matrix, C_{ij}^μ. We have derived the covariance matrix by inverting the Fisher matrix and hence, we have already marginalized over other parameters. Since the individual pixels of μ are highly correlated, the covariance matrix will be non-diagonal, and the value of μ in any particular bin will be practically unconstrained. With PCA, we decorrelate the parameters and find their linear combinations that are best constrained by data:

$$\alpha_i = \sum_{j=1}^{m\times n} W^{\mu}_{ij}(\mu_j - \bar{\mu}_j) \ . \tag{5.10}$$

In practice, one finds that only a few of the α's are well constrained (i. e. their corresponding errors are small), while most are essentially unconstrained. This is the main benefit of performing a PCA – it takes a function with many (infinite) degrees of freedom and isolates their few uncorrelated linear combinations that can be constrained by a given experiment. μ_i (and similarly, γ_i) can be expressed as

$$\mu_i - \bar{\mu}_i = \sum_{j=1}^{m\times n} W^{\mu}_{ij}\alpha_j \ . \tag{5.11}$$

where i labels a point on the (z,k) grid, j label the eigenmode, W is the rotation matrix defined in Eq. (2.38) and $\bar{\mu}_i$ is the fiducial value. Thus, taking the continuous limit, and using $\bar{\mu} = 1$ as the fiducial value, we can formally rewrite this as

$$\mu(z,k) = 1 + \sum_j \alpha_j W^{\mu}_j(z,k) \ , \tag{5.12}$$

which is an expansion of μ into an orthogonal basis of eigenvectors $W^{\mu}_j(z,k)$. We can now rearrange the eigenvectors into a 2D form and plot them as surfaces in the (z,k) space. We will refer to these surfaces as the principal components (PC's) or *eigenmodes*; the shapes of the best constrained eigenmodes indicate the kind of features in μ that experiments are most likely to constrain. The regions in (z,k) where the best constrained eigenmodes peak indicate the *sweet spots*, i.e. the intervals in time and scale where a given experiment will be more sensitive to departures from ΛCDM. The number of nodes in the z and k directions indicate the degree of sensitivity of the surveys to the z- and k-dependence of μ. The same procedure can be repeated for the function $\gamma(a,k)$ by isolating and diagonalizing the γ block of the covariance matrix to determine the eigenvectors $W^{\gamma}(z,k)$ and the corresponding eigenvalues.

The procedure outlined above addresses the ability of data to constrain μ and γ separately. Namely, when deriving the eigenmodes and eignevalues of μ (γ) we marginalize over γ (μ). However, observations probe combinations of the potentials ϕ and ψ that depend on both μ and γ. This yields a degeneracy between μ and γ and, by marginalizing over one, we lose the information that is common to both functions. In addition to forecasting separate constraints on μ and γ, one may want to know how sensitive data is to any departure from the standard growth. Namely, we may want to answer a less ambitious, yet equally interesting, question of whether either of the two functions deviates from unity, without specifying which. For this purpose, we want to save the information common to both functions, which we previously lost by mutual marginalization. Hence, we consider the combined principal components of μ and γ. We follow the same procedure as before, except now we diagonalize the block of the covariance matrix containing the pixels of μ and γ. The components of the matrix that diagonalizes $C^{\mu\gamma}$ will be $W_{ij}^{\mu\gamma}$, where now $i, j = 1....2m \times n$; each eigenmode j consists now of a double series of pixels on the (k, z) grid, representing combined eigenmodes in the two sub-spaces.

In the remainder of this section we analyze the principal components (eigenmodes) of the functions μ and γ defined in Sec. 3.2.1 for the combination of large scale structure (WL and GC), CMB and SNe experiments detailed in Sec. 5.2.1. In particular, we want to investigate the effect of degeneracies with other cosmological parameters on the eigenmodes and eigenvalues of μ and γ. For this purpose, in Subsection 5.4.1, we start with the simplest case where only uncertainties in the pixelated functions μ and γ (referred to as "MG pixels") are considered, with all other parameters fixed to their fiducial values. The highest redshift pixels ($3 < z < 30$) of μ and γ are outside the range directly probed by the WL surveys. However, they do impact the observables: $\mu(z > 3, k)$ re-sets the amplitude of the growth at all lower redshifts, while $\gamma(z > 3, k)$ affects the ISW contribution to the CMB temperature anisotropy. The sensitivity of observables to variations in $\mu(z > 3, k)$ and $\gamma(z > 3, k)$ depends on the assumed high-z cutoff – making the high-z interval wider increases the sensitivity. Thus below we focus on quantities that are independent of this cutoff, such as the eigenmodes and eigenvalues of μ and γ obtained after marginalizing over the high-z MG pixels, as well as the uncertainty in the overall growth between recombination and $z = 3$, which is directly controlled by $\mu(z > 3, k)$, but is independent of the choice of the high-z cutoff (see 5.4.4). In 5.4.2, we discuss effects of marginalizing over the high-z pixels and galaxy bias parameters. In (5.4.3), we consider degeneracies with the basic parameters

$\{\Omega_b h^2, \Omega_c h^2, h, \tau, n_s, A_s\}$ and the effective equation of state $w(z)$. Throughout this section, we always marginalize over the SNe nuisance parameter. To gain additional insight, we also project our findings onto the function Σ.

We examine the parameter degeneracies using LSST as the fiducial survey for WL and GC. Then, in 5.4.5, we compare the final case, in which we marginalize over all the parameters except the μ and γ in the range $0 < z < 3$, to the analogous forecast for DES.

5.4.1 PCA for LSST with all parameters, except MG pixels, fixed (high-z information included)

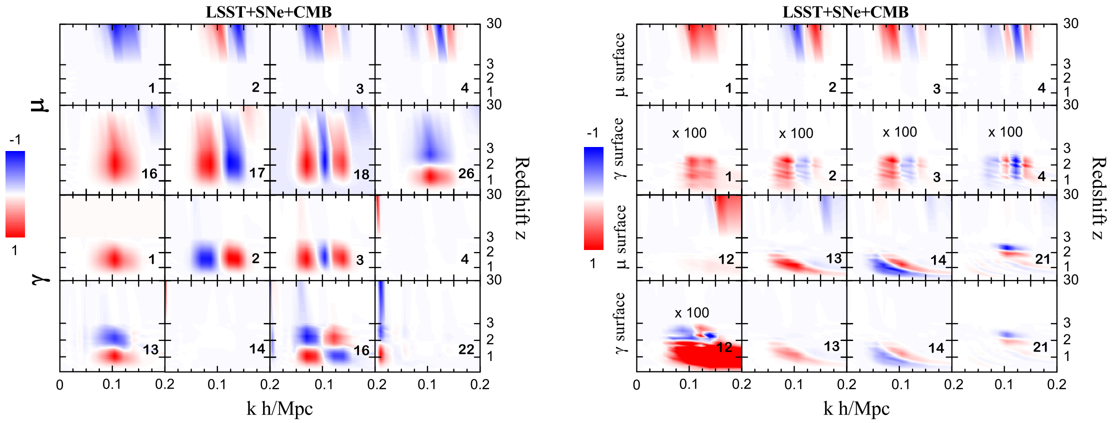

(a) μ and γ

(b) *combined*

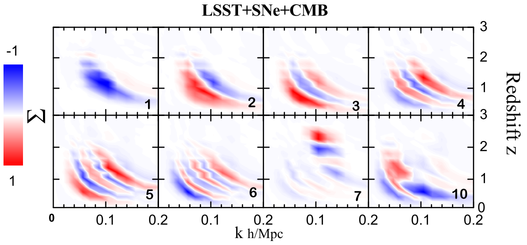

(c) Σ

Figure 5.1: The eigenmodes for LSST(+SN+CMB) with all other parameters fixed to fiducial values.

As a first step, we study the eigenmodes and associated uncertainties of the MG functions without considering their covariance with other parameters. We do this by isolating

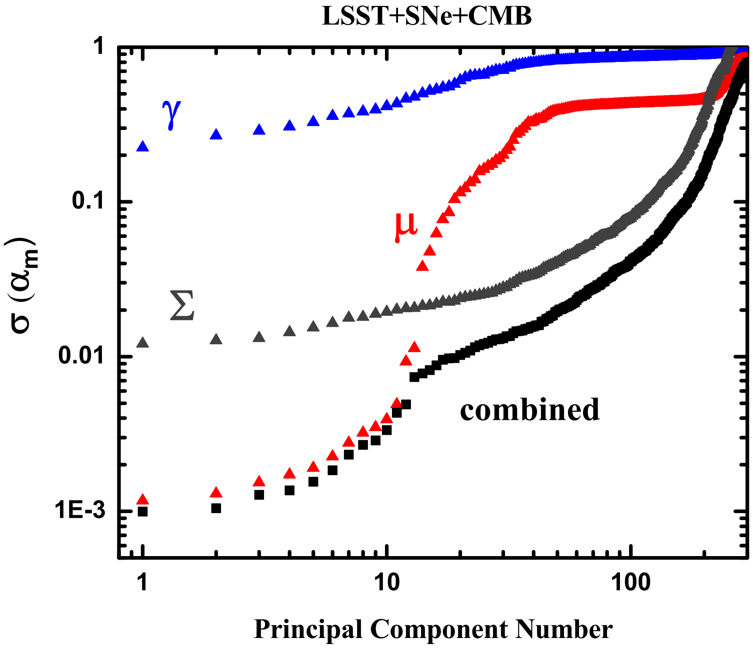

Figure 5.2: The uncertainties (square roots of covariance eignevalues) associated with the eigenmodes of μ, γ, Σ and the combined (μ,γ) case for LSST(+SN+CMB) with all other parameters fixed to fiducial values.

and inverting the block of the Fisher matrix containing only MG pixels (including the high-z bins) and diagonalizing the resulting covariance matrix.

Fig. 5.1(a) shows some of the eigenmodes of μ and γ. Each panel in these plots represents a region in (z,k) space with an eigenmode function plotted as a surface. We order, and consequently number, the eigenmodes according to how well they can be constrained, *i.e.* following the ordering of the corresponding errors (square root of the covariance matrix eigenvalues) from the smallest (best constrained) to the largest (least constrained).

The first feature to notice is in the μ eigenmodes (top two rows in Fig. 5.1(a)), where the best constrained modes peak at high-z, and show no features at low z; we need to get to the 16th mode to start seeing some features in the $z < 3$ interval, which is the actual redshift range of LSST. This is because μ directly affects the growth of matter density perturbations, and changing the amplitude of perturbations at some redshift affects the growth at lower redshifts. As we discuss in 5.4.4, the constraint on μ at $z > 3$ depends strongly on the width of the bin, i.e. the value of the arbitrarily chosen high-z cutoff. It is also highly correlated with μ in lower redshift bins and some of the vanilla cosmological parameters.

Unlike μ, the best constrained modes of γ do not have a support at high z. They peak at low redshifts (bottom two rows in Fig. 5.1(a)). This follows from the fact that, according to our definition, to measure γ one needs to measure both ϕ and ψ. Therefore, bounds on γ come mostly from combining the GC data, which probes ψ (affected by μ), with the WL signal probing $(\phi+\psi)$ (affected by both μ and γ). One can also see that there are modes that peak at $z > 3$ and at low k (very large scales). This is mainly due to the ISW effect, seen as a contribution to the CMB temperature spectrum, which is sensitive to the time variation of both potentials at all times after the last-scattering.

An important thing to notice is that the best constrained modes of μ and γ show oscillations (nodes) in k, but no nodes in the z-direction. One has to look at the higher number modes to start seeing oscillations in z. For instance, for μ, the first z-node appears in the 26th eigenmode. The number of nodes is indicative of the sensitivity of the function to changes in k and z, and we see that the experiments are significantly more sensitive to scale-dependent features of the MG functions, and not as sensitive to the time-dependence. This is expected, since the impact of a scale-dependent change in μ (or γ) is directly translated into a scale-dependent feature in the WL and GC spectra. For instance, in the case of GC, μ effectively appears as a scale-dependent normalization factor. On the other hand, the projection of time-dependent features of the MG functions onto the observables involves integration over time which makes detecting z-dependent features harder. Also, the amount of information coming from the radial (z-direction) is limited by the fact that LSST only probes structures at $z \lesssim 3$, and by the fact that we consider only linear scales, effectively cutting off a significant volume at low z.

Fig. 5.1(b) shows the best *combined* eigenmodes of (μ,γ). Every combined eigenmode is represented by a pair of values at each point on the (k,z) grid, one value resulting from a variation of μ on that grid point and the other from a variation of γ on the same grid point. We show each eigenmode as a pair of surfaces, one corresponding to μ and the other to γ. It can be noticed that the best constrained modes peak at high redshift, which is the result of high sensitivity of the growth to changes in μ in the high-z bins. Since γ does not directly affect the growth rate, the γ surfaces of these eigenmodes have a very low amplitude, requiring us to amplify them by a factor of 100 in order to make them visible in the plots. The combined eigenmodes that peak at low redshifts, starting from the 13th, do not exhibit separation of scale or time dependent oscillations, but rather have a diagonal form in the (z,k) space, showing a degeneracy between scale and time. This is because the WL observables dominate the information for combined modes at low redshift. Indeed, the changes in the weak lensing kernel due to a shift of the lens along the line of sight (*i.e.* a change in redshift) are degenerate with those due to a resizing of the lens (*i.e.* a change in scale).

Fig. 5.1(c) shows the best eigenmodes for the function Σ. As it is clear from its definition (4.13), Σ is directly sensitive to the lensing potential $(\phi+\psi)$; therefore its signal comes mainly from low redshifts and it does not have well constrained high redshift modes. For this reason the plots for Σ span only over the low redshift interval. From these plots we notice a $k-z$ degeneracy analogous to the one found in the combined (μ,γ) modes as it is clear from a comparison of Fig. 5.1(b) and Fig. 5.1(c).

Finally, Fig. 5.2 shows the uncertainties (square roots of covariance eigenvalues) associated with the eigenmodes of μ, γ, Σ and the combined modes. As expected, the combined eigenmodes are constrained best, since they contain all of the information about any departure of either μ or γ from unity. The constraints on γ are the weakest, since γ is not directly constrained by WL nor GC, while μ does better than γ since it is directly constrained by GC. The eigenmodes of μ that peak at $z>3$ are constrained better than those of Σ, while Σ is measured better than μ for modes with support at lower redshifts. This is because at low redshifts most of the information comes from WL, which is directly sensitive to Σ. As mentioned earlier, the bounds on the $z>3$ bin of μ are dependent on the arbitrary cutoff and in the next subsection we will marginalize over it.

5.4.2 PCA for LSST after marginalizing over high z and galaxy bias, everything else is fixed

In order to remove the dependence of our results on the arbitrary choice of the upper cutoff of the high-z bins ($3<z<30$), we marginalize over the high-z pixels. This is achieved by removing the rows and columns corresponding to high-z pixels from the covariance matrix of the previous subsection, and then diagonalizing it to find the eigenmodes and

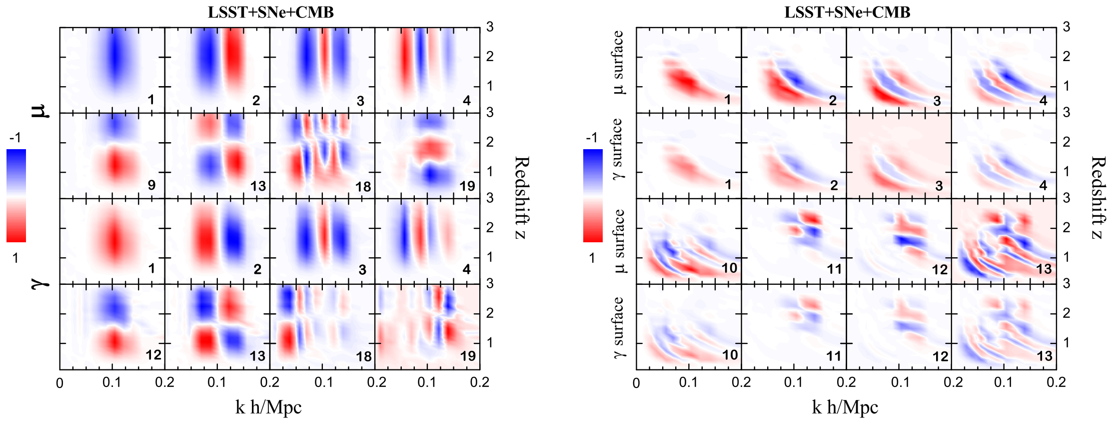

(a) μ and γ

(b) *combined*

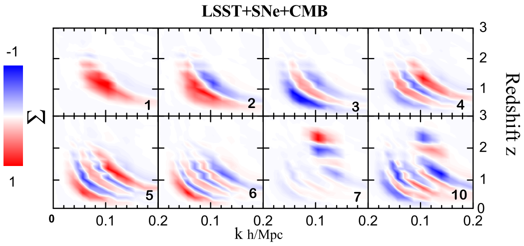

(c) Σ

Figure 5.3: The eigenmodes for LSST(+SN+CMB) after marginalizing over the high-z bins, with all other parameters fixed to fiducial values.

eigenvalues. This essentially removes all the information about the growth at $z > 3$ and, with that, all the $z > 3$ features in the eigenmodes. This is seen in Figs. 5.3(a)-5.3(c), where the eigenmodes for μ, γ, the combined (μ, γ) and Σ are shown for this case.

From Fig. 5.3(a) we notice that, in the absence of the high-z information, the first few best constrained eigenmodes of μ and γ have similar shapes. However, this similarity fades for the higher order eigenmodes, reflecting the different dependences of the two functions on the metric potentials. For instance, the first node in z appears at the 9th mode for μ and only at the 12th for γ, reflecting a higher sensitivity of μ to time dependent features.

The best constrained combined (μ, γ) eigenmodes have the same shapes in the μ- and γ-surfaces, but the γ-surfaces have a lower amplitude (Fig. 5.3(b)). This is again explained by the fact that both functions are constrained by the same experiments (WL and GC), therefore having similar eigenmodes, with μ being more directly related to the growth of

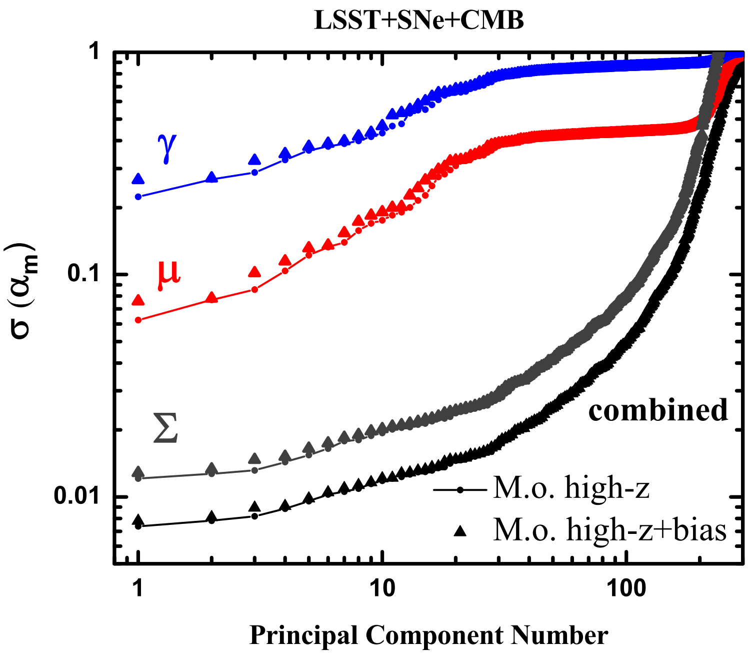

Figure 5.4: The uncertainties associated with the eigenmodes of μ, γ, Σ and the combined (μ, γ) modes for LSST(+SN+CMB), after marginalizing over the high-z bins only (M.o. high-z), and after marginalization over the high-z bins and the galaxy bias parameters (M.o. high-z+bias), with all other parameters fixed to fiducial values.

structure.

As can be observed from Fig. 5.3(c), after marginalizing over the high-z bins, the best eigenmodes of Σ are very similar to the combined (μ, γ) modes. Indeed, once the high-z information is removed, the combined modes are primarily constrained by WL and, therefore, carry more or less the same information as the Σ modes.

Fig. 5.4 shows the uncertainties associated with the eigenmodes of μ, γ, Σ and the combined (μ, γ) modes after marginalizing over the high-z bins. Comparing to Fig. 5.2, we see that now there is no crossing over of the errors on μ and Σ, *i.e.* all the PCs of Σ do better than the μ ones. This is due to the disappearance of the eigenmodes with high-z support. In addition, we notice a small overall degradation of constraints, which is due to throwing away the information common with the low-z bins.

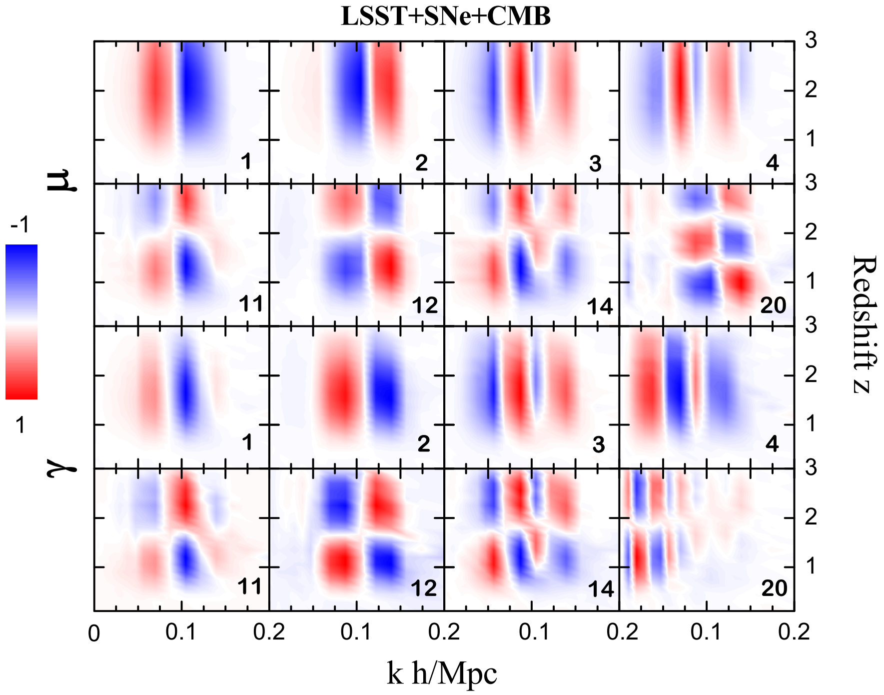

Figure 5.5: The eigenmodes of μ and γ for LSST(+SN+CMB), after marginalizing over the high-z bins and the galaxy bias parameters, with all other parameters fixed to fiducial values.

Next, we marginalize over the galaxy bias parameters. This is achieved by inverting the part of the Fisher matrix that includes the MG pixels and the bias parameters. This effectively removes the information about the overall normalization of μ. This is manifested in the disappearance of some of the eigenmodes, including the homogeneous eigenmodes, e.g. present in Fig. 5.3(a) but not in Fig. 5.5. The same happens to the eigenmodes of Σ and of the combination (μ, γ) and we do not plot them.

5.4.3 PCA for LSST after marginalizing over the vanilla cosmological parameters and $w(z)$.

We now marginalize over the cosmological parameters: $\{\Omega_c h^2, \Omega_b h^2, h, \tau, n_s, A_s\}$ and the binned values of $w(z)$. By doing so we account for the covariance of MG pixels with the vanilla ΛCDM parameters and the effective dark energy equation of state. Figs. 5.6(a)-5.7

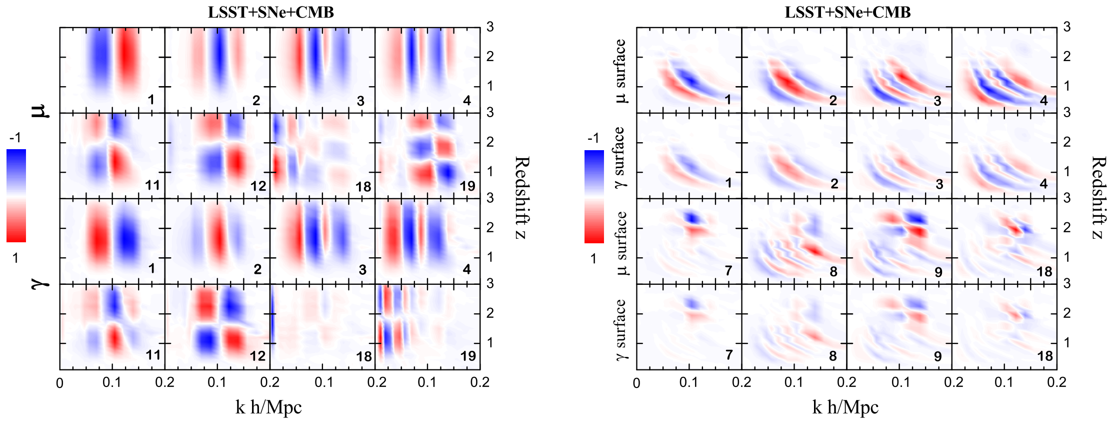

(a) μ and γ

(b) *combined*

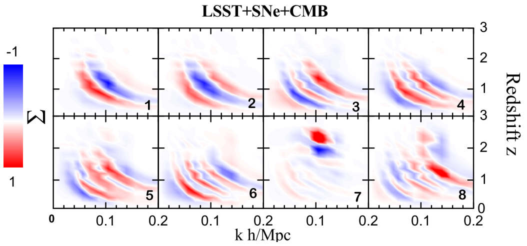

(c) Σ

Figure 5.6: The eigenmodes for LSST(+SN+CMB) after marginalizing over all other parameters.

show the PCA results for this case.

The impact of marginalizing over $w(z)$, as opposed to setting it to $w = -1$, is not dramatic and we do not separately show the eigenmodes for the latter case. The associated eignevalues, plotted in Fig.5.7, show only a minor differences. This is, in part, due to the high quality of the assumed SNe dataset (see Sec. 5.2.1). However, it is also because of marginalizing over the vanilla parameters, the galaxy bias parameters and the high-z bins, which already throws away most of the information that is common between the MG pixels and $w(z)$. The effect of marginalizing over bias parameters and w bins is minor changes in the shape of modes (e.g. second mode in Fig. 5.6(a) to be compared with second mode in Fig. 5.5), disappearance of some of the modes and an overall degradation of constraints.

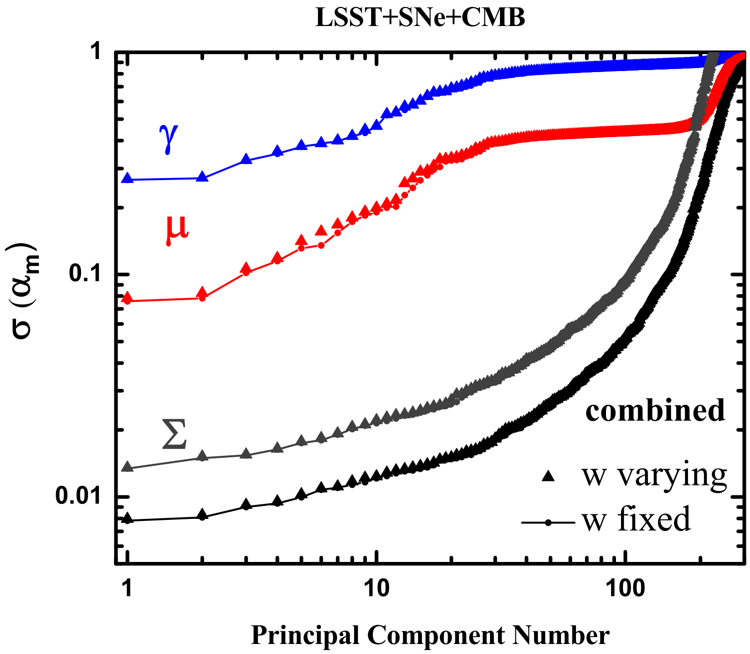

Figure 5.7: The uncertainties associated with the eigenmodes of μ, γ, Σ and the combined (μ,γ) modes for LSST+SN+CMB after marginalizing over all other parameters. Two cases are shown: with w bins fixed to their fiducial value of -1 (dots joined by lines), and with w bins varied and marginalized over (triangles).

5.4.4 Constraints on the growth at high redshift

The growth at $z > 3$ is not directly probed by the large scale structure surveys considered here. Any modification to growth at $z > 3$, such as due to variations of high-z MG pixels, is observed as an overall shift of the amplitude of the growth at all subsequent (i.e. lower) redshifts. This can, in principle, be compensated by counter-variations of the low-z MG pixels. However, we find that bounds on high-z pixels are still relatively tight (at a percent level), even after marginalizing over the low-z bins. Such tight constraints are due to the large width of high-z pixels. Namely, a small change in value of μ in the high-z bins results in an accumulated modification of growth that can only be compensated by a very large variation of the low-z pixels. On the other hand, the low-z pixels are directly constrained by the surveys and large variations are not allowed. Of course, one can always make the bounds on the high-z bins arbitrarily weak by making the bins narrower.

Since the width of high-z pixels is a somewhat arbitrary parameter, one can ask if another quantity can be introduced to quantify the growth at $z = 3$. We take this quantity to be the ratio $r(k)$, defined as:

$$r(k) \equiv \frac{\Delta(z=3,k)}{\Delta(z_{\rm rec},k)}\,, \tag{5.13}$$

where Δ is defined in Eq. (3.33) and $z_{\rm rec}$ denotes the redshift at recombination. We can estimate the variance in r ($C_{rr} = \sqrt{\sigma_r^2}$) from

$$\sigma_r = \sum_i \frac{\partial r}{\partial p_i}\sigma_{p_i}\,, \tag{5.14}$$

where p_i's are all the parameters of our model that affect r. Our calculation shows that $\sigma_r/r > 1$ for all k. In other words, r is completely unbounded, as expected. Note that the calculation would need to be adjusted for DES, for which the highest redshift is $z = 1.3$, instead of $z = 3$.

5.4.5 Comparison with DES

To get a further insight into how the MG constraints depend on the properties of the experiments, we compare PCA for LSST+CMB+SNe with that for DES+CMB+SN. That is, we interchange LSST with DES for the WL and GC data, while keeping the assumptions for the CMB and SNe data the same. We perform this comparison only for the case in which we marginalize over all parameters, *i.e.* high-z bins, bias parameters, cosmological vanilla parameters and $w(z)$, as in 5.4.3.

Figs. 5.8(a) and 5.8(b) show the eigenmodes of μ, γ and (μ,γ) for DES+CMB+SN. These results should be compared to Figs. 5.6(a) and 5.6(b) for LSST. We choose to show a smaller number of eigenmodes, since there are not as many well constrained modes for DES as there are for LSST.

As can be seen from Figs. 5.8(a) and 5.8(b), the range over which the eigenmodes vary is limited to smaller redshifts ($z < 1$), which reflects the redshift range probed by DES. Like in the case of LSST, there is a higher sensitivity to scale-dependent features. Furthermore, in the case of DES, there are modes with oscillations in z. Some of the combined eigen-

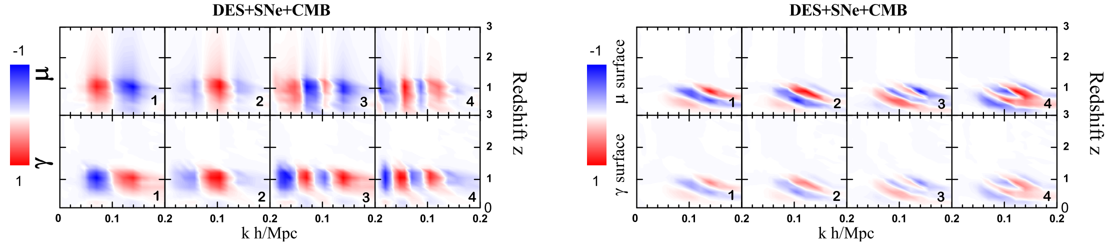

(a) μ and γ

(b) *combined*

Figure 5.8: The eigenmodes for DES+SNe+CMB after marginalizing over all other parameters.

modes are also absent for DES . Fig. 5.9 shows a comparison of the uncertainties associated with the modes for LSST and DES.

While the overall sensitivity of DES is less than LSST by a factor of few, DES, when combined with CMB and SNe data, is still able to constrain several eigenmodes with better than 10% accuracy. We may not be able to detect a time-dependent MG feature with high confidence from DES, but it is possible to constrain scale-dependent features.

5.5 Effects of systematic errors

Systematics are notoriously hard to predict, and forecast results that include systematics are in general sensitive to the modeling and the assumed priors [231, 25, 26, 27]. Here we consider some of the systematics that will affect future tomographic surveys and study their impact on our PCA results. This can give us a general insight on how systematic errors could affect our inferences of the eigenmodes and the corresponding uncertainties. The systematics we consider here are the photo-z errors and some of the errors in the measurement of the point spread function (PSF). These errors are modeled in [25, 231] and we use their parametrization for our Fisher analysis.

The effects of the systematics are detailed in the Appendix, and with these assumptions we study the degradation of ability of DES and LSST to constrain MG by marginalizing over the systematics parameters without applying any prior. As we show later, the degradation is apparent, but not disastrous. It is true that the catastrophic photo-z errors (CPE) for WL surveys [232] can lead to disastrous degradation on the constraints of the cosmological

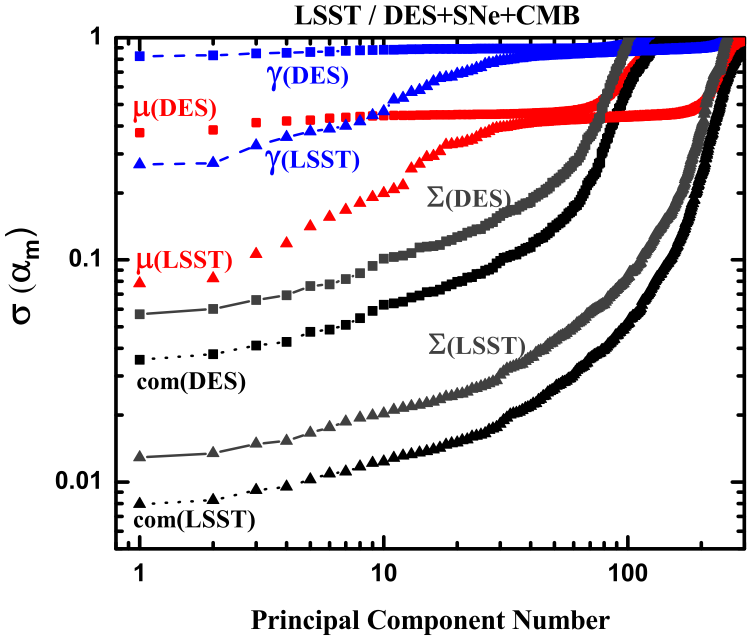

Figure 5.9: The uncertainties associated with the eigemodes of μ, γ, Σ and combined (μ, γ) modes for DES(+SN+CMB) and for LSST(+SN+CMB) errors, after marginalization over all other parameters.

parameters, but as shown in [232], an additional 30,000 spectroscopic redshifts can help to control the bias in cosmological parameters due to CPE under the level of statistical errors. The most significant effect is to reduce the ability of LSST to detect the z-dependence of μ. This is a preliminary analysis, which does not include scale-dependent systematics, which can be particularly important in MG studies (as was found in [233] where PCA was applied to a set of existing data including CFHTLS).

Let us look at the errors for combined eigenmodes shown in Fig. 5.10(a) for the following cases: (I) no systematics, with w fixed; (II) no systematics, with w varied; (III) with systematics, and w fixed; (IV) with systematics, and w varied. We can see that allowing for systematics degrades the constraints more than allowing for variations in w. Also, once the systematic errors are included, allowing w to vary does not degrade the constraint further. This means that the MG pixels are more degenerate with the systematics parameters

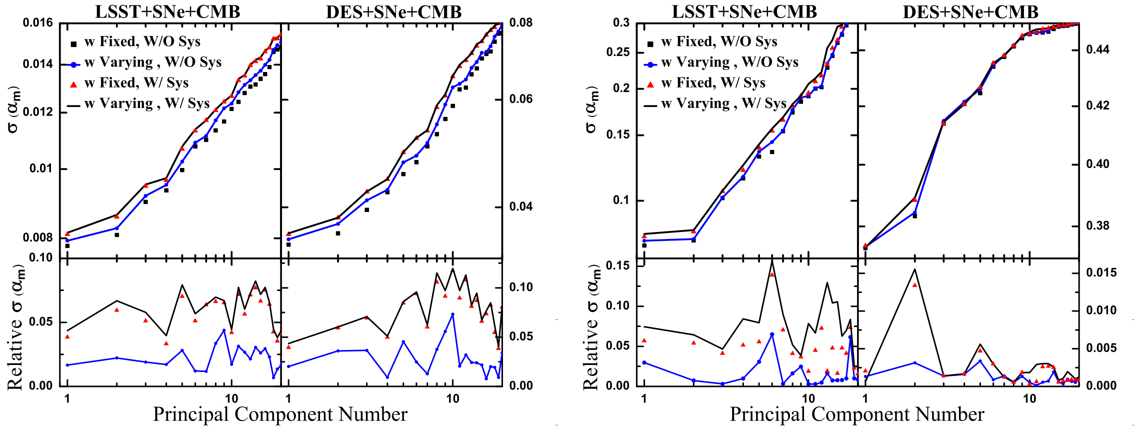

(a) *combined* (b) μ

Figure 5.10: Top: The uncertainties associated with the eigenmodes for LSST (left) and DES (right) for four cases: (I) without systematics and w fixed, (II) without systematics but w varied, (III) with systematics but w fixed and (IV) with systematics and w varied. Bottom: The uncertainties for LSST (left) and DES (right) relative to Case I.

than the w bins, implying that the uncertainty in the galaxy distributions, which is basically photo-z error from the systematics, can affect the constraint on the growth more significantly than w does. In general, the errors on the best constrained modes are degraded by $\lesssim 10\%$ for both LSST and DES. Another interesting observation is that the largest degradation does not happen for the first few modes, but for the intermediate modes. This is reasonable – the first few modes do not have nodes in z and thus are relatively immune to the systematics dominated by the photo-z errors.

We have shown the errors on the eigenmodes for μ in Fig. 5.10(b) where the same cases as above are considered. One notices that degradation on μ is less than what we had for combined case, especially no significant changes for DES are found. For γ, degradation is very small simply because the constraints on γ eigenmodes are very weak in the first place. We are not therefore showing γ errors here.

Another observation is that systematics can create new, or destroy existing modes, so that the modes with the same order in the PCA sequence in the cases with and without systematics can be different modes. One can see this clearly by looking at the eigensurfaces in Fig. 5.11, where we illustrate the three μ modes and one γ mode with and without systematics. They look similar except that the modes with systematics in general have more nodes

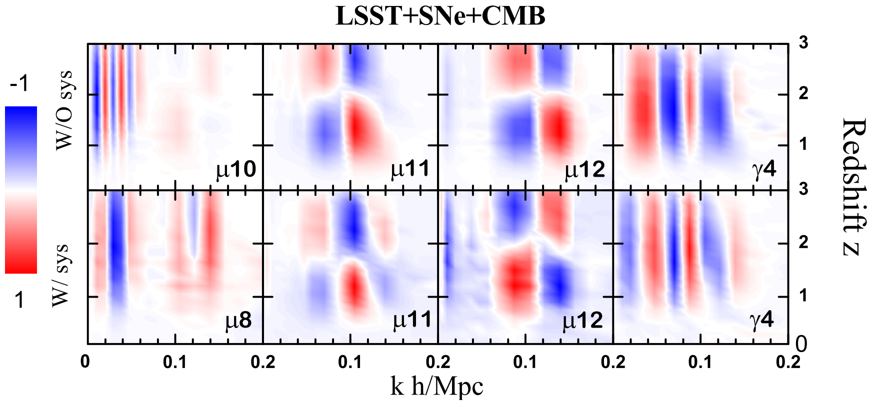

Figure 5.11: The eigenmodes for LSST(+SN+CMB). The upper(lower) panel corresponds to the case without(with) systematics. The 10th, 11th and 12th modes of μ without systematics, are compared to the 8th, 11th and 12th modes of μ with systematics respectively. These modes are chosen since they correspond to the last z-independent and first z-dependent mode respectively, in the two case (with and without systematics). Analogously, the 4th eigenmode of γ without systematics is compared to the 4th mode of γ with systematics. It is an illustration of how LSST eigenmodes are distorted as a result of accounting for systematics.

in k, indicating that systematics do not just dilute the constraints on the old modes, but also make some modes disappear (or make them very poorly constrained). The general trend is that eigenmodes with very high frequency features in k are no longer well-constrained after inclusion of systematics.

Overall, we find that the inclusion of systematics results in a noticeable, but not dramatic, dilution of the constraints on MG from DES. This is because photo-z errors would most immediately affect the z-dependence of MG, to which DES was already mostly insensitive even without systematics. The main constraints from DES, as can be seen from the shape of the eigenmodes (Fig. 5.12), will be on the scale-dependence of μ and γ, and that information is somewhat reduced, but mostly preserved. The impact of the systematics on LSST could be more significant, simply because LSST has a higher potential for resolving z-dependent features. In this preliminary analysis, we find that allowing for systematic errors under the assumptions of [25, 231] preserves most of the scale-dependent information from LSST, but decreases our ability to measure eigenmodes of μ with z-dependent

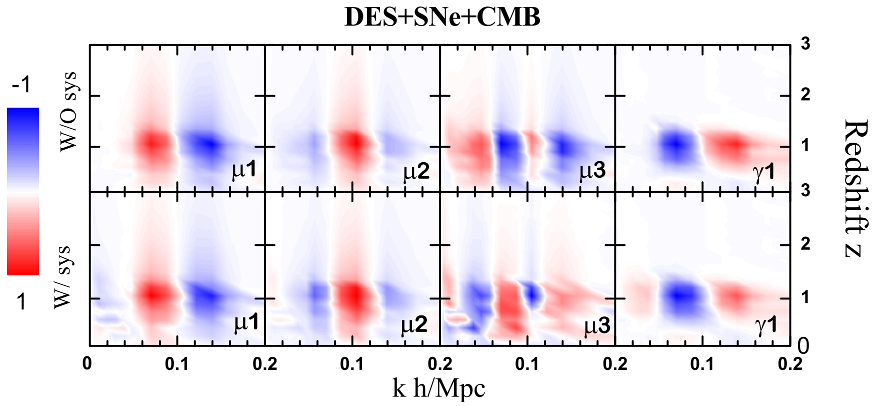

Figure 5.12: The eigenmodes for DES(+SN+CMB). The upper(lower) panel corresponds to the case without(with) systematics. The three modes of μ and first mode of γ without systematics, are compared to corresponding modes of μ with systematics. It is an illustration of how DES eigenmodes would be distorted due to systematics.

features.

5.6 Degeneracy between MG parameters and dark energy EoS

In Sec. 5.4.3, we marginalized over the binned equation of state and analyzed the impact of this marginalization on the eigenmodes of μ and γ. Here we investigate how marginalizing over MG pixels affects the eigenmodes and eigenvalues of $w(z)$. In this case, we diagonalize the block of the covariance matrix containing the 21 w-bins. Fig. 5.13 (top) shows the best three eigenmodes of w in the case when μ and γ pixels are co-varied, and when they are fixed to their fiducial values.

The most noticeable effect of the marginalization is a reduction of the amplitude of the best constrained modes at higher z. In other words, letting MG parameters vary squeezes the best constrained eigenmodes of $w(z)$ towards low redshift. This is expected, since most of the information on $w(z)$ comes from the SNe and from the probes of LSS at higher redshift. The latter is largely degenerate with MG, and so the high-z information on $w(z)$ is erased. On the other hand, LSS does not contribute much to the low-z information, since

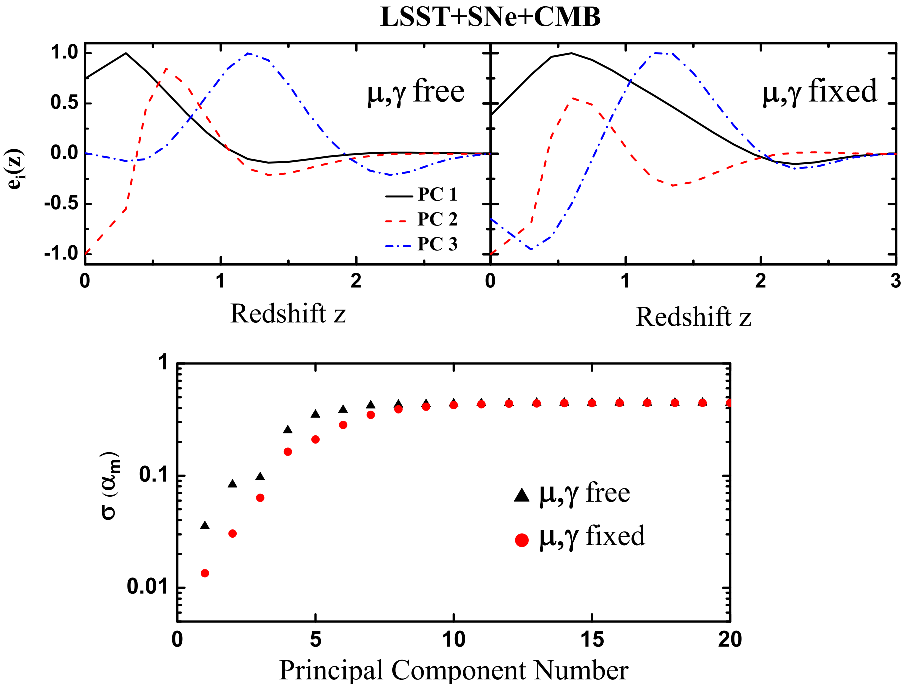

Figure 5.13: Top: First three eigenmodes of $w(z)$ with (left) and without (right) MG included. Bottom: Errors for $w(z)$ eigenmodes with and without MG included (there is a prior of 0.5 on w bins).

we restrict to modes in the linear regime, therefore the marginalization has little impact on the low-redshift parts of the $w(z)$ modes.

Overall the effects of the marginalization over the MG functions are not dramatic and future surveys will have the ability to measure both w and MG. Fig. 5.13 (bottom) shows the degradation of errors on the w eigenmodes after marginalizing over other parameters, including MG. Note that a prior of $\sigma_i = 0.5$ has been put on the bins of w.

5.7 Projected errors on parameters of specific models from principal components

MG pixels can be viewed as a compressed form for the information we get from observation about the linear growth. One can perform a PCA and store this information in the eigenmodes and their eigenvalues. The advantage of PCA is that the information can be compressed and used more efficiently, namely, the well-constrained eigenmodes usually carry almost all of the existing information.

Exploiting information stored in the eigenmodes, we can easily emulate any other parameterization to forecast parameter errors without regenerating the Fisher matrices from scratch [237]. In other words, we can treat MG pixels as our observables and use them to calculate the Fisher matrices for specific model parameters.

The Fisher matrix can be written as

$$F_{ab} = \sum_{\alpha\beta} \frac{\partial O_\alpha}{\partial p^a} C^{-1}_{\alpha\beta} \frac{\partial O_\beta}{\partial p^b} \,, \tag{5.15}$$

where O_α are cosmological observables and p^a are parameters of a specific model. This can be rewritten as

$$\begin{aligned} F_{ab} &= \sum_{ij} \frac{\partial \mathcal{P}_i}{\partial p^a} \left[\sum_{\alpha\beta} \frac{\partial O_\alpha}{\partial \mathcal{P}_i} C^{-1}_{\alpha\beta} \frac{\partial O_\beta}{\partial \mathcal{P}_j} \right] \frac{\partial \mathcal{P}_j}{\partial p^b} \,, \\ &= \sum_{ij} \frac{\partial \mathcal{P}_i}{\partial p^a} \, F_{ij} \, \frac{\partial \mathcal{P}_j}{\partial p^b} \end{aligned} \tag{5.16}$$

where $\mathcal{P}$'s are MG pixels and F_{ij} is the ij element of their Fisher matrix. All we need now is to expand the derivatives of the MG pixels with respect to a given parameter in the eigenmode basis. That is, for each of the new parameters, we find the coefficients $\mathcal{C}_l^a$ such that [1]

$$\frac{\partial \mathcal{P}_i}{\partial p^a} = \sum_l \mathcal{C}_l^a \, e_i^l \,, \tag{5.17}$$

where the sum is over all the eigenmodes and e_i^l is value of the lth eigenmode at the ith pixel of the 2D (k,z) grid. Substituting Eq. (5.17) in Eq. (5.16), we can then find the Fisher matrix for the parameters of our model by simple projection as

$$F_{ab} = \sum_i \mathcal{C}_i^a \, \mathcal{C}_i^b \, \lambda_i^{-1} \,, \tag{5.18}$$

where again the sum is over all the eigenmodes, and λ_i's are the corresponding eigenvalues of the covariance matrix for MG pixels.

We now illustrate the details of this method by applying it to a one-parameter model which gives a good approximation of $f(R)$ theories in the quasi-static limit [208] (and which is a customized form of the more general parametrization introduced in [41])

$$\begin{aligned} \mu(a,k) &= \frac{1}{1-1.4\cdot 10^{-8}\lambda^2 a^3} \frac{1+\frac{4}{3}\lambda^2 k^2 a^4}{1+\lambda^2 k^2 a^4}\,, \\ \gamma(a,k) &= \frac{1+\frac{2}{3}\lambda^2 k^2 a^4}{1+\frac{4}{3}\lambda^2 k^2 a^4}\,, \end{aligned} \tag{5.19}$$

where $\lambda^2 = B_0 c^2/(2H_0^2)$ and c is the speed of light. The parameter λ is the mass of the $f(R)$ scalar degree of freedom today. In [217, 234], a bound of $B_0 \lesssim 10^{-3}$ at 95% confidence level was found based on the current cluster abundance data, which extends to mildly non-linear scales.

Here, we forecast the constraints on B_0 from LSST, based only on linear scales, in two ways: using a direct Fisher matrix calculation and a Fisher matrix projection described above. We choose $B_0 = 0$, corresponding to GR, as the fiducial model. We use the same combination of future data for the direct Fisher matrix calculations as we did for the PCA

---

[1] Note that since we are working on a discrete (k,z) grid, our equations are in a discrete form. Analogous expressions could be written for the continuous case. For example, Eq. (5.17) for a continuous μ function would be $\frac{\partial \mu(a,k)}{\partial p^a} = \sum_l \mathcal{C}_{\mu,l}^a \, e_l^\mu(a,k)$.

DES		LSST	
Direct	Projection	Direct	Projection
$1.5 \cdot 10^{-6}$	$2.5 \cdot 10^{-6}$	$3.1 \cdot 10^{-7}$	$2.4 \cdot 10^{-7}$

Table 5.1: Error forecasts for the B_0 parameter for DES and LSST in combination with CMB and SNe data.The results for Fisher matrix projection formalism used here is compared to the direct Fisher matrix calculation.

of MG, and use the eigenmodes and eigenvalues of Section 5.4.3 for the Fisher matrix projection. The derivatives on the left hand side of Eq. (5.17) can be calculated analytically from Eq. (5.19). Since we are working on a 2D grid of k and a, we use the averaged value of these derivative expressions over each pixel and compute the expansion coefficients of eq. (5.17) numerically. Table 5.1 shows the forecasted constraints on B_0 from LSST and DES combination data obtained using the two methods. The results show a reasonable agreement.

One should be careful when working with projection method. For example, the priors used for calculating the covariance matrix for MG pixels (C_{ij} in eq. (5.16)) should be the same as the priors that would be used for a direct fisher analysis for a model. Ideally, the fiducial models should also be the same in both approaches.

As mentioned before, one of the advantages of the PCA approach is that we are able to compress information using only the best principal components. We find that in order to reproduce the errors shown in the "Projection" columns of Table 5.1 at about 95% precision we only need $\sim 25\%$ of the eigenmodes. Such compression of information can be useful, given the increasing volume of cosmological data.

5.8 Summary

The number of well-constrained eigenmodes gives a forecast of how many degrees of freedom describing deviations from GR will be constrained, and is particularly informative when comparing the outcome for different surveys. The shapes of the eigensurfaces indicate the regions of scale and redshift where the surveys under consideration will be most sensitive to departures from GR.

In Section 5.4, a detailed presentation of the eigenmodes and eigenvalues of the functions μ, γ, Σ as well as of the combination (μ,γ) was given, comparing them and interpreting the differences. Degeneracy between the MG functions and other cosmological parameters was also studied by progressively varying and marginalizing over the different parameters. Of particular interest was the analysis of the degeneracy with the equation of state. We saw that after marginalizing over the MG functions, the high-z information on $w(z)$ is erased and its best constrained eigenmodes are squeezed towards low redshift; however, the effects of the marginalization are not dramatic and future surveys will have the ability to constrain both w and modified growth. From the comparison of the results for LSST and DES, in Sec. 5.4.5, we notice that LSST will have overall a higher sensitivity to modified growth and will be more sensitive to time-dependent features. In Sec. 5.5, we studied the effects of WL systematics for LSST, and found that the degradation of constraints on MG is not significant, at least of the systematics models we have considered, and especially after one marginalizes over an arbitrary $w(z)$.

Finally, the utility of the PCA approach as a data compression formalism was illustrated. One can store the information contained in observables in terms of the MG pixels, or the eigenmodes of two functions. One can later use this information to project on to constraints on the parameters of specific models. For example, in Sec. 5.7, the errors on the MG functions were projected to forecast the error in B_0 and we saw that only a fraction of the total number of eigenmodes is needed to obtain this constraint.

Chapter 6

Degeneracies between MG and other parameters

The impact of modification to gravity on the cosmological observables is partially degenerate with other physical effects. One of the goals of taking a phenomenological approach of parametrizing the field equations is to detect possible deviations of (linear) perturbations from their default evolution efficiently and model-independently. However, degeneracies existing between the MG and other model parameters would limit our ability to do so. Therefore, it would be interesting to study how degenerate the parameters of different MG parametrizations are with the main cosmological parameters. One can investigate the scales and redshifts where these degeneracies are minimum, how different observables can break these degeneracies, and what combinations of data do it best. This can help us to come up with an optimum set of parameters for extracting information about a model and constraining the MG parameters.

To study the degeneracies, in this chapter, we consider some of the widely used parametric forms of the MG functions introduced in Chapters 3-5. In addition, we also consider the pixelization scheme of (μ,γ) as a less model-dependent treatment of the functions. With the pixels of μ and γ, one is able to study the degeneracies at particular redshifts and scales of interest.

There are different physical processes that lead to degenerate effects with modified gravity on the cosmological observables. For example, in Section 4.4, it was explained how massive neutrinos modify the growth of structure in a way that can be degenerate

Parameter description	I	II	III	IV
$\Omega_b h^2$, baryon density	1	1	1	1
$\Omega_c h^2$, cold dark matter density	2	2	2	2
H_0, Hubble constant today	3	3	3	3
τ, optical depth	4	4	4	4
n_s, scalar spectral index	5	5	5	5
w_i ,effective DE equation of state	6	6	6	6-7
MG, MG parameters in each model	7	7-9	7-11	8-19
A_s, amplitude of scalar perturbations	8	10	12	20
b_i, bias parameters for 10 GC tomographic redshift bins	9-18	11-20	13-22	21-30

Table 6.1: List of the parameters included in our models (I - IV), with the numbers showing the order of their appearance in each model.

with a modification to gravity. With the new generation of large scale structure surveys, these additional effects have non-negligible contribution and their degeneracies should be considered when searching for hints of modified growth. Also, as we saw in Section 5.5, the WL systematics can change the constraints on the MG functions. It would be important to investigate how the degeneracies change when including the systematics.

6.1 Models

We choose to work with four models which include one, three, five and twelve MG parameters, respectively. Table 6.1 shows the model parameters that we use in our Fisher analysis and the order in which they are sorted. In all of the models, we include the main cosmological parameters (#1-5 and A_s). When GC data is included, we assume that the bias is scale-independent on the linear scales and introduce 10 constant bias parameters, one for each photometric redshift bin surveyed by LSST. $w(z)$ is either binned or considered as a constant and is included in the Fisher analysis [1].

1-parameter MG model: f(R) theory

We consider the BZ parametrization of f(R) theories, Eq. (6.1), as our 1-parameter model. Here, the MG parameter is the squared Compton wavelength of the scalar field today, B_0

---

[1] We include the SNe Ia nuisance parameter in all these models and then marginalize over it.

from Eq. (4.36). We choose a fiducial value of $B_0 \sim 10^{-6}$ in accordance with the forecasted error on this parameter from LSST [47]. For this value of B_0, the pre-factor in Eq. (6.1) is negligible and we have

$$\mu(k,a) = \frac{1+\frac{4}{3}B_0 C}{1+B_0 C} \qquad \gamma(a,k) = \frac{1+\frac{2}{3}B_0 C}{1+\frac{4}{3}B_0 C}, \tag{6.1}$$

where $C \equiv (cka^2)^2/2H_0^2$.

3-parameter MG model: scalar-tensor theory

We choose the (μ,Σ) combination, described in Section 3.2.2, with the following parametric form

$$\begin{aligned} \mu &= 1+\frac{ca^s(k/H_0)^n}{1+3ca^s(k/H_0)^n}, \\ \Sigma &= 1, \end{aligned} \tag{6.2}$$

where c, n and s are constants. This choice of (μ,Σ) can cover a wide range of scalar-tensor theories [238]. It is easy to show that Eqs. (6.2) can be described in terms of (μ,γ) as

$$\mu = 1+\frac{ca^s(k/H_0)^n}{1+3ca^s(k/H_0)^n}, \quad \gamma \equiv \frac{2}{\mu}-1 = 1-\frac{6ca^s(k/H_0)^n}{1+ca^s(k/H_0)^n}. \tag{6.3}$$

defining $3c/H_0^2 \equiv \lambda^2$, we get back the BZ parametrization, Eq. (4.35). We work with the fiducial values of $s = 4$ and $n = 2$ and $c = 0.002$. The value for c is taken from the 95% C.L. constraints on the parameter from the current large scale structure data [238].

5-parameter MG model: a general BZ parametrization

The BZ parametrization with five independent parameters, $\beta_1, \beta_2, \lambda_1, \lambda_2$ and s in Eq. (4.35), provides more flexibility in capturing modified gravity features. We choose a set of fiducial parameter values corresponding to a f(R)-class model [46]: $\beta_1 = 4/3$, $\beta_2 = 1/2, s = 4, \lambda_s^2 = \beta_1\lambda_1^2 = 1000\ \mathrm{Mpc}^2$.

12-parameter MG model: model-independent pixelization

We also consider the less model-dependent case where μ and γ are pixelized. We choose to have three bins in the linear k range ($10^{-5} - 0.2$ h/Mpc) and for each k bin, we have a *high-z* bin ($3 < z < 30$) and a *low-z* bin ($0 < z < 3$). In total, there are twelve MG pixels, six for μ (# 8-13) and six for γ (# 14-19). $w(z)$ is also binned to one low-z bin (#6) and one high-z one (#7).

6.2 Degeneracy of Parameters

In this section, we study the correlations between the MG and other parameters of the models described in 6.1. For the analysis of this section, the experimental setup, observables and the procedure are similar to that of Chapter 5. From a Fisher analysis of the parameters, we calculate the covariance and correlation matrices for the model parameters.

For each MG parameter, we show two correlation plots. The *normalized* correlation, $\overline{C}_{ij} \equiv C_{ij}/\sqrt{(C_{ii} \times C_{jj})}$, and the *un-normalized* correlation C_{ij}, where C is the covariance matrix of all parameters, computed by inverting the corresponding Fisher matrix. The reason for showing the un-normalized correlations is that it is hard to judge about the importance of correlation between two parameters by just looking at the normalized correlation values. For example, a parameter might be highly correlated with the others while being very well-constrained, which means that it is well-measured anyway. For the un-normalized case, we plot the absolute values of correlations on a semi-log plot. Also we show the $\sqrt{C_{ii} \times C_{jj}}$ values where i runs over all the parameters and j is the index of the MG parameter we are plotting the correlations for. These values will be used as a reference and help us estimate the relative degree of correlations between parameters.

We start from the combination of the CMB and SNe Ia data. We then add the GC and WL data in two steps and study how including them breaks the degeneracies. Finally, we add all the cross-correlations of CMB×CG, CMB×WL and WL×CG. As mentioned, CMB+SNe data are always included and mainly constrain the background parameters. For simplicity, we do not show CMB+SNe and CMB+SNe+WL combinations in the un-normalized plot.

With CMB+SNe data only, one measures the cosmological distances and thus, the background parameters. To describe this, we note that the comoving distance to a redshift z is defined as

$$\chi \propto \int_0^z \frac{dz}{H_0\sqrt{\Omega_m a^{-3} + \Omega_r a^{-4} + \Omega_{DE}}} \tag{6.4}$$

Varying the background parameters changes the comoving distances to observed phenomena such as recombination. This interferes with the growth of perturbations by changing the time available for perturbations to grow, which can be degenerate with changing the growth rate.

With the GC data, one can estimate the density fluctuations of galaxies ($\rho_g\delta_g$) which is related to the total matter density fluctuations, $\rho_m\delta_m$, via the bias parameter. $\rho_m\delta_m$ itself is related to other model parameters via the Poisson equation, Eq. (3.33), which can be written as

$$k^2\psi \propto \mu\rho_m\delta_m \propto \frac{\mu\,\rho_g\delta_g}{b}\,, \tag{6.5}$$

where b is the bias parameter. Hence, the evolution equation for the matter density perturbation, Eq. (3.35), becomes

$$\ddot{\delta}_m + \mathcal{H}\dot{\delta}_m \propto \frac{\mu\,\rho_g\delta_g}{b}\,. \tag{6.6}$$

Having $\rho_g\delta_g$ measured by GC observations, the growth of matter perturbations is directly related to μ, bias and the Hubble parameter.

WL data probes the $\phi+\psi$ combination. From Eqs. (3.33) and (3.34),

$$\psi \equiv \frac{\phi+\psi}{1+\gamma}\,, \tag{6.7}$$

and we can write Eq. (3.35) as

$$\ddot{\delta}_m + \mathcal{H}\dot{\delta}_m \propto \frac{\mu}{1+\gamma}\,\rho_m\delta_m\,. \tag{6.8}$$

Here, the bias parameter is not involved and the growth of matter is directly dependent on $\rho_m\delta_m$. With WL data alone, there is a high degeneracy between the MG parameters and $\Omega_b h^2$, $\Omega_c h^2$ and H_0 (Figs. 6.1, 6.2, 6.3, 6.4, 6.5).

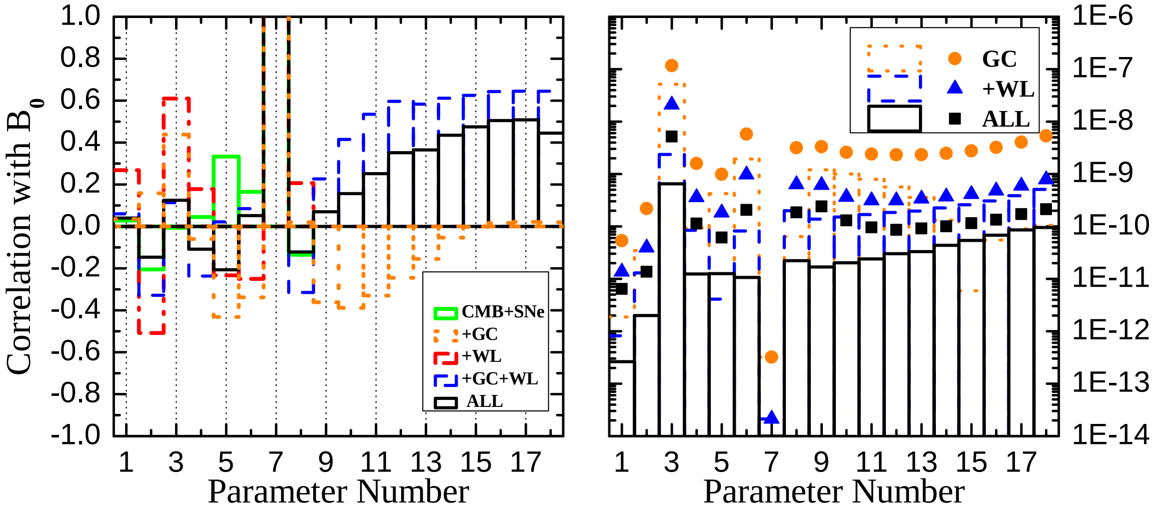

Figure 6.1: Correlation between B_0 (#7) and other parameters, for different combinations of data, normalized (left) and un-normalized (right). CMB+SNe data is also included for the right panel but the graphs are not shown. The scattered points (orange circles, blue triangles and black squares) represent the $\sqrt{C_{B_0B_0} \times C_{ii}}$ value for each parameter i for a comparison with the un-normalized correlation.

When both GC and WL data are included, we have

$$\ddot{\delta}_m + \mathcal{H}\dot{\delta}_m \propto \frac{\mu}{1+\gamma}\,\frac{\rho_g \delta_g}{b}\,. \tag{6.9}$$

Now the galaxy density fluctuations are directly measured by the GC data and we also have the WL measurements. GC and WL data sets probe different combinations of the potentials ϕ and ψ and it helps to break the degeneracies significantly. When adding the cross-correlations of GC and WL, further information about the time evolution of the perturbations is provided. In fact, as we will see, the cross-correlation data puts the strongest constraints on the MG parameters and breaks the degeneracies best.

6.2.1 f(R) models parametrized by B_0

B_0 is related to the Compton wavelength of the scalar DoF. Below this transition scale, the growth of structure is modified due to the presence of the fifth force. Fig. 6.1 shows the normalized (left) and un-normalized (right) correlations between B_0 (#7) and the rest

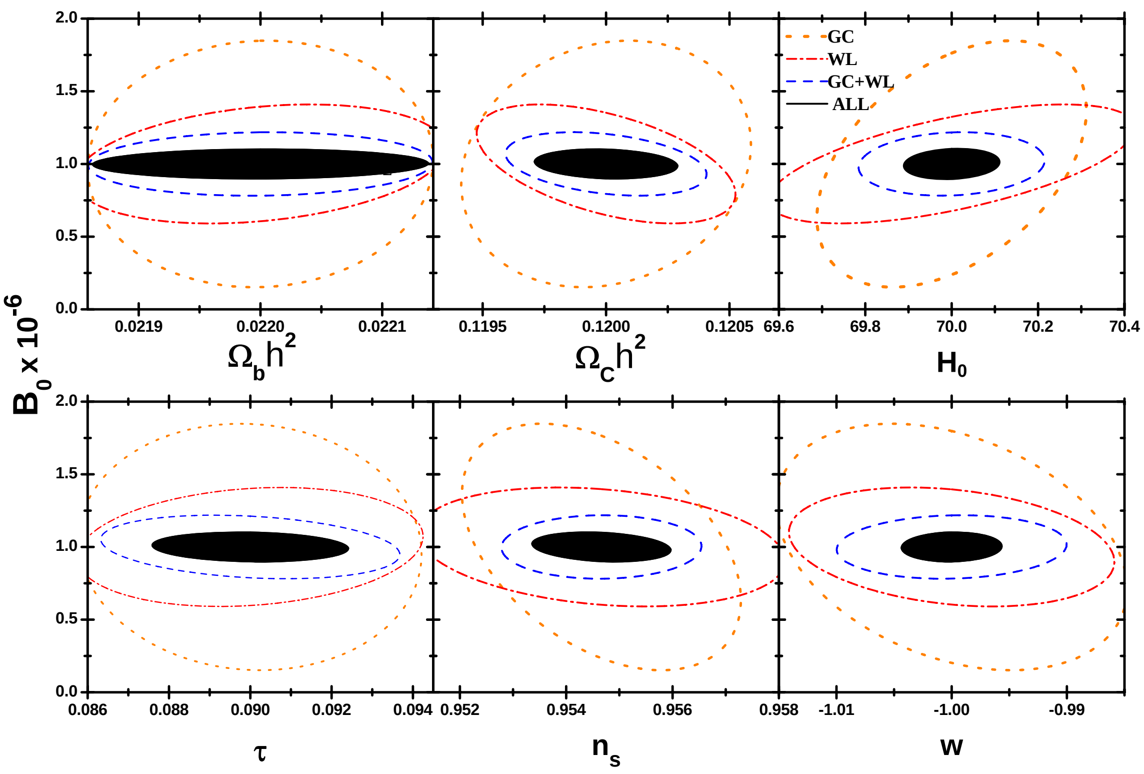

Figure 6.2: The 68% confidence level contours for the basic parameters and B_0.

of the model parameters. We mainly focus on the cases where correlations are significant compared to the corresponding $\sqrt{C_{ii} \times C_{jj}}$ value. For a better demonstration, Fig. 6.2 shows the 68% C.L. contour plots for the basic model parameters and the role of different observables in constraining them.

From the normalized correlation plot, Fig. 6.1 (left), we see that except for the bias, degeneracies between B_0 and other parameters are broken to a better than $\sim 10\%$ level when all data is included. In the following, we briefly study the degeneracies of B_0 with each of the model parameters:

$\Omega_b h^2$: It plays an important role in the radiation domination era through the coupling to photons, and at the recombination, so that the height and separation of the CMB peaks are very sensitive to it. Therefore, $\Omega_b h^2$ is strongly constrained by the CMB data and is not highly correlated with B_0. The correlation is significant only when the WL data is considered without the GC data. With the WL data, the constraints on all parameters, including $\Omega_b h^2$, are relatively tight but there is degeneracy between B_0 and $\Omega_b h^2$, $\Omega_c h^2$ and H_0 due to the reasons discussed in the previous section. However, when GC data is included, the degeneracy is broken (Figs. 6.1-6.2).

$\Omega_c h^2$: The CDM energy density has an important role after the matter-radiation equality epoch. CMB data is mainly sensitive to $\Omega_c h^2$ through the geometry of the universe. The SNe Ia data is also sensitive to it through the value of the Hubble parameter entering the distance measurements. Varying $\Omega_c h^2$ will change the epochs of matter-radiation equality and matter-dark energy equality, leading to a different history of growth of perturbations. The CDM density is also important for the secondary CMB effects, such as the ISW effect. It is an extra source of correlations between the MG parameter and $\Omega_c h^2$.

H_0: Similar to the baryon and CDM densities, H_0 enters the distance measurements by CMB and SNe Ia. Unlike the matter densities, its value does not change the CMB temperature fluctuations (the position and relative heights of the CMB peaks). That is why there is a negligible degeneracy between H_0 and B_0. However, since H_0 enters the evolution equations of matter perturbations, Eq. (3.35), MG parameters are highly degenerate with H_0 after including the large scale structure data. With the cross-correlation data, evolution of matter density perturbations is much better constrained and the degeneracy with H_0 is significantly reduced.

τ: The main impact of the optical depth is on CMB, including the ISW term, Eq. (4.29), and it can be degenerate with how the density perturbations evolve. When including the GC and WL data, this degeneracy still exists, while the constraints on the parameters become tighter. That is why we see higher correlation in Fig. 6.1 (left). Again, with the cross-correlation data, the time evolution of perturbations is much better constrained and the degeneracy is broken.

n_s and A_s: The power spectrum of the primordial perturbations, Eq. (1.57), is related to n_s and A_s parameters as

$$P_\psi(k) \propto A_s k^{n_s-4}, \tag{6.10}$$

so that they determine the initial values of scalar metric perturbations, as well as the matter density perturbations. As a result, the impact of a modification to growth after recombination can, in principle, be degenerate with varying n_s and A_s.

w: As discussed in Chapter 5, it is possible to constrain w and MG parameters simultaneously. w, like other background parameters, affects the growth by changing the expansion history. The dark energy density, and consequently w, influences the recent expansion history and determines the ISW signal. However, most of the information about w is coming from SNe Ia and the main role of the large scale structure data is to break degeneracies with MG parameters (Fig. 6.2).

Bias: As can be seen from Fig. 6.1 and in the next subsections, the bias parameters would have the highest degeneracies with the MG parameters. Observations of galaxies (baryonic matter) are related to the matter density perturbations via the bias parameter, Eq. (3.35). GC data alone is neither able to constrain the bias parameters, nor it can break their degeneracies with B_0. Eq. (6.6) shows that increasing B_0[2] and decreasing the bias have the same impact on the growth of perturbations. In other words, to get the same evolution for δ, a variation in B_0 can be compensated with variations of the bias parameter. This negative correlation, however, would vanish at high redshifts due to less observable galaxies. When WL data is added, the sensitivity to the bias parameters, specially at high redshifts, is increased. However, if we look at the uncorrelated plots, we see that the constraints on parameters are shrunk by almost two orders of magnitude. Hence, the residual degeneracy, although relatively high, are not as important. The cross-correlation data is able to lower the uncertainties, and the correlations, by a factor of few.

With the above description, we have a guideline on how our model parameters could be correlated with the MG parameters of the model. With the 1-parameter MG model, we can mainly study the theories where there is an intrinsic transition scale in the behavior of gravity due to a scalar degree of freedom with a fixed (f(R)) coupling to matter. Hence, in the following subsections, we investigate the degeneracies for models with more MG parameters.

6.2.2 Scaler-tensor models parametrized with (c,s,n)

Fig. 6.3 shows the correlation plots for c (top row), s (middle row) and n (bottom row). Here, c (#7) is a pre-factor controlling the overal amplitude of MG effects, while s (#8) and

---

[2] $\frac{\partial\mu}{\partial B_0} > 0$, so that increasing B_0 is equivalent to increasing μ.

n (#9) control the redshift and scale of the MG effects, respectively. This parametrization is more flexible in capturing a MG feature, compared to the 1-parameter model in the previous section. However, the MG parameters themselves are highly correlated. The high correlations limit how well the MG parameters can be constrained, and we observe that adding the WL data does not improve the constraints significantly.

From the left panels of Fig. 6.3, we see that c has a negative correlation with both s and n. An increase of c will enhance the growth on all scales. Increasing n decreases the enhancement of growth on larger scales and pushes the MG effects to smaller scales. Hence, the impact of c on the linear growth is opposite to that of n. Increasing s pushes the MG effects to more recent times (smaller redshifts). Data is able to discriminate between c and s from the measurement of the growth at multiple redshift bins but c and n are producing highly degenerate effects. s and n, on the other hand, are positively correlated because increasing s pushes the MG effects to smaller redshifts. For the WL data, as the dominant observable, this effect is degenerate with increasing n, which pushes the MG effects to smaller scales. This degeneracy is an intrinsic property of the WL potential, as described in Chapter 5.

Fig. 6.3 shows that degeneracies of the MG parameters with other parameters are broken to a good extent after including the WL data. In particular, degeneracies with the bias parameters are reduced so that, $\overline{C}_{ij} = C_{ij}/\sqrt{(C_{ii} \times C_{jj})} \lesssim 0.1$ in all cases. One can see that there is a sweet spot in redshift where the bias parameters are best constrained. One recalls from Section 5.4 that this spot, in the middle redshift range, is where the best eigenmodes of the MG functions are peaked.

We see that adding new MG parameters provides more flexibility in detecting MG effects, but the MG parameters will be highly correlated. One suspects that adding even more MG parameters to the model might just weaken the constraints, without providing any new information. In the next section, we consider a model with more MG parameters and test how redundant the extra parameters would be.

6.2.3 General model parametrized with BZ parameters

Fig. 6.4 shows the correlations for $\log(\lambda_1^2)$ (first row), $\log(\lambda_2^2)$ (second row), β_1 (third row) and s (last row). Here, (β_1,β_2) are the analogues of c in the (c,s,n) model, while (λ_1,λ_2) are similar to n, i.e. controlling the transition scale where the MG effects become important. s in both models has the same role.

The main reason for including this model is to show the redundancy of the extra MG parameters introduced. Comparing the plots in the Figs. 6.3 and 6.4 shows that there are more degeneracies in this model, specially with the bias parameters. We notice that λ_1 and λ_2 are constrained very similarly by data. It might seem in contradiction with what we expect from the previous Chapter that μ (and hence, λ_1) should be better constrained than γ (hence, λ_2). But, we see in Fig. 6.4 that there is almost a perfect correlation between λ_1 and λ_2. This correlation limits how well data constrains λ_1, via the uncertainties of λ_2 measurement. λ's also have a high positive correlation with s (#11) due to the same reason that explained the correlation between n and s in the (c,s,n) model. Similarly, β_1 and β_2 are also highly correlated [3].

As before, larger s would lead to the enhancement of the growth starting at a larger redshift and accumulating over time. This mimics the effect of a stronger fifth force due to an increase of β's. Since s is a common parameter to both the BZ model of this section and the (c,s,n) model of the previous section, with the same fiducial value, we can get an estimate of how much the constraints on the parameters are diluted and how much extra degeneracy is introduced. Comparing the un-normalized plots for s in Figs. 6.3 and 6.4 shows that both the errors and the correlations are higher by at least one order of magnitude.‘

6.2.4 Pixelated MG functions

In Fig. 6.5, the correlation plots are shown for the middle-k ($0.07 < k < 1.4$ h/Mpc), low-z pixels of μ (top row) and γ (bottom row). We choose these pixels since, as we saw in Chapter 5, they cover the scales and redshifts where LSST is most sensitive to the modified growth.

In the previous models, the MG parameters were introduced in a way that they would affect the MG parameter values at all scales and redshifts. This inevitably produces correlations between the MG parameters. On the other hand, with the MG pixels, the modified growth is confined to the ranges covered by each pixel so that correlations are intrinsically lower. In particular, the μ pixels are less correlated with the γ pixels as one can compare

---

[3] Therefore, we did not include the correlation plots for β_2.

with the correlations of μ and γ parameters in the BZ model. As a result, the errors on the μ pixels (#8-13) are obviously smaller than (and are not limited by) those of the γ pixels (#14-19).

The other advantage of working with the MG pixels is that one can isolate some of the physical processes that affect the growth at particular scales or redshifts. For example, we see from Fig. 6.5 that there is a relatively smaller error on the first high-z γ pixel (# 15) compared to the error on the other two pixels (# 17,13). We recall from Section 5.4 that the ISW effect strongly constrains the γ function at large scales and the first high-z γ pixel happens to cover those scales.

In Section 5.6, we concluded that in spite of correlations between the MG pixels and w bins, future surveys like LSST are able to constrains both functions simultaneously. We can look at the correlations in more detail here. From Fig. 6.5, we see high correlation between the MG pixels and the high-z w bin (#7), which is positive (negative) for μ (γ). This is reasonable as increasing w would change the onset of the acceleration phase to a later time and hence, more time for the growth of perturbations. On the other hand, the low-z w bin (#6) has a negligible degeneracy with the MG pixels, again, in accordance with what we expect. Since most of the low-z information on w is coming from SNe Ia data and, the low-z w bins are not correlated with the MG pixels.

The plots also show a general trend of negative correlations between the high-z pixels with their corresponding low-z pixels. It makes sense as any change in the high-z (low-z) pixel value should be counteracted with a change in the corresponding low-z (high-z) pixel values. As for MG parameters in the previous models, there are also high correlations between pixels and basic parameters, like H_0 or A_s (#20), and the bias parameters.

6.3 Other degenerate effects

In this subsection, we take the 3-parameter (c,s,n) model and generalize our analysis by including the WL systematics (described in Section 5.5) and considering neutrinos to be massive. We would like to know how these additional effects change the correlations between the MG and other parameters. We first include the WL systematics and, in the next step, the massive neutrinos. Massive neutrinos are taken here as a part of the dark matter (DM) in the universe and their total mass is considered as a parameter in the Fisher analysis, with a fiducial value of $\Sigma m_\nu = 0.05$ eV.

Fig. 6.6 shows the correlations for c (top row), s (middle row) and n (bottom row) in four cases: without any additional effects, with systematics, with massive neutrinos and with both systematics and massive neutrinos. For these plots we used the full data combination. The total mass of neutrinos is considered as the last parameter (#21) in the plots.

Systematics do not change the parameter constraints and their correlations considerably. With massive neutrinos, however, the correlations of MG parameters with each other, with the bias parameters and some of the basic parameters increases significantly. Massive neutrinos, as part of the DM, would freely stream and slow down the growth on the free-streaming scales. The heavier they are, the larger portion of DM they make, leaving less CDM in the universe. This slows down the growth and, hence, massive neutrinos are negatively correlated with c. Heavier neutrinos would have a shorter free-streaming scale. This is roughly the same as the effect of increasing s or n, thus, explaining their positive correlation.

6.4 Summary

In this chapter, we studied the degeneracies between different sets of MG parameters with the other parameters that are usually considered in models of large scale structure formation. We used a combination of the CMB, SNe Ia and large scale structure experiments, did a Fisher analysis of the parameters and computed their correlation matrix.

We considered three models with parametric forms of the MG functions. We saw in Section 6.2 that in the 3-parameter MG model, degeneracies were broken to a good extent but there were relatively high correlations between the MG parameters themselves. It was also demonstrated that increasing the number of the MG parameters would introduce redundancies and weaken the constraints. Finally, with pixelization of the MG functions, we were able to study the degeneracies at different scales and redshifts.

Among the model parameters, the bias parameters had the highest correlation with the MG parameters, due to their direct involvement in the equation for the growth of perturbations, Eq. (3.35). It seems that for the 3-parameter model, it was possible to break such degeneracies better without weakening the overall constraints on the parameters. The background parameters were degenerate with MG mainly through the expansion history and its impact on the growth time. With the GC and WL data combined, one probes two different combinations of the scalar potentials. This leads to tight constraints and relatively low degeneracies. Among the observables we used, WL provides most of the information about the growth at low redshifts. The intrinsic degeneracy between the scale and the redshift in the WL kernel limits its ability in probing the time evolution of perturbations. This leads to some residual degeneracies between the MG and the basic parameters. In such cases, the cross-correlation of WL and GC data at multiple tomographic redshift bins will significantly break the degeneracies. In fact, the cross-correlation power spectra are the most informative observables for probing the growth of structure.

We have also considered other physical effects that could be degenerate with a modification to gravity. The WL systematics that we considered in our analysis did not change the correlations while the presence of massive neutrinos could have an important impact. It would be interesting to investigate how including new type of observables, such as redshift space distortion (RSD) [210, 235], would resolve such degeneracies.

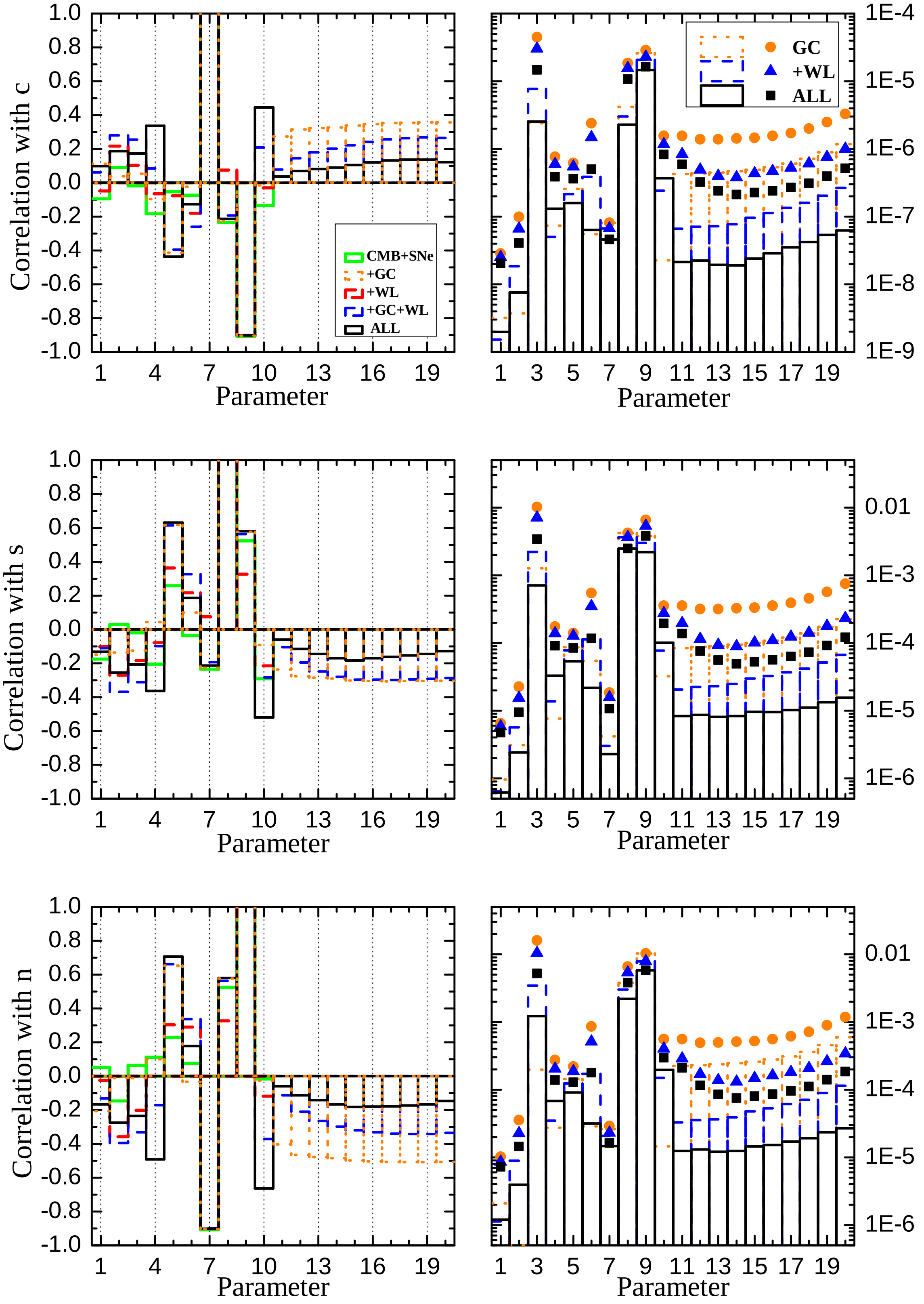

Figure 6.3: Correlation between *c* (top row), *s* (middle row) and *n* (bottom row) and other parameters for different combinations of data, same as in Fig. 6.1.

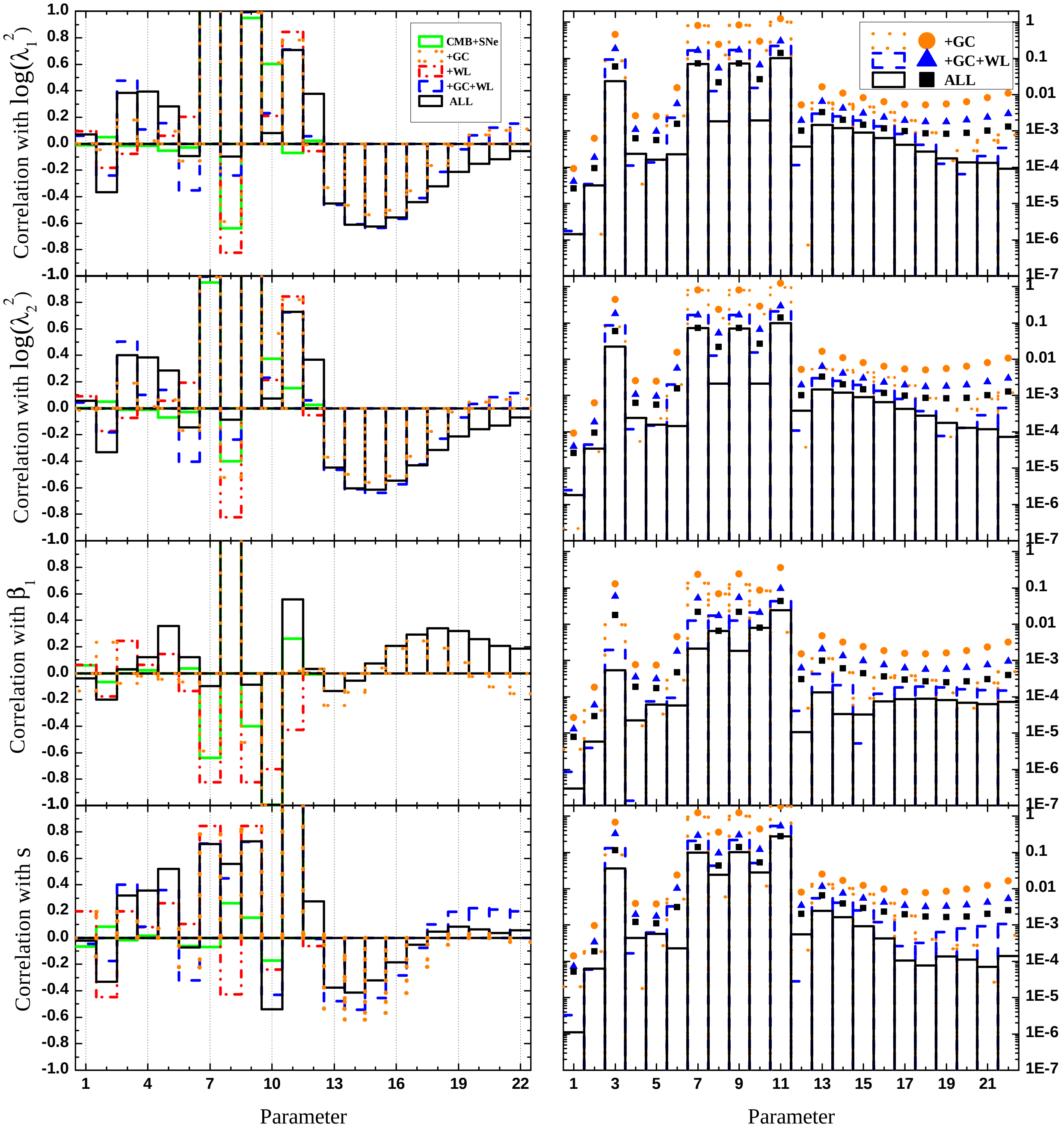

Figure 6.4: Correlation between $\log(\lambda_1^2)$ (first row), $\log(\lambda_2^2)$ (second row), β_1 (third row) and s (last row) and other parameters for different combinations of data.

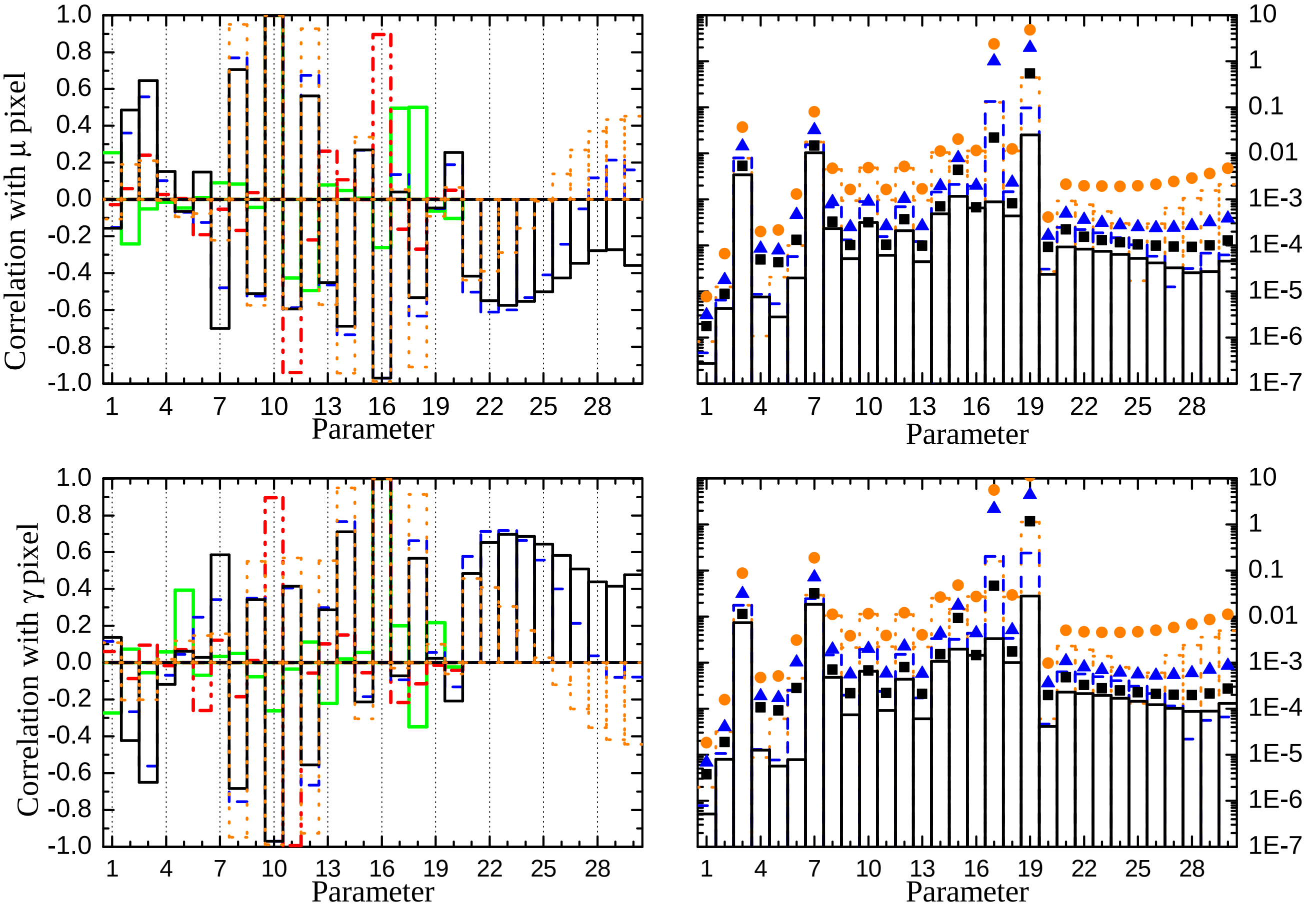

Figure 6.5: Correlation between pixelated and other parameters for different combinations of data.

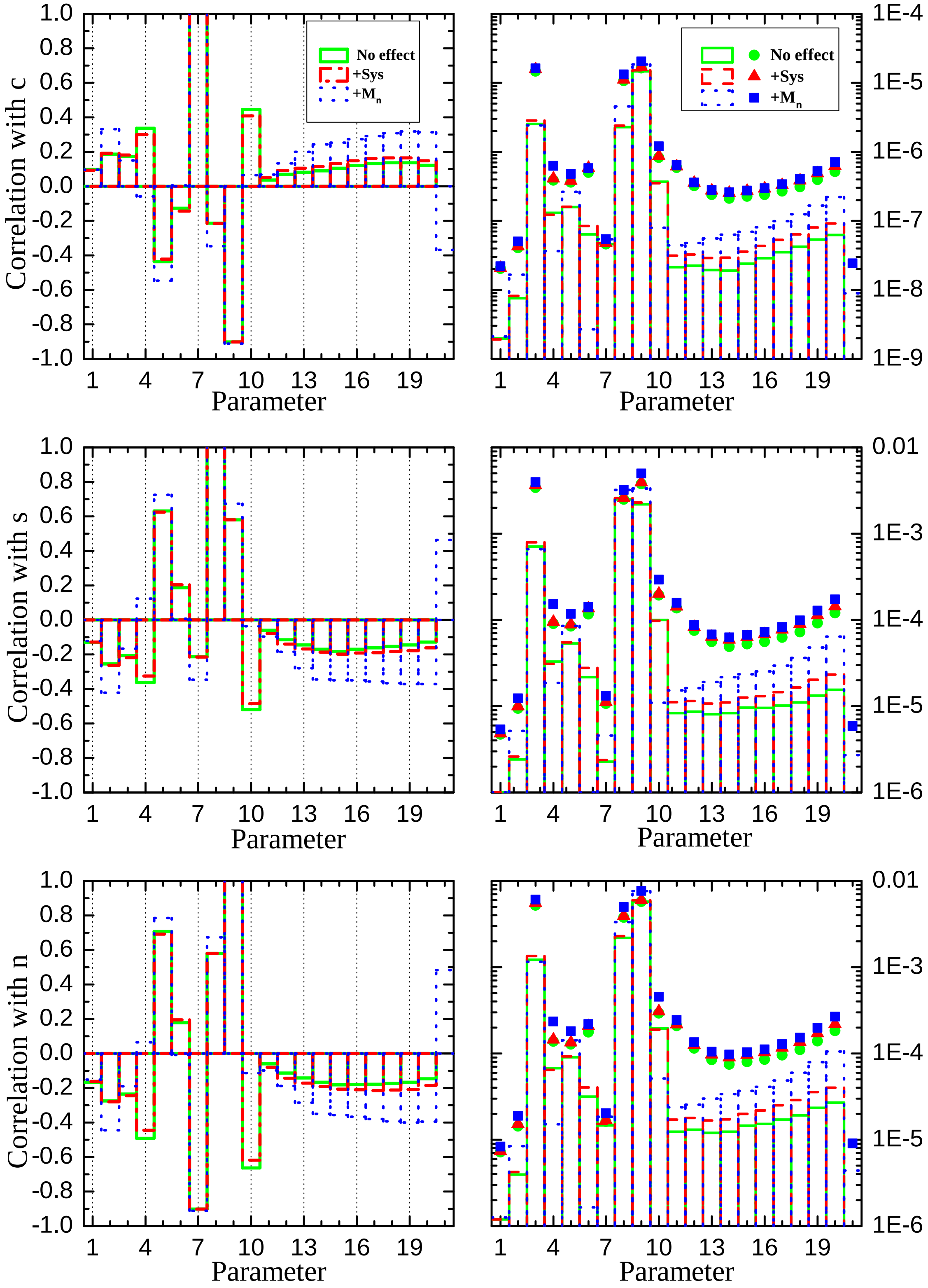

Figure 6.6: correlations for *c* (top row), *s* (middle row) and *n* (bottom row) with full data. Three cases are compared: when no additional effects are included, when the WL systematics included and when neutrinos are massive.

Chapter 7

Summary and future directions

We started this thesis with a brief review of the basics concepts in cosmology and the observables that cosmological surveys measure. We then described the main pieces of observational evidence for the accelerated expansion of the universe and the ΛCDM model. After describing some of the theoretical problems associated with the cosmological constant, we outlined the possible alternatives.

Dark energy

In Chapter 2, after a brief overview of the proposed theories of dark energy, we described the phenomenological approaches to measuring its properties. Different techniques have been used to constrain w, and its dynamical behavior, using probes of cosmological distances. We introduced wavelets as an effective expansion basis for detecting local dynamics in $w(z)$. Assuming a flat universe, we demonstrated that such features are detectable from a combination of futuristic cosmological distance measurements, namely, SNe Ia, CMB and BAO data. Relaxing the flatness assumption made such features undetectable due to the high degeneracy with the curvature parameter, Ω_k.

This work can be extended using other types of observables, including data from the ongoing and upcoming large scale structure surveys. While w is a background parameter (zeroth-order in perturbation theory), it affects the growth of matter perturbations. With the upcoming high-quality data, further information about w will be provided. We stress that a conclusion about any deviation of w from its ΛCDM value should be made based on a consistent detection from a collection of the available methods. This way, any bias or model-dependence of the methods could be eliminated.

Modified gravity

As the alternative to the existence of a dark energy component in the universe, we reviewed how modifications to GR can produce accelerated expansion on cosmological scales. We provided some theoretical background for the modified gravity models and discussed their problems. Since the background evolution (expansion) of the universe is more or less fixed from a combination of independent observations, one needs to look at the evolution of perturbations for distinguishing between different theories. Again, in the absence of a compelling theory of modified gravity, we turned our attention to phenomenological approaches for detecting possible deviations from the evolution predicted by GR.

An example of such an approach is a model-independent parametrization of the linear growth of structure. It is done by introducing two functions of scale and time (MG functions) with well-defined values in ΛCDM, but different values in alternative dark energy and modified gravity theories. We reviewed how the linear growth of matter perturbations can be parametrized in a general way using the two functions. The main value of this method is in allowing for a model-independent way of looking for departures from GR.

MGCAMB

We described in detail how the parametrized equations of linear perturbations can be implemented in the numerical Einstein-Boltzmann solver codes, such as CAMB, that makes it possible to evaluate the cosmological observables from the parametrized equations. We demonstrated the capabilities of our code (MGCAMB) by obtaining joint constraints on the neutrino mass and parameters of two models of modified gravity. We found that GR remained a good fit in all cases. We have made the MGCAMB patch public at `http://www.sfu.ca/~aha25/MGCAMB.html` and will update it regularly to keep it compatible with the latest distributions of CAMB.

PCA of MG functions

In Chapter 5, we described how a Fisher analysis can be used to forecast the errors on the MG functions, parametrizing the modified Poisson equation (μ) and the ratio (γ) between the two Newtonian potentials from WL surveys such as DES and LSST, combined with CMB data from Planck and futuristic SNe Ia data. By applying Principal Component Analysis (PCA), we were able to work with the eigenmodes of the MG functions. We also considered other choices of MG functions and studied their merits. After introducing some of the systematic effects in WL surveys, we studied how they impact the eigenmodes of (μ,γ) functions, as well as the scales and redshifts where these effects are most prominent. Finally, we demonstrated the utility of PCA as a data compression formalism for an efficient storage of information about modified growth on linear scales, and how this information can be *projected* to constrain the parameters of specific MG models, rather than doing a separate analysis for each model from scratch.

Some of the aspects of this analysis can be further investigated. For example, one can study in more detail the range of applicability and precision of the projection method, as compared to the direct Fisher analysis, in constraining model parameters. This can be done by computing the constraints on parameters of different MG models from the two methods to check the agreement.

Another direction for future work is to revisit the assumed scale-independence of the galaxy bias. In [236], it was shown that a scale-dependent growth necessarily implies a scale-dependent bias on linear scales. In the present analysis, this was effectively encoded in our function μ, but in a future study it may be interesting to include the scale-dependent bias explicitly. In addition to scale-dependent bias, scale-dependent initial conditions may also be degenerate with the MG modes.

The PCA technique represents a model-independent way of analyzing the power of cosmological surveys to constrain modified growth. In addition to forecasts, it can be applied to current data. For instance, given an array of experiments, one can use a Fisher forecast to first find the eigenmodes, then fit the amplitudes of these modes to real data. Because these modes are expected to be (nearly) orthogonal to each other, it does not matter if one fits them one by one or simultaneously. If any of them is found to deviate from zero significantly, it would constitute a smoking gun for modified gravity. Alternatively, if Fisher forecasted eigenmodes are found to be non-negligibly correlated, it would indicate that the fiducial model assumed in their derivation was wrong and that a modification is needed.

We also investigated the degeneracy of the MG functions with other parameters, such as the basic cosmological parameters, galaxy bias and, most importantly, with $w(z)$, to see how well future data can constrain DE and modification to gravity simultaneously. The degeneracy between μ and γ, or Σ, can be further broken by adding information from RSD measurements. It will be interesting to extend our analysis to include RSD for surveys that simultaneously measure lensing and peculiar velocities, such as DESpec and Euclid.

Appendix A

The model for WL and GC systematics

We follow [25, 231] and consider three sources of systematics for future tomographic imaging surveys: photo-z errors, as well as additive and multiplicative errors due to the uncertainty of the point spread function (PSF) measurements.

Photo-z Errors

The redshift errors may stem from three sources: the distortion of the total galaxy distribution, z-bias and z-scatter.

Distortion of the total galaxy distribution: Suppose the observers measure the redshift z using some photometric method, and $\Delta\bar{z} \equiv z - \bar{z}$ denotes the error. This error, in general, might induce a distortion of the overall distribution of the galaxies. To quantify this effect, we follow [25] to expand $\Delta\bar{z}$ using the smooth Chebyshev polynomials ($T_n(x) = \cos(n \arccos x)$):

$$\Delta\bar{z} = \sum_{i=1}^{N_{\rm chb}} g_i T_i\left(\frac{\bar{z} - z_{\rm max}/2}{z_{\rm max}/2}\right). \tag{A.1}$$

As argued in [25], choosing $N_{\rm chb} = 30$ is large enough to yield convergent result, and we follow this setting. If the expansion coefficients g_i's are much smaller than unity, the biased galaxy distribution can be estimated as

$$N(z) = \bar{N}\left[z - g_i T_i\left(\frac{\bar{z} - z_{\rm max}/2}{z_{\rm max}/2}\right)\right] \tag{A.2}$$

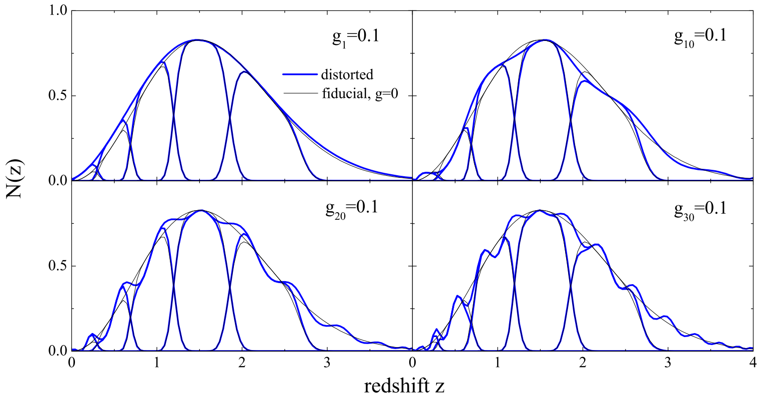

Figure A.1: Redshift error - distortion: distortion of the total galaxy distribution due to uncertainties in redshift measurement, plotted here for LSST. g_i's are expansion coefficients of $\Delta\bar{z}$ in terms of Chebyshev polynomials (A.1).

The galaxy distribution of the *i*th bin is,

$$N_i(z) \propto N(z)\left[\mathrm{erfc}\left(\frac{z_{\mathrm{i}-1} - z}{\sqrt{2}\sigma(z)}\right) - \mathrm{erfc}\left(\frac{z_{\mathrm{i}} - z}{\sqrt{2}\sigma(z)}\right)\right] \tag{A.3}$$

Thus if the overall distribution is biased by g, all the redshift bins are biased accordingly, as shown in Fig A.1 (We show the galaxy distributions of LSST for an example).

In our calculations we account for this effect by marginalising over 30 Chebyshev coefficients.

Redshift-bin Centroids Uncertainty: To be general, we also consider the possible degradation if there exists some uncertainty in measuring the centroids of the redshift bins, i.e. the so-called non-vanishing z-bias $b_i \equiv z_i - \bar{z}_i \neq 0$. The z-bias basically 'shifts' the centroids of the bins. See this effect illustrated in Fig A.2. In the calculation, we assign one z-bias parameter for each bin, then marginalize over them.

Note that the centroid shifts do not capture the catastrophic errors where a smaller fraction of redshifts are completely mis-estimated and reside in a separate island in the $z - \bar{z}$ plane [25, 232].

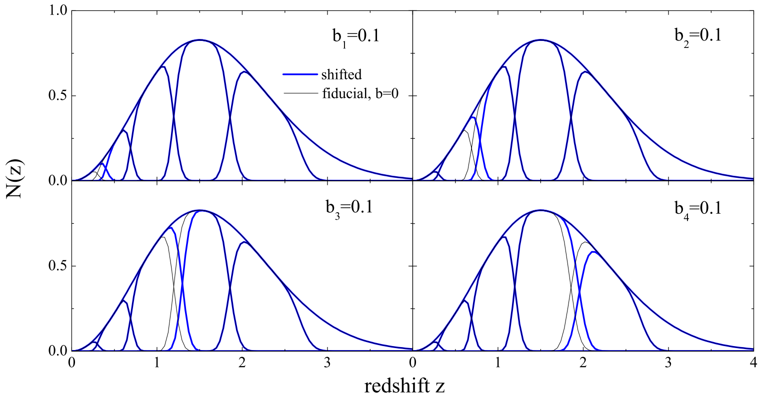

Figure A.2: Redshift error - shift: uncertainty in measuring the centroids of the redshift bins (non-vanishing z-bias), quantified by b_i coefficients at redshift bin i.

z-scatter: We assume that $\sigma(z) = \sigma_0(1+z)$, and we choose $\bar{\sigma}_0 = 0.03(0.05)$ for fiducial model for LSST (DES). But if σ_0 is not perfectly measured, i.e., the z-scatter is not zero, $\Delta \equiv \sigma_0 - \bar{\sigma}_0 \neq 0$, there will be further degradation. In the calculation, we assign one z-scatter parameter for each bin, then marginalize over. As shown in [25], this effect is sub-dominant.

Additive errors

Additive errors are present for both galaxy counts and lensing shear measurements, and they are generated, for example, by the anisotropy of the point spread function (PSF). Following [25] and [231], we parametrize the additive errors as

$$(C_\ell^{\mathrm{XY}})_{ij} = \delta_{\mathrm{XY}} \rho A_i^{\mathrm{X}} A_j^{\mathrm{Y}} \left(\frac{\ell}{\ell_*^{\mathrm{X}}} \right)^{\gamma} \tag{A.4}$$

and choose $\rho = 1, \gamma = 0$. The fiducial values of the A's are, $(A^g)^2 = 10^{-8}, (A^\gamma)^2 = 10^{-9}$ [231].

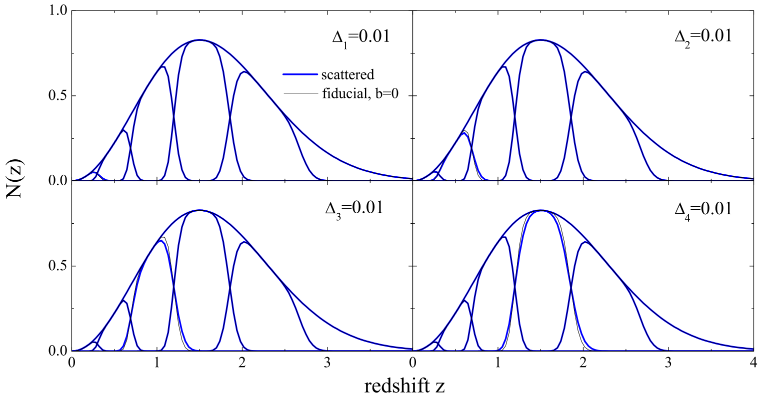

Figure A.3: Redshift error - scatter: uncertainties in the photo-z error at redshift z modeled as $\sigma(z) = \sigma_0(1+z)$, where Δ_i is $\sigma_0 - \bar{\sigma}_0$ at redshift bin i.

Multiplicative errors

Multiplicative errors in measuring shear can be introduced by various sources. For example, a circular PSF of finite size is convolved with the true image of the galaxy to produce the observed image, and in the process it produces a multiplicative error [25].

$$(\widetilde{C}_\ell^\gamma)_{ij} = (C_\ell^\gamma)_{ij}[1 + f_i + f_j] \tag{A.5}$$

We choose $f = 0$ as fiducial.

Bibliography

[1] A. Einstein, Preuss. Akad. Wiss. Berlin, 1915: 844-847, (1915).

[2] E.P. Hubble, Proc. Nat. Acad. Sci., 15, 168-173, (1929).

[3] A.G. Riess et al., Astron. J., 116, 1009-1038, (1998).

[4] S. Perlmutter et al., Astrophys. J., 517, 565-586, (1999).

[5] A.G. Riess et al., Astrophys. J., 607, 665-687, (2004).

[6] A. Einstein, Preuss. Akad. Wiss. Berlin, 1917: 142-152, (1917).

[7] A. Friedmann, Zeitschrift fur Physik, 10, 377-386, (1922).

[8] E. J. Copeland, M. Sami and S. Tsujikawa, Int. J. Mod. Phys. D *15*, 1753 (2006).

[9] R. Bean and O. Dore, Phys. Rev. **D69**, p. 083503 (2004).

[10] J. Weller and A. M. Lewis, Mon. Not. Roy. Astron. Soc. **346**, 987 (2003).

[11] W. Hu and R. Scranton, Phys. Rev. **D70**, p. 123002 (2004).

[12] M. Ishak, A. Upadhye and D. N. Spergel, Phys. Rev. **D74**, p. 043513 (2006).

[13] S. Hannestad, Phys. Rev. **D71**, p. 103519 (2005).

[14] L. Knox, Y.-S. Song and J. A. Tyson, Phys. Rev. **D74**, p. 023512 (2006).

[15] E. Bertschinger, Astrophys. J. **648**, 797 (2006).

[16] S. Wang, L. Hui, M. May and Z. Haiman, Phys. Rev. **D76**, p. 063503 (2007).

[17] W. B. Bonnor, Monthly Notices of the Royal Astronomical Society, Vol. 117, p.104 (1957).

[18] C. -P. Ma and E. Bertschinger, Astrophys. J. *455*, 7 (1995) [astro-ph/9506072].

[19] S. Dodelson, "Modern Cosmology", Academic Press (2003).

[20] D. J. Eisenstein et al., Astrophys. J. **633**, 560 (2005).

[21] W. J. Percival *et al.* [SDSS Collaboration], Mon. Not. Roy. Astron. Soc. **401**, 2148 (2010) [arXiv:0907.1660 [astro-ph.CO]].

[22] M. Kowalski et al., Astrophys. J. **686**, 749 (2008).

[23] W. H. Press, P. Schechter, Astrophysical Journal, Vol. 187, pp. 425-438 (1974).

[24] D. Wittman et al, Nature *405*, 143 (2000).

[25] D. Huterer, M. Takada, G. Bernstein and B. Jain, Mon. Not. Roy. Astron. Soc. **366**, 101 (2006) [arXiv:astro-ph/0506030].

[26] D. Kirk, I. Laszlo, S. Bridle and R. Bean, arXiv:1109.4536 [astro-ph.CO].

[27] I. Laszlo, R. Bean, D. Kirk and S. Bridle, arXiv:1109.4535 [astro-ph.CO].

[28] M. R. Nolta et al., Astrophys. J. Suppl. *180*, 296 (2009).

[29] D. Huterer, Gen. Rel. Grav. **42**, 2177 (2010) [arXiv:1001.1758 [astro-ph.CO]].

[30] E. Semboloni et al., Astron. Astrophys. *452*, 51 (2006).

[31] L. Fu et al., Astron. Astrophys. *479*, 9 (2008).

[32] O. Dore et al. (2007).

[33] R. Massey et al., Astrophys. J. Suppl. *172*, 239 (2007).

[34] J. Lesgourgues, M. Viel, M. G. Haehnelt and R. Massey, JCAP *0711*, p. 008 (2007).

[35] `http://www.darkenergysurvey.org/`

[36] `http://www.lsst.org`

[37] P. Zhang, M. Liguori, R. Bean and S. Dodelson, Phys. Rev. Lett. **99**, p. 141302 (2007).

[38] R. Caldwell, A. Cooray and A. Melchiorri, Phys. Rev. **D76**, p. 023507 (2007).

[39] L. Amendola, M. Kunz and D. Sapone, JCAP **0804**, p. 013 (2008).

[40] B. Jain and P. Zhang, Phys. Rev. **D78**, p. 063503 (2008).

[41] E. Bertschinger and P. Zukin, Phys. Rev. **D78**, p. 024015 (2008).

[42] Y.-S. Song and K. Koyama, JCAP **0901**, p. 048 (2009).

[43] F. Schmidt, Phys. Rev. **D78**, p. 043002 (2008).

[44] P. Zhang, R. Bean, M. Liguori and S. Dodelson (2008).

[45] G.-B. Zhao, L. Pogosian, A. Silvestri and J. Zylberberg, Phys. Rev. **D79**, p. 083513 (2009).

[46] G.-B. Zhao, L. Pogosian, A. Silvestri and J. Zylberberg, Phys. Rev. Lett. **103**, p. 241301 (2009).

[47] A. Hojjati, G. -B. Zhao, L. Pogosian, A. Silvestri, R. Crittenden and K. Koyama, Phys. Rev. D **85**, 043508 (2012) [arXiv:1111.3960 [astro-ph.CO]].

[48] S. Perlmutter *et al.* [Supernova Cosmology Project Collaboration], Astrophys. J. **517**, 565 (1999) [astro-ph/9812133].

[49] A. G. Riess *et al.*, Astron. J. *116*, 1009 (1998); Astron. J. *117*, 707 (1999).

[50] A. G. Riess *et al.* [Supernova Search Team Collaboration], Astrophys. J. *607*, 665 (2004).

[51] T. R. Choudhury and T. Padmanabhan, Astron. Astrophys. **429**, 807 (2005).

[52] E. Komatsu *et al.* [WMAP Collaboration], Astrophys. J. Suppl. *192*, 18 (2011) [arXiv:1001.4538 [astro-ph.CO]].

[53] R. Jimenez, P. Thejll, U. Jorgensen, J. MacDonald and B. Pagel, MNRAS, 282, 926 (1996).

[54] H. Richer *et al.*, Astrophys. J. *574*, L151 (2002).

[55] B. Hansen *et al.*, Astrophys. J. *574*, L155 (2002).

[56] T. Giannantonio, R. Scranton, R. G. Crittenden, R. C. Nichol, S. P. Boughn, A. D. Myers and G. T. Richards, Phys. Rev. D **77** (2008) 123520 [arXiv:0801.4380 [astro-ph]].

[57] C. H. Lineweaver and C. A. Egan, Astrophysical Journal, Vol 671, 853 (2007).

[58] S. Weinberg: Rev. Mod. Phys. 61, 1 (1989).

[59] Y. Fukuda *et al.* [Super-Kamiokande Collaboration], Phys. Rev. Lett. **81**, 1562 (1998) [arXiv:hep-ex/9807003].

[60] Q. R. Ahmad *et al.* [SNO Collaboration], Phys. Rev. Lett. **89**, 011301 (2002) [arXiv:nucl-ex/0204008].

[61] G. L. Fogli *et al.*, Phys. Rev. D **75** (2007) 053001 [arXiv:hep-ph/0608060].

[62] M. Maltoni, T. Schwetz, M. A. Tortola and J. W. F. Valle, New J. Phys. **6** (2004) 122 [arXiv:hep-ph/0405172].

[63] S. Wang, Z. Haiman, W. Hu, J. Khoury and M. May, Phys. Rev. Lett. **95**, 011302 (2005) [astro-ph/0505390].

[64] A. J. Albrecht *et al.*, arXiv:astro-ph/0609591.

[65] C. Wetterich, Astron. Astrophys. **301**, 321 (1995) [arXiv:hep-th/9408025].

[66] P. Binetruy, Phys. Rev. D **60**, 063502 (1999) [arXiv:hep-ph/9810553].

[67] P. G. Ferreira and M. Joyce, Phys. Rev. Lett. **79**, 4740 (1997).

[68] P. G. Ferreira and M. Joyce, Phys. Rev. **D58**, p. 023503 (1998).

[69] R. R. Caldwell and M. Kamionkowski, Ann. Rev. Nucl. Part. Sci. **59**, 397 (2009) [arXiv:0903.0866 [astro-ph.CO]].

[70] E. J. Copeland, A. R. Liddle and D. Wands, Phys. Rev. D **57**, 4686 (1998) [arXiv:gr-qc/9711068].

[71] C. Armendariz-Picon, T. Damour and V. F. Mukhanov, Phys. Lett. B **458**, 209 (1999) [arXiv:hep-th/9904075].

[72] R. J. Scherrer, Phys. Rev. Lett. **93**, 011301 (2004) [arXiv:astro-ph/0402316].

[73] T. Chiba, T. Okabe and M. Yamaguchi, Phys. Rev. D **62**, 023511 (2000) [arXiv:astro-ph/9912463].

[74] C. Armendariz-Picon, V. F. Mukhanov and P. J. Steinhardt, Phys. Rev. Lett. **85**, 4438 (2000) [arXiv:astro-ph/0004134].

[75] J. A. Frieman, C. T. Hill, A. Stebbins and I. Waga, Phys. Rev. Lett. **75**, 2077 (1995) [arXiv:astro-ph/9505060].

[76] K. Choi, Phys. Rev. D **62**, 043509 (2000) [arXiv:hep-ph/9902292].

[77] J. E. Kim and H. P. Nilles, Phys. Lett. B **553**, 1 (2003) [arXiv:hep-ph/0210402].

[78] L. A. Boyle, R. R. Caldwell and M. Kamionkowski, Phys. Lett. B **545**, 17 (2002) [arXiv:astro-ph/0105318].

[79] S. Kasuya, Phys. Lett. B **515**, 121 (2001) [arXiv:astro-ph/0105408].

[80] M. Nishiyama, M. a. Morita and M. Morikawa, arXiv:astro-ph/0403571.

[81] N. Arkani-Hamed, H. C. Cheng, M. A. Luty and S. Mukohyama, JHEP **0405**, 074 (2004) [arXiv:hep-th/0312099].

[82] P. Creminelli, G. D'Amico, J. Norena and F. Vernizzi, arXiv:0811.0827 [astro-ph].

[83] R. Fardon, A. E. Nelson and N. Weiner, JCAP **0410**, 005 (2004) [arXiv:astro-ph/0309800].

[84] R. D. Peccei, Phys. Rev. D **71**, 023527 (2005) [arXiv:hep-ph/0411137].

[85] N. Afshordi, M. Zaldarriaga and K. Kohri, Phys. Rev. D **72**, 065024 (2005) [arXiv:astro-ph/0506663].

[86] A. W. Brookfield, C. van de Bruck, D. F. Mota and D. Tocchini-Valentini, Phys. Rev. D **73**, 083515 (2006) [Erratum-ibid. D **76**, 049901 (2007)] [arXiv:astro-ph/0512367].

[87] R. R. Caldwell, Phys. Lett. B **545**, 23 (2002) [arXiv:astro-ph/9908168].

[88] R. R. Caldwell, M. Kamionkowski and N. N. Weinberg, Phys. Rev. Lett. **91**, 071301 (2003) [arXiv:astro-ph/0302506].

[89] B. McInnes, JHEP **0208**, 029 (2002) [arXiv:hep-th/0112066].

[90] We are grateful to Neven Bilic, Gary Tupper and Raoul Viollier for correspondence on this point.

[91] R. Jackiw, arXiv:physics/0010042.

[92] N. Bilic, G. B. Tupper and R. D. Viollier, arXiv:astro-ph/0207423.

[93] M. C. Bento, O. Bertolami and A. A. Sen, Phys. Rev. D **66**, 043507 (2002).

[94] L. Amendola, F. Finelli, C. Burigana and D. Carturan, JCAP **0307**, 005 (2003).

[95] E. V. Linder, Phys. Rev. Lett. **90**, 091301 (2003) [arXiv:astro-ph/0208512].

[96] M. Chevallier and D. Polarski, Int. J. Mod. Phys. D **10**, 213 (2001) [arXiv:gr-qc/0009008].

[97] P. S. Corasaniti, M. Kunz, D. Parkinson, E. J. Copeland and B. A. Bassett, Phys. Rev. D **70**, 083006 (2004) [arXiv:astro-ph/0406608].

[98] U. Alam, V. Sahni, T. D. Saini and A. A. Starobinsky, Mon. Not. Roy. Astron. Soc. **354**, 275 (2004) [arXiv:astro-ph/0311364].

[99] B. A. Bassett, P. S. Corasaniti and M. Kunz, Astrophys. J. **617**, L1 (2004).

[100] D. Huterer and M. S. Turner, Phys. Rev. D **60**, 081301 (1999); D. Huterer and M. S. Turner, Phys. Rev. D **64**, 123527 (2001).

[101] J. Weller and A. Albrecht, Phys. Rev. Lett. **86**, 1939 (2001).

[102] M. Chevallier and D. Polarski, Int. J. Mod. Phys. D **10**, 213 (2001).

[103] E. V. Linder, Phys. Rev. Lett. **90**, 091301 (2003); Phys. Rev. D **70**, 023511 (2004).

[104] B. A. Bassett, M. Kunz, J. Silk and C. Ungarelli, Mon. Not. Roy. Astron. Soc. **336**, 1217 (2002).

[105] P. S. Corasaniti and E. J. Copeland, Phys. Rev. D **67**, 063521 (2003).

[106] D. Huterer and G. Starkman, Phys. Rev. Lett. **90**, 031301 (2003).

[107] R. G. Crittenden, L. Pogosian and G. Zhao, JCAP **12**, 025 (2009) [arXiv:astro-ph/0510293]

[108] D. Huterer and A. Cooray, Phys. Rev. D **71**, 023506 (2005) [arXiv:astro-ph/0404062].

[109] G. -B. Zhao and X. -m. Zhang, Phys. Rev. D **81**, 043518 (2010) [arXiv:0908.1568 [astro-ph.CO]].

[110] R. G. Crittenden, G. -B. Zhao, L. Pogosian, L. Samushia and X. Zhang, JCAP **1202**, 048 (2012) [arXiv:1112.1693 [astro-ph.CO]].

[111] T. D. Saini, S. Raychaudhury, V. Sahni and A. A. Starobinsky, Phys. Rev. Lett. **85**, 1162 (2000) [arXiv:astro-ph/9910231].

[112] Akaike, Hirotugu (1974). "A new look at the statistical model identification". IEEE Transactions on Automatic Control 19 (6): 716723.

[113] Schwarz G., 1978, Ann. Statist., **5**, 461

[114] A. R. Liddle, Mon. Not. Roy. Astron. Soc. **351**, L49 (2004).

[115] A. Hojjati, L. Pogosian and G. -B. Zhao, JCAP **1004**, 007 (2010) [arXiv:0912.4843 [astro-ph.CO]].

[116] S. M. Carroll, M. Hoffman and M. Trodden, Phys. Rev. D **68**, 023509 (2003) [arXiv:astro-ph/0301273].

[117] P. Mukherjee and Y. Wang, Astrophys. J. **598**, 779 (2003) [arXiv:astro-ph/0301562].

[118] A. Shafieloo, T. Souradeep, P. Manimaran, P. K. Panigrahi and R. Rangarajan, Phys. Rev. D **75**, 123502 (2007) [arXiv:astro-ph/0611352].

[119] M. Hobson, A. Jones and A. Lasenby, arXiv:astro-ph/9810200; P. Mukherjee, M. P. Hobson and A. N. Lasenby, Mon. Not. Roy. Astron. Soc. **318**, 1157 (2000) [arXiv:astro-ph/0001385]; P. Mukherjee and Y. Wang, Astrophys. J. **613**, 51 (2004) [arXiv:astro-ph/0402602]; J. D. McEwen, M. P. Hobson, A. N. Lasenby and D. J. Mortlock, Mon. Not. Roy. Astron. Soc. Lett. **371**, L50 (2006) [arXiv:astro-ph/0604305]; A. Curto, E. Martinez-Gonzalez, P. Mukherjee, R. B. Barreiro, F. K. Hansen, M. Liguori and S. Matarrese, arXiv:0807.0231 [astro-ph]; P. Cabella *et al.*, arXiv:0910.4362 [astro-ph.CO].

[120] P. Cabella, P. Natoli and J. Silk, Phys. Rev. D **76**, 123014 (2007) [arXiv:0705.0810 [astro-ph]].

[121] Daubechies, I. 1988, Communications on Pure and Applied Mathematics, vol. 41, pp. 909996

[122] Numerical Recipes 3rd Edition: The Art of Scientific Computing by William H. Press, Saul A. Teukolsky, William T. Vetterling, and Brian P. Flannery

[123] A. G. Kim, E. V. Linder, R. Miquel and N. Mostek, Mon. Not. Roy. Astron. Soc. **347**, 909 (2004) [arXiv:astro-ph/0304509].

[124] G. Aldering *et al*, Proc. SPIE, 4836, 61 (2002).

[125] E. Komatsu *et al.* [WMAP Collaboration], Astrophys. J. Suppl. **180**, 330 (2009) [arXiv:0803.0547 [astro-ph]].

[126] Y. Wang and P. Mukherjee, Phys. Rev. D **76**, 103533 (2007) [arXiv:astro-ph/0703780].

[127] O. Elgaroy and T. Multamaki, arXiv:astro-ph/0702343.

[128] H. Li, J. Q. Xia, G. B. Zhao, Z. H. Fan and X. Zhang, Astrophys. J. **683**, L1 (2008) [arXiv:0805.1118 [astro-ph]].

[129] P. Mukherjee, M. Kunz, D. Parkinson and Y. Wang, Phys. Rev. D **78**, 083529 (2008) [arXiv:0803.1616 [astro-ph]].

[130] W. J. Percival, S. Cole, D. J. Eisenstein, R. C. Nichol, J. A. Peacock, A. C. Pope and A. S. Szalay, Mon. Not. Roy. Astron. Soc. **381**, 1053 (2007) [arXiv:0705.3323 [astro-ph]].

[131] Pearson, K. (1901). "On Lines and Planes of Closest Fit to Systems of Points in Space" (PDF). Philosophical Magazine 2 (6): 559572.

[132] J. Q. Xia, G. B. Zhao, H. Li, B. Feng and X. Zhang, Phys. Rev. D **74**, 083521 (2006).

[133] M. Chevallier and D. Polarski, Int. J. Mod. Phys. D **10**, 213 (2001).

[134] E. V. Linder, Phys. Rev. Lett. **90**, 091301 (2003).

[135] G. B. Zhao and X. Zhang, arXiv:0908.1568 [astro-ph.CO].

[136] M. Hicken *et al.*, Astrophys. J. **700**, 1097 (2009) [arXiv:0901.4804 [astro-ph.CO]].

[137] C. M. Will, *Cambridge, UK: Univ. Pr. (1993) 380 p.*

[138] S. M. Carroll, *San Francisco, USA: Addison-Wesley (2004) 513 p*

[139] T. Damour and K. Nordtvedt, Phys. Rev. D **48**, 3436 (1993).

[140] C. Brans and R. H. Dicke, Phys. Rev. 124, 925 (1961)

[141] B. Bertotti, L. Iess and P. Tortora, Nature **425**, 374 (2003).

[142] S. Capozziello, S. Carloni and A. Troisi, Recent Res. Dev. Astron. Astrophys. **1**, 625 (2003) [arXiv:astro-ph/0303041].

[143] S. M. Carroll, V. Duvvuri, M. Trodden and M. S. Turner, Phys. Rev. D **70**, 043528 (2004) [arXiv:astro-ph/0306438].

[144] A. D. Dolgov and M. Kawasaki, Phys. Lett. B **573**, 1 (2003) [arXiv:astro-ph/0307285].

[145] T. Chiba, Phys. Lett. B **575**, 1 (2003) [arXiv:astro-ph/0307338].

[146] A. L. Erickcek, T. L. Smith and M. Kamionkowski, Phys. Rev. D **74**, 121501 (2006) [arXiv:astro-ph/0610483].

[147] I. Sawicki and W. Hu, Phys. Rev. **D75**, p. 127502 (2007).

[148] L. Amendola, Phys. Rev. **D62**, p. 043511 (2000).

[149] R. Bean and J. Magueijo, Phys. Lett. **B517**, 177 (2001).

[150] A. Coc, K. A. Olive, J. -P. Uzan and E. Vangioni, Phys. Rev. D **73**, 083525 (2006) [astro-ph/0601299].

[151] C. Schimd, J. -P. Uzan and A. Riazuelo, Phys. Rev. D **71**, 083512 (2005) [astro-ph/0412120].

[152] R. Catena, M. Pietroni and L. Scarabello, Phys. Rev. D **76** (2007) 084039 [astro-ph/0604492].

[153] G. R. Dvali, G. Gabadadze and M. Porrati, Phys. Lett. **B485**, 208 (2000).

[154] A. Lue, Phys. Rept. **423**, 1 (2006).

[155] S. Rydbeck, M. Fairbairn and A. Goobar, JCAP **0705**, p. 003 (2007).

[156] W. Fang et al., Phys. Rev. **D78**, p. 103509 (2008).

[157] N. Arkani-Hamed, S. Dimopoulos, G. Dvali and G. Gabadadze, arXiv:hep-th/0209227.

[158] G. Dvali, S. Hofmann and J. Khoury, Phys. Rev. D **76**, 084006 (2007) [arXiv:hep-th/0703027].

[159] D. N. Vollick, Phys. Rev. D **68**, 063510 (2003) [arXiv:astro-ph/0306630].

[160] G. J. Olmo, Phys. Rev. D **72**, 083505 (2005).

[161] V. Sahni and Y. Shtanov, JCAP **0311**, 014 (2003) [arXiv:astro-ph/0202346].

[162] K. Freese and M. Lewis, Phys. Lett. B **540**, 1 (2002) [arXiv:astro-ph/0201229].

[163] S. Rasanen, JCAP **0402**, 003 (2004).

[164] E. Barausse, S. Matarrese and A. Riotto, Phys. Rev. D **71** 063537 (2005).

[165] E. W. Kolb, S. Matarrese, A. Notari and A. Riotto, arXiv:hep-th/0503117.

[166] E. W. Kolb, S. Matarrese and A. Riotto, arXiv:astro-ph/0506534; arXiv:astro-ph/0511073; arXiv:astro-ph/0511124.

[167] T. Buchert, Gen. Rel. Grav. **32**, 105 (2000).

[168] T. Buchert, Gen. Rel. Grav. **33**, 1381 (2001).

[169] N. C. Tsamis and R. P. Woodard, Phys. Lett. B **301**, 351 (1993).

[170] N. C. Tsamis and R. P. Woodard, Annals Phys. **253**, 1 (1997).

[171] N. C. Tsamis and R. P. Woodard, Nucl. Phys. B **474**, 235 (1996).

[172] N. C. Tsamis and R. P. Woodard, Annals Phys. **267**, 145 (1998).

[173] E. E. Flanagan, Phys. Rev. D **71**, 103521 (2005); G. Geshnizjani, D. J. H. Chung and N. Afshordi, Phys. Rev. D **72**, 023517 (2005); C. M. Hirata and U. Seljak, Phys. Rev. D **72**, 083501 (2005); E. R. Siegel and J. N. Fry, Astrophys. J. **628**, L1 (2005).

[174] A. Ishibashi and R. M. Wald, Class. Quant. Grav. **23**, 235-250 (2006).

[175] T. Buchert, J. Larena and J. M. Alimi, arXiv:gr-qc/0606020.

[176] K. S. Thorne and C. M. Will. ApJ, 163:595, Feb. 1971.

[177] L. Pogosian, A. Silvestri, K. Koyama and G. -B. Zhao, Phys. Rev. D **81**, 104023 (2010) [arXiv:1002.2382 [astro-ph.CO]].

[178] L. M. Wang and P. J. Steinhardt, Astrophys. J. **508**, 483 (1998) [arXiv:astro-ph/9804015].

[179] E. V. Linder and R. N. Cahn, Astropart. Phys. **28**, 481 (2007) [arXiv:astro-ph/0701317].

[180] T. Clifton, P. G. Ferreira, A. Padilla and C. Skordis, Phys. Rept. **513**, 1 (2012) [arXiv:1106.2476 [astro-ph.CO]].

[181] V. Acquaviva, A. Hajian, D. N. Spergel and S. Das, Phys. Rev. D **78**, 043514 (2008) [arXiv:0803.2236 [astro-ph]].

[182] W. Hu and I. Sawicki, Phys. Rev. D **76**, 104043 (2007) [arXiv:0708.1190 [astro-ph]].

[183] P. Zhang, Phys. Rev. D **73**, 123504 (2006) [arXiv:astro-ph/0511218].

[184] P. Brax, C. van de Bruck, A. C. Davis and A. M. Green, Phys. Lett. B **633**, 441 (2006) [arXiv:astro-ph/0509878].

[185] Y. S. Song, W. Hu and I. Sawicki, Phys. Rev. D **75**, 044004 (2007) [arXiv:astro-ph/0610532].

[186] R. Bean, D. Bernat, L. Pogosian, A. Silvestri and M. Trodden, Phys. Rev. D **75**, 064020 (2007) [arXiv:astro-ph/0611321].

[187] L. Pogosian and A. Silvestri, Phys. Rev. D **77**, 023503 (2008) [arXiv:0709.0296 [astro-ph]].

[188] S. Tsujikawa, Phys. Rev. D **77**, 023507 (2008) [arXiv:0709.1391 [astro-ph]].

[189] K. Koyama and R. Maartens, JCAP **0601**, 016 (2006) [arXiv:astro-ph/0511634].

[190] Y. S. Song, I. Sawicki and W. Hu, Phys. Rev. D **75**, 064003 (2007) [arXiv:astro-ph/0606286].

[191] Y. S. Song, arXiv:0711.2513 [astro-ph].

[192] A. Cardoso, K. Koyama, S. S. Seahra and F. P. Silva, Phys. Rev. D **77**, 083512 (2008)

[193] N. Afshordi, G. Geshnizjani and J. Khoury, JCAP **0908**, 030 (2009).

[194] J. M. Bardeen, Phys. Rev. D **22**, 1882 (1980).

[195] V. F. Mukhanov, H. A. Feldman and R. H. Brandenberger, Phys. Rept. **215**, 203 (1992).

[196] R. Caldwell, A. Cooray, and A. Melchiorri, Phys. Rev. D, 76(2):023507 (2007).

[197] M. A. Amin, R. V. Wagoner, and R. D. Blandford, MNRAS, 390:131 (2008).

[198] S. AAppleby and J. Weller, JCAP **1012**, 006 (2010) [arXiv:1008.2693 [astro-ph.CO]].

[199] P. G. Ferreira and C. Skordis, Phys.Rev. (2010).

[200] `Http://www.sfu.ca/~aha25/MGCAMB.html`

[201] `http://camb.info/`

[202] A. Lewis, A. Challinor and A. Lasenby, Astrophys. J. **538**, 473 (2000) [arXiv:astro-ph/9911177].

[203] `http://cosmologist.info/cosmomc/`

[204] M. Zaldarriaga and U. Seljak, Phys. Rev. D **55**, 1830 (1997) [arXiv:astro-ph/9609170].

[205] W. Hu and M. J. White, Phys. Rev. D **56**, 596 (1997) [arXiv:astro-ph/9702170].

[206] S. Ho, C. Hirata, N. Padmanabhan, U. Seljak and N. Bahcall, Phys. Rev. D **78**, 043519 (2008) [arXiv:0801.0642 [astro-ph]].

[207] W. Hu and I. Sawicki, Phys. Rev. D **76**, 064004 (2007) [arXiv:0705.1158 [astro-ph]].

[208] T. Giannantonio, M. Martinelli, A. Silvestri and A. Melchiorri, JCAP **1004**, 030 (2010) [arXiv:0909.2045 [astro-ph.CO]].

[209] S. A. Thomas, S. A. Appleby and J. Weller, JCAP **1103**, 036 (2011) [arXiv:1101.0295 [astro-ph.CO]].

[210] Y. S. Song, G. B. Zhao, D. Bacon, K. Koyama, R. C. Nichol and L. Pogosian, arXiv:1011.2106 [astro-ph.CO].

[211] Y. S. Song, L. Hollenstein, G. Caldera-Cabral and K. Koyama, arXiv:1001.0969 [astro-ph.CO].

[212] R. Bean and M. Tangmatitham, Phys. Rev. D **81**, 083534 (2010) [arXiv:1002.4197 [astro-ph.CO]].

[213] Y. S. Song, H. Peiris and W. Hu, Phys. Rev. D **76**, 063517 (2007) [arXiv:0706.2399 [astro-ph]].

[214] E. Komatsu *et al.* [WMAP Collaboration], Astrophys. J. Suppl. **192**, 18 (2011) [arXiv:1001.4538 [astro-ph.CO]].

[215] R. Kessler *et al.*, Astrophys. J. Suppl. **185**, 32 (2009) [arXiv:0908.4274 [astro-ph.CO]].

[216] A. G. Riess *et al.*, Astrophys. J. **699**, 539 (2009) [arXiv:0905.0695 [astro-ph.CO]].

[217] L. Lombriser, A. Slosar, U. Seljak and W. Hu, arXiv:1003.3009 [astro-ph.CO].

[218] T. Giannantonio *et al.*, Phys. Rev. D **74** (2006) 063520 [arXiv:astro-ph/0607572].

[219] W. Hu, Phys. Rev. D **77**, 103524 (2008) [arXiv:0801.2433 [astro-ph]].

[220] G. B. Zhao, L. Pogosian, A. Silvestri and J. Zylberberg, Phys. Rev. Lett. **103**, 241301 (2009) [arXiv:0905.1326 [astro-ph.CO]].

[221] http://pan-starrs.ifa.hawaii.edu

[222] E. Beynon, D. J. Bacon, K. Koyama, Mon. Not. Roy. Astron. Soc. **403**, 353-362 (2010). [arXiv:0910.1480 [astro-ph.CO]].

[223] P. Astier, J. Guy, R. Pain and C. Balland, arXiv:1010.0509 [astro-ph.CO].

[224] W. Hu and B. Jain, Phys. Rev. D **70**, 043009 (2004) [arXiv:astro-ph/0312395].

[225] http://snfactory.lbl.gov/

[226] http://sci.esa.int/planck

[227] Z. Ivezic, J. A. Tyson, et al for the LSST Collaboration, arXiv:0805.2366 [astro-ph].

[228] J. F. Kenney and E. S. Keeping, *Mathematics of Statistics, Part II*, 2nd ed. (Van Nostrand, New York) (1951).

[229] M. G. Kendall, A. Stuart, *The Advanced Theory of Statistics, Volume II*, Griffin, London (1969).

[230] M. Tegmark, A. Taylor and A. Heavens, Astrophys. J. **480**, 22 (1997) [arXiv:astro-ph/9603021].

[231] H. Zhan, L. Knox and J. A. Tyson, Astrophys. J. **690**, 923 (2009) [arXiv:0806.0937 [astro-ph]].

[232] G. Bernstein and D. Huterer, arXiv:0902.2782 [astro-ph.CO].

[233] G. -B. Zhao, T. Giannantonio, L. Pogosian, A. Silvestri, D. J. Bacon, K. Koyama, R. C. Nichol, Y. -S. Song, Phys. Rev. **D81**, 103510 (2010). [arXiv:1003.0001 [astro-ph.CO]].

[234] F. Schmidt, A. Vikhlinin and W. Hu, Phys. Rev. D **80**, 083505 (2009) [arXiv:0908.2457 [astro-ph.CO]].

[235] A. J. S. Hamilton, astro-ph/9708102.

[236] L. Hui and K. P. Parfrey, Phys. Rev. D **77**, 043527 (2008) [arXiv:0712.1162 [astro-ph]].

[237] R. G. Crittenden, L. Pogosian and G. B. Zhao, JCAP **0912**, 025 (2009) [arXiv:astro-ph/0510293].

[238] G. -B. Zhao, H. Li, E. V. Linder, K. Koyama, D. J. Bacon and X. Zhang, arXiv:1109.1846 [astro-ph.CO].